DIELECTRIC PROPERTIES OF CRYOGENIC GASES

A Dissertation
Presented to
The Academic Faculty

by

Chanyeop Park

In Partial Fulfillment
of the Requirements for the Degree
Doctor of Philosophy in the
School of Electrical and Computer Engineering

Georgia Institute of Technology
May 2018

DIELECTRIC PROPERTIES OF CRYOGENIC GASES

Approved by:

Professor Lukas Graber, Advisor
School of Electrical and Computer Engineering
Georgia Institute of Technology

Professor Santiago Grijalva
School of Electrical and Computer Engineering
Georgia Institute of Technology

Professor Sastry Pamidi, Co-advisor
Department of Electrical and Computer Engineering, FAMU-FSU College of Engineering
Florida State University

Professor Thomas Habetler
School of Electrical and Computer Engineering
Georgia Institute of Technology

Professor Maryam Saeedifard
School of Electrical and Computer Engineering
Georgia Institute of Technology

Professor Mitchell Walker
School of Aerospace Engineering
Georgia Institute of Technology

Date Approved: January 22, 2018

To my dear wife

Yeseul Lee

and respected parents

for their unlimited trust and support.

ACKNOWLEDGEMENTS

No words could express my utter gratitude and respect for my advisor Professor Lukas Graber, whom I think is not only one of the nicest professors, but also the kindest individuals I met in my life. I still remember how glad I felt when he welcomed me the very first day I stepped into his office. Meeting with him since then has always been pleasant and inspiring. Discussing research ideas with Lukas has been extremely creative and open-ended. He gave me the freedom to explore further and to decide what the next steps should be, but guided me with his expert knowledge when I was overlooking something. There is no doubt that the balance between the freedom and inspiration Lukas provided me with was the key for my accomplishments.

My sincere gratitude also goes to my co-advisor Professor Sastry Pamidi. Without Sastry's positive spirit and encouragement, my research would not have developed into what it is now. Sastry has been one of the greatest champions of my research, who always encouraged my ideas. The positive energy projecting out from Sastry's mind, at times, made me believe that I had already solved a problem, which gave me great confidence, even before I began working on it. Also, my research, which has been mainly supported by the Office of Naval Research (ONR) through the grants N00014-14-1-0346 and N00014-16-1-2282, would not have been possible without Sastry's support.

I must admit that I was extremely lucky throughout my doctoral program to have many scientists and engineers from all around the world including Switzerland, France, China, and South Korea, who kindly shared their knowledge with me even though they never knew me personally. Among them, I would like to offer my special thanks to June Young Kim. Discussing with June Young from the early days of my

doctoral program enabled me to quickly understand the basics of plasma physics, which has been fruitful to the heart of my research.

Professor Ju Lee, who was my undergraduate and master's thesis advisor, has always been the inspiration in the background of my academic life. After graduating from my undergraduate program, he gave me the honor of being a part of his lab as a master's student and provided me with overwhelming support and guidance ever since. My sincere recognition goes to Professor Ju Lee and his family.

Back in Fall 2013, I would not have been able to come to the U.S. for my Ph.D. program without the tremendous support that I received from the Kwanjeong Educational Foundation. The commitment and responsibility that I had as a recipient of the Kwanjeong scholarship, which is the most prestigious scholarship in South Korea only paralleled by the Samsung scholarship, have been one of the greatest motivations to push my work forward. I deeply acknowledge the invaluable support provided by the members of the Kwanjeong Educational Foundation.

Most importantly, I sincerely thank my family for being extraordinarily forgiving and supportive over the last several years of my doctoral program. I must express my gratitude to my parents-in-law Minho Lee and Keumsook Choi for their unfailing support. It is unquestionable that I have always deeply thanked and loved my parents, Changseo Park and Junghee Cho for their unconditional trust, encouragement, and unending patience. It is their love and sacrifice that raised me to become who I am today. I would like to also acknowledge my only brother Chanyong, a true pursuer of his dream and passion, for being a true inspiration for me whenever I felt weakened.

Finally, my ultimate appreciation and gratitude goes to my beloved wife Yeseul. I am undoubtedly the luckiest man to marry Yeseul, who is the most proactive, positive, brightest, and loveliest person I have ever met. Since long before our marriage, Yeseul has been my hope and guardian: she loved, trusted, supported, and encouraged me to get through the most uncertain period my life in the most hopeful way.

TABLE OF CONTENTS

LIST OF TABLES

LIST OF FIGURES

SUMMARY

With the goal of improving the dielectric strength of gaseous cryogens, this dissertation discusses the dielectric properties of cryogenic gas mixtures based on electron kinetics, dielectric modeling, and plasma diagnostics. The electron kinetics work involves the numerical analysis of electron ensembles in cryogenic gas mixtures. The results of the analysis qualitatively predict the varying dielectric strength of the cryogenic gas mixtures. The dielectric modeling work provides the quantitative predictions of gas dielectric strength in terms of breakdown voltages. Specifically, the work develops a new dielectric strength model that can accurately estimate the dielectric strength variations caused by the variation of cryogenic gas mixture composition. The plasma diagnostics work involves the design and development of a plasma experiment, which is used for measuring DC plasmas generated from potential cryogenic gas mixtures. By analyzing the measured results, the electron energy distribution function of each gas mixture is derived, which is subsequently used for calculating plasma parameters including plasma density and plasma temperature. Research tasks discussed in this dissertation are dedicated for the dielectric enhancement of gaseous cryogens, which is pivotal for the development of medium- and high-voltage superconducting power applications.

CHAPTER I

PROBLEM STATEMENT

Traditionally, liquid nitrogen has been the standard cooling medium (cryogen) for operating superconducting power applications. However, gaseous cryogens, which have several benefits over liquid cryogens, are recognized as promising cooling media for future superconducting power systems. The main benefits of gaseous cryogens are lower asphyxiation hazard, wider operating temperature range, which enables superconductors to be operated with higher current density, and lower pumping effort, which allows the use of longer superconducting cables and the integration of multiple superconducting devices with a single refrigeration system.

Although many advantages are gained by using gaseous cryogens, the major challenges for the widespread use of gas-cooled superconducting power applications are lower heat capacity and lower dielectric strength. Studies addressing means for compensating the low heat capacity issue have been reported in the literature. However, no study has thus far reported any feasible solutions for the low dielectric strength challenge associated with using gaseous cryogens. This dissertation focuses on developing tools to study and discovering methods to improve the dielectric strength of gaseous cryogens for medium- and high-voltage superconducting power applications.

CHAPTER II

STATE OF THE ART

2.1 Superconductors for Power Applications

Electric power demand is escalading worldwide and the growing use of electric vehicles in urban districts is expected to boost the demand even further. Environmental issues call for improved energy efficiency and lower carbon emissions. The expanding urban power grid and the increased reliance on distributed renewable energy sources pose the threat of more frequent faults and larger fault currents. There is an urgent need for power system technologies that offer enhanced resilience, reliability, and power quality. Several new technologies are being explored to address the challenges. Superconducting electrical power system technology is one of the feasible solutions for many of the challenges.

Superconductors are materials that show zero electrical resistance below their critical temperatures. The superconductivity was first discovered in 1911 by Kamerlingh Onnes, who also discovered a method to liquify helium, when he observed a sudden drop in resistance of mercury at 4 K while measuring the resistance of pure metals in liquid helium [63]. Superconductors can be broadly classified into two groups based on their critical temperatures. Superconductors with critical temperatures below 30 K are classified as low temperature superconductors (LTS) and those with critical temperatures above 30 K are classified as high temperature superconductors (HTS). High temperature superconductivity in $LaBaCuO_x$ with a critical temperature at 35 K was first discovered in 1986 [11]. A year later, in 1987, superconductivity in $YBa_2Cu_3O_7$ (YBCO) with the critical temperature of 93 K was discovered. The YBCO structure allowed the substitution of Yttrium by several rare-earth elements and since then

Superconductor	Transition temperature (K)
Nb	9.5
NbTi	9.5
Nb_3Sn	18.3
Nb_3Al	18.8
MgB_2	39
$REBa_2Cu_3O_7$	93
$Bi_2Sr_2Ca_1Cu_2O_8$	85
$Bi_2Sr_2Ca_2Cu_3O_{10}$	108−110

Figure 1: A list of practical superconductors [79].

these materials have been called REBCO superconductors. In fact, REBCO became the first material that showed superconductivity above the boiling point of liquid nitrogen (*i.e.*, 77 K) and has continued to be used as one of the materials for HTS power applications [79].

Although hundreds of superconducting materials have been discovered since the first discovery in 1911, fewer than ten of them have practical use for power applications as listed in Figure 1 [79]. The reasons behind such few practical superconducting materials are the following. First of all, superconductors should be operated within the superconducting region shown in Figure 2. The figure presents a superconducting region in 3-D surface bounded by critical temperature (T_c), critical magnetic field (B_c), and current density (J_c). All three conditions should be satisfied for a superconductor to be superconducting. Within the superconducting region, practical superconductors are operated in the temperature range typically provided by cryogens (*i.e.*, cooling media). Most superconducting applications are cooled with liquid nitrogen (65–77 K) or liquid helium (1.2–4.2 K). Hence, the critical temperature of the superconductors should be higher than the boiling point of nitrogen or helium such that it could maintain its superconducting property under potential temperature excursions. Another factor that must be satisfied to become a practical

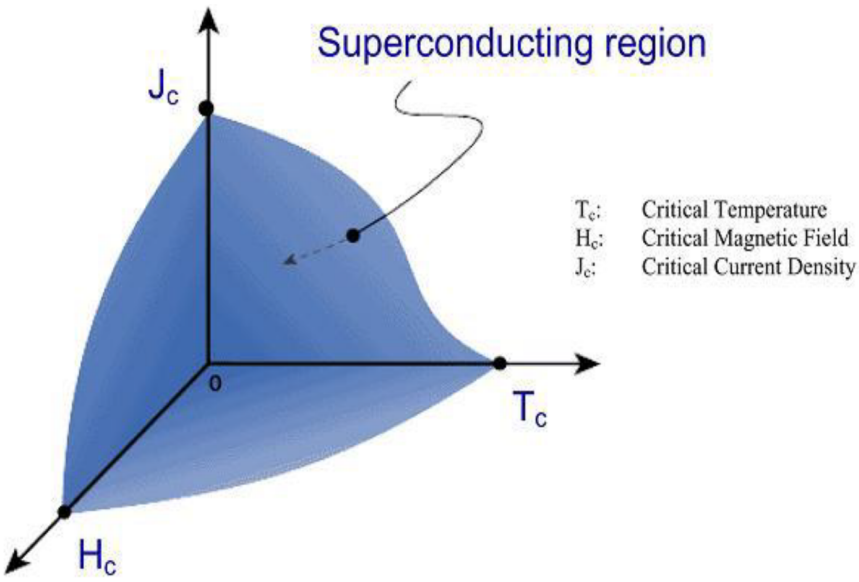

Figure 2: Superconducting region defined by critical temperature (T_c), critical magnetic field (B_c), and current density (J_c) [66].

superconductor is sufficient current density at the operating temperature and background magnetic field. As shown in Figure 2, superconductors, in general, cannot conduct large electrical current when the background magnetic field is high. Hence, for instance, superconductors for rotating machines should show exceptionally good performance even under high magnetic fields, which drastically reduces the options of practical superconductors. These requirements indicate that the power density per volume or weight of practical superconductors should be significantly higher than that of conventional conductors (copper or aluminum). Furthermore, the practical superconductors should be amenable to being manufactured into the form of flexible wire or tape with sufficient mechanical strength and robustness required for the fabrication and operation of electrical power devices. Since all of these requirements must be satisfied simultaneously, the number of superconducting materials that are suitable for electric power application is limited.

The need for superconducting technology arises when high energy efficiency and high power density become crucial design factors. The increasing demand for electric power is one of the challenges power utilities are faced with. According to the "Annual

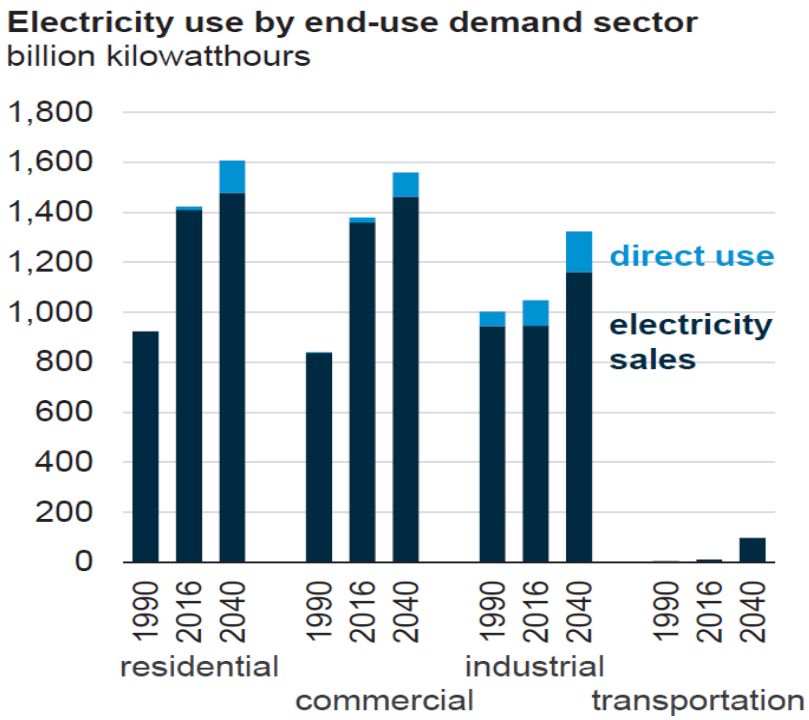

Figure 3: Electricity Consumption Continues to Increase [7]. *Growth in direct use generation above growth in sales is primarily the result of the adoption of rooftop photovoltaic (PV) and natural gas-fired combined heat and power (CHP).

Energy Outlook 2017" reported by the U.S. Energy Information Administration (Figure 3), the demand for electric power has been steadily increasing and is projected to further increase in the coming decades in all sectors including transportation mainly caused by the expected massive electrification of automobiles, ships, and aircrafts [7]. The major issue is that much of the increase of power demand is expected to occur in the concentrated urban areas. The growing urban power demand is becoming a severe challenge for conventional copper and aluminum cable technology that transmit electricity to the cities, which is also known as the urban power bottleneck", but superconducting technology can provide high efficiency, high power density, and high reliability under potential contingencies. To list some of the superconducting technologies, superconducting cables have major advantages of carrying much larger currents, typically 2–4 kA for the same cross section as conventional copper cables carrying 1 kA. The current carrying capability of such cables can effectively fulfill

the increasing energy demand. Superconducting fault current limiters enhance the reliability of power grids. These devices exploit the nonlinearly increasing resistance of superconductors, also known as superconductor-to-resistive transition, that occurs when current higher than its critical current flows. This transition has the advantage of being self-triggered and reacting almost instantaneously without any external activation sequences. Furthermore, superconducting synchronous rotating machines, which are installed with rotors made of superconducting coils and stators with copper coils, have several advantages over conventional electric machines [83]. Superconducting machines provide higher efficiency and reduced size and weight: a 36.5 MW ship propulsion motor was demonstrated for the U.S. Navy and weighed one-fourth of a conventional machine with the same power rating including all supporting components [27].

HTS technologies not only provide feasible solutions for the power utilities, but also enables technological advancements for aerospace and naval applications. Future naval ships will have electromagnetic rail guns, electromagnetic aircraft launch systems (EMALS), high power lasers, high power radars, and directed energy weapons, which all require more efficient power management. Also, power apparatuses with high power density are required in future ships since the size of the ships will be kept relatively small. Increased power demand and restricted size of future naval ships require the use of integrated HTS power systems [59]. Using conventional copper cables to satisfy the increased power ratings instead of using HTS cables will cause significant size and weight increase. The difference in power density is obvious when material properties are compared: copper can conduct 350 A/cm^2 while HTS materials can conduct 30,000 A/cm^2 [59]. As shown in Figure 4, 12 copper cables with 2.2 in (55.9 mm) outer diameter (OD) is equivalent to 1 HTS cable with 2.75 in (69.8 mm) OD. Hence, a successful implementation of an HTS power system could reduce the weight and volume by 75% and 80%, respectively. Due to these benefits, one of the

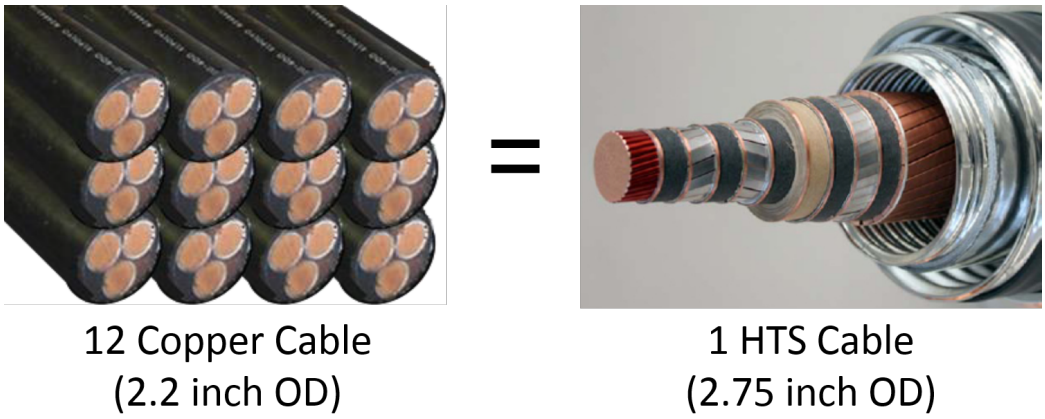

Figure 4: Comparing the dimensions of conventional copper cables to HTS cables.

options of future electric ship and aircraft power systems is operating them at cryogenic temperatures to utilize the high power density and high efficiency provided by HTS motors, generators, and cables [12, 59].

A typical cryogenic power system is shown in Figure 5. The term "cryogenic" is used instead of "HTS" or "superconducting" since the power electronic converters are not superconducting, but still operating at a cryogenic temperature. For such power systems a cryogenic cooling loop with a central cryo-refrigeration plant would be the most versatile and efficient way to integrate multiple devices with a wide range of cryogenic operating temperature between 10–100 K. HTS motors and generators, which are exposed to high background magnetic fields, are devices that require comparatively lower temperature operation (20–40 K). HTS cables, which are not exposed to significant magnetic field, can achieve substantial power densities even at temperatures around 70 K. Depending on the application and system design, HTS cables can be operated at temperatures within 50–80 K to exploit the benefits of high power density and minimum cooling cost. In fact, the coefficient of performance (COP) for cooling is given by

$$COP_{cooling} = \frac{Q_c}{W_{in}} = \frac{T_c}{T_h - T_c}, \tag{1}$$

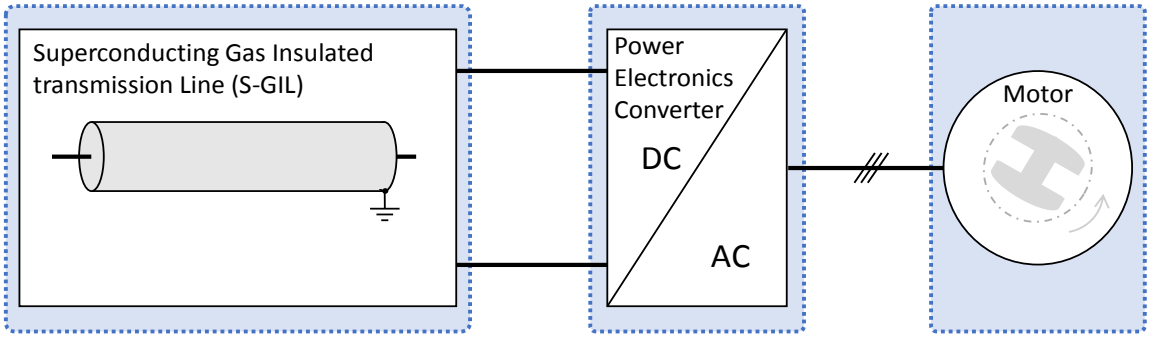

Figure 5: Components of a Cryogenic Power System

where Q_c is the energy of heat removed from the cold temperature T_c and W_{in} is the consumed energy of a refrigeration system, which exhausts heat at the ambient temperature of T_h. The equation indicates that cooling superconductors at 4.2 K with an ambient temperature of 300 K results in 1.4% cooling efficiency while cooling superconductors at 77 K with the same ambient temperature results in 34.5% cooling efficiency. Note that these values are the theoretical maximums and in practice 10–33% of these values can be achieved [79]. The main purpose of operating power electronics devices at cryogenic temperatures is to maximize overall system efficiency. A large temperature gradient exists between the HTS cable and copper conductors if conventional power electronic converters are used. The temperature gradient from ambient to the cryogenic system causes substantial heat leak, which reduces the overall efficiency of power systems and requires larger cryogenic cooling systems. Hence, the capital and operating costs of cryogenic systems are expected to be significantly reduced when the power electronic converters are operated under cryogenic conditions. Accounting for potential miss-match in the coefficients of thermal expansion (CTE), the cryogenic power converters would most likely operate at the warmest range of cryogenic operating temperatures (80–100 K). Since no liquid cryogen can be used in such a system that requires a potential operating temperature range of 10–100 K, the cooling system would have to be operated based on gaseous cryogens

such as He, H_2, N_2, F_2, and O_2 or mixtures of them.

2.2 Challenges of Using Gaseous Cryogens in Power Devices

High temperature superconducting (HTS) technology is a promising solution for future power grid, aerospace, and naval power applications, where high efficiency and high power density is crucial. Liquid nitrogen (N_2) has been the standard cryogenic cooling medium for high-temperature superconducting (HTS) power applications owing to its effective cooling capability and high dielectric strength [42]. Nevertheless, gaseous helium (He)-cooled HTS applications are being developed for aerospace and naval applications to take advantage of the wider operating temperature range offered by gaseous He. HTS devices become smaller and lighter by using He since lower operating temperatures enable superconductors carry higher current densities. The temperature dependent current density in HTS materials combined with the wider range of operating temperature allowed by gaseous He enable the tuning of the operating power rating of an HTS device, which provides an effective and inexpensive means of meeting the required higher-than-typical power demands in certain operational scenarios. Gaseous cryogens also enable easier integration of cryogenic systems of multiple devices into a single cryogenic cooling loop that is served by a centralized cryogenic plant. In fact, integrating multiple devices with a single larger cryogenic system, which is relatively difficult to realize with the use of liquid N_2 because of its narrower liquid temperature range [71, 72], is more efficient than doing so with several smaller distributed cryogenic systems [65]. Moreover, gaseous He reduces the risk of asphyxiation hazards posed by liquid N_2 in closed-space applications such as on-board ships or aircrafts [65]. Furthermore, gaseous cryogens require lower pumping effort than liquids, which enables the use of superconducting cables over longer distances and between different elevations. Due to these benefits, cryogenic gaseous He is preferred in aerospace and naval superconducting power applications [26, 47]. The

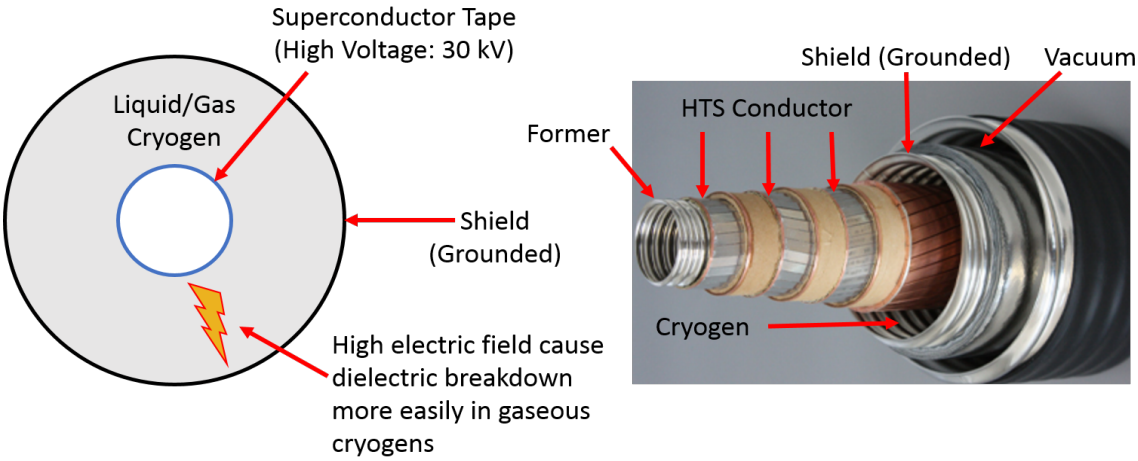

Figure 6: High-Temperature Superconducting Cable.

U.S. Navy has demonstrated HTS degaussing systems, which are used for reducing the magnetic signatures of naval ships, with gaseous helium-cooled HTS cables as a replacement for copper-based degaussing systems [47]. Also, megawatt-scale helium-cooled HTS ship propulsion motors have been successfully demonstrated by the U.S. Navy [25, 27].

Despite all of the benefits of using gaseous He as a cryogen, the naval HTS power applications, currently running at low voltages, are expected to face issues when the operation is extended to medium and high voltages. The issues are mainly caused by the lower volumetric heat capacity and dielectric strength of He [80]. The heat capacity and dielectric strength of a cryogen are crucial factors in HTS power applications. This is due to the fact that a cryogen not only functions as a coolant, but also as a dielectric medium that must withstand high voltage gradients within the HTS power apparatus as shown in Figure 6. Although the figure only shows an example of an HTS cable, a similar structural simplification is possible for other HTS power devices. In any type of HTS power apparatus cavities will exist between the high voltage superconductor and the grounded shield, and cryogens will be filled in the cavities to cool superconductors and to prevent dielectric breakdown. The low heat capacity issue of gaseous He, which is important for the thermal design of HTS power

devices, have been reported. Previous studies on the cooling efficiency of gaseous He have shown that increasing the gas pressure and flow rate could partially compensate for the low cooling capability of He [67]. However, no studies have yet reported any fundamental means to improve the dielectric properties of gaseous He, which is crucial in operating HTS power devices at higher voltage levels.

2.3 Electron Kinetics

Interactions between electrons and neutral particles are largely classified into elastic and inelastic collisions. Elastic collisions occur over the entire electron energy range and become dominant at low electron energy. This type of collision results in a kinetic energy transfer with an energy transfer ratio of $2m/M$, where m is the mass of electrons and M is the mass of neutral particles. Taking into account the masses of electrons and neutral particles, $2m/M$ is on the order of 10^{-4}. For example, the $2m/M$ value of an electron-He collision is 2.7×10^{-4} and that of an electron-H_2 collision is 5.4×10^{-4}). Although kinetic energy transfer occurs between the two particles, the total kinetic energy of electrons and neutral particles is conserved in elastic collisions. On the contrary, inelastic collisions result in the dissipation of kinetic energy. As in elastic collisions, inelastic collisions involve kinetic energy transfers, but some inelastic collisions such as excitation and ionization collisions have a threshold energy that is consumed after each collision. That is, excitation collisions consume electron energies to excite neutral particles into various excited states (e.g., rotational, vibrational, and electronic excitation modes), and ionization collisions consume electron energy to ionize neutral gas particles. As a result, electrons involved in excitation and ionization collisions dissipate the amount of energy equivalent to the threshold energy of the respective inelastic collision. It should be noted that the threshold energy does not necessarily exist in electron attachment collisions, an inelastic process that removes free electrons from a gaseous medium, but lead to a total loss of electron energy.

Therefore, inelastic collisions reduce the overall energy of electrons substantially.

The collision processes between electrons and neutrals are represented by electron scattering cross sections $\sigma(\epsilon)$. Distinct sets of electron scattering cross sections exist for each gas and vary as a function of electron energy ϵ. The cross section data are essential for the calculation of the coefficients of electron kinetics including the density-reduced ionization coefficient (α/N), the density-reduced attachment coefficient (η/N), and the density-reduced effective ionization coefficient $((\alpha-\eta)/N)$. These coefficients describe variations in the number of free electrons in gases. By definition, α/N is the number of ionization collisions per unit length in the direction of the electric field normalized by particle number density N, η/N is the number of attachment collisions per unit length in the direction of the electric field normalized by N, and $(\alpha-\eta)/N$, which represents the effective number of ionization collisions per unit length in the direction of the electric field normalized by N, is simply the difference between α/N and η/N. The dielectric strength of gases can be compared by the density-reduced critical electric field $((E/N)_{cr})$: defined as the density-reduced electric field (E/N), in which the rates of ionization and attachment processes are equal, that is, E/N corresponding to $(\alpha-\eta)/N=0$.

2.4 Boltzmann Analysis

Calculating the electron kinetics coefficients of gas mixtures requires the electron energy distribution function (EEDF), which can be obtained by numerically solving the Boltzmann equation with the two-term approximation: known as the Boltzmann analysis [38, 93]. The Boltzmann equation is a kinetic equation that describes the variation of macroscopic quantities such as particle number in seven dimensions: six-spatial dimensions of position and velocity and one dimension of time.

$$\frac{\partial f}{\partial t}+\upsilon\cdot\nabla f-\frac{e}{m}E\cdot\nabla_{\mathrm{v}}f=C[f], \tag{2}$$

where v is the velocity vector, ∇ is the gradient in the position space, e is the elementary charge, m is the electron mass, E is the electric field, ∇_{v} is the gradient in the velocity space, and $C[f]$ is the collision term that determines the rate of change in f. To simplify the equation, a spatially uniform electric field and collision probability is assumed which makes the electron distribution to be symmetric in the velocity space around the electric field direction. The two-term approximation is then applied to reduce the angular dependency of the velocity with respect to the direction of the electric field [38]. It has been reported that the accuracy of the two-term approximation method is lower at high reduced electric fields (E/N), in which inelastic collisions are dominant and electron distribution is highly anisotropic [14, 38]. However, the two-term approximation can provide sufficient accuracy for the weakly ionized gases with large elastic electron scattering cross sections under low to intermediate E/N values, which apply to the conditions of the present study [77].

Boltzmann analysis was used in numerous studies searching for sulfur hexafluoride (SF_6) replacement gases and SF_6-based gas mixtures. In fact, SF_6 has been extensively used as an insulation medium and arc quenching medium for conventional high-voltage and medium-voltage power apparatuses including gas insulated switchgear (GIS) [32, 34]. However, its use led to the increased levels of SF_6 in the atmosphere, which has a global warming potential (GWP) 24,000 times greater than that of carbon dioxide (CO_2), raising concerns of global warming [31]. Hence, the primary purpose of the SF_6-related studies was, in short, finding the environmentally-friendly version of SF_6. To briefly introduce some of the related studies, Pinheiro *et al.* investigated the effective ionization coefficient $\alpha - \eta$ of SF_6 and its mixtures with He and Xe respectively [77]. Zhao *et al.* investigated the dielectric properties of the gas mixtures by taking into account the composition of dissociated species of the original gas generated during the arc quenching process, at various gas temperature and

pressure combinations [97, 98]. Wang *et al.* studied the critical breakdown electric field of SF_6-CF_4 mixtures under high gas temperature for high voltage circuit breaker application [91, 92]. Li *et al.* worked on the dielectric properties of SF_6-N_2, SF_6-CF_4 mixtures by considering the variation of the dissociated species of the original gas under various conditions of gas temperature and pressure [52, 53]. Tanaka *et al.* estimated the dielectric properties of N_2-O_2 mixtures under a wide range of gas temperature [85]. Tezcan *et al.* conducted the Boltzmann analysis on CF_4-Ar mixture by varying the mole fraction of CF_4, which is considered as a potential SF_6 replacement gas [87]. Jiang *et al.* computed the temperature and pressure distribution of a model of a circuit breaker, and used the local temperature, pressure distribution of the circuit breaker to estimate the dielectric strength of the gas at various locations of the circuit breaker [45]. Deng *et al.* conducted the Boltzmann analysis on C_3F_8-N_2 and C_3F_8-CO_2 gas mixtures [23, 24] since C_3F_8 could potentially be used as an insulating medium due to its strong electronegative property while N_2 and CO_2 were added to increase the overall vapor pressure of the mixture to prevent condensation. These studies were mainly focused on non-cryogenic temperature (*i.e.*, ambient and above-ambient temperatures) applications and used the two-term approximation method to obtain the density-reduced critical electric field ($(E/N)_{cr}$): the density-reduced electric field (E/N), at which the density-reduced ionization coefficient (α/N) and the density-reduced attachment coefficient (η/N) are in equilibrium.

Although many studies have used $(E/N)_{cr}$ as a metric to compare the dielectric strength of gas mixtures, it cannot be directly used for cryogenic gas mixtures without accounting for gas temperature, gas pressure, and gas composition that prevent gas mixtures from condensing [54, 81]. Hence, it is necessary to identify the maximum allowed mole fraction of individual gas species to investigate $(E/N)_{cr}$ and E_{cr} over the cryogenic temperature range of 10–100 K at absolute pressure levels between 1.0 and 2.0 MPa (typical pressures used in HTS applications) while assuming a constant

system volume. In this way, it is possible distinguish gas mixtures that simply show greater $(E/N)_{cr}$ from those that are feasible for practical cryogenic applications. The candidate gases for cryogenic applications are He, H_2, N_2, F_2, and O_2. Most of these gases are well investigated in their pure form, and their Paschen's curves are widely available [56, 78]. Yet, some of the fundamental dielectric properties of these gases, and especially the properties of their mixtures have not been studied in detail using the theoretical means such as Boltzmann analysis. The lack of such studies is not surprising since gases such as He and H_2 are rarely expected to perform well as dielectric media in conventional high-voltage applications. Nevertheless, their electrical insulation strength becomes significantly important, when they are used as a cryogenic media for cooling as well as insulating HTS power devices operating at temperatures between 10-100 K, the typical temperature range of interest.

2.5 Dielectric Strength Model

Dielectric breakdown in gases between two electrodes can be described by the Townsend breakdown criterion. Figure 7 illustrates electron multiplication process that precedes a dielectric breakdown. Even in the absence of any applied electric fields, free electrons are generated at a certain rate by background and cosmic radiation as shown in the figure. The corresponding background current is i_0. When voltage is applied between the electrodes (higher potential at the anode), electrons are attracted to the anode. As electrons travel along the red arrow of Figure 7, they collide with gas particles and generate more free electrons by ionizing them. By the time the electrons arrive at the anode surface, the electron and ion currents are increased by $i_0(e^{\alpha d} - 1)$, where α is the ionization coefficient and d is the distance between the electrodes. Since ions are attracted to the cathode, the ion current of $i_0(e^{\alpha d} - 1)$ arrives at the cathode surface. As ions bombard the cathode surface, a fraction of them releases electrons from the surface. The chance of an ion releasing an electron is defined by

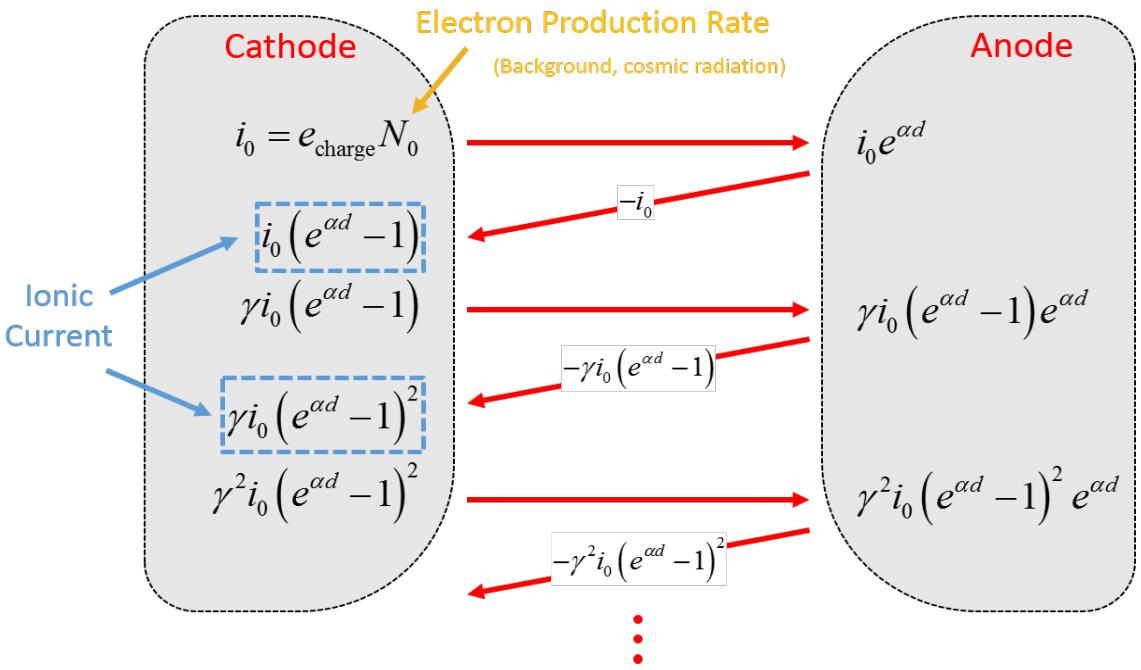

Figure 7: Electron multiplication between two electrodes.

γ, which is the secondary electron emission coefficient. The number of the secondary electrons at the cathode surface is $\gamma i_0(e^{\alpha d}-1)$, which increases exponentially as they travel across the gap. The process repeats indefinitely. Adding up all currents arriving at the anode surface forms a geometric series.

$$i_{anode} = \frac{i_0 e^{\alpha d}}{1-\gamma(e^{\alpha d}-1)} \tag{3}$$

From this equation, it can be seen that i_{anode} will go to infinity when the following condition is satisfied.

$$e^{\alpha d} = 1 + \frac{1}{\gamma} \tag{4}$$

The condition is also known as the Townsend breakdown criterion. To model the dielectric strength (*i.e.*, breakdown voltage), parameters in the pressure normalized

ionization coefficient α/p are required. Conventionally, the empirical formula of the pressure-normalized ionization coefficient

$$\alpha/p = Ae^{-Bp/E}, \tag{5}$$

which relates α/p to the applied pressure normalized electric field E/p, electrode gap distance d, and gas pressure p, has been used in the regression process for the approximation of parameters A and B [9, 28, 36, 43, 56, 57, 64, 74, 75, 78, 82, 89]. Some authors proposed the empirical formula

$$\alpha/p = Ae^{-B(p/E)^{1/2}} \tag{6}$$

for the regression process of noble gases [57, 78]. Once the values of A and B are known, the dielectric strength (*i.e.*, breakdown voltage) is obtained by the following equation.

$$V_{bd} = \frac{B}{k_o + ln(pd)}pd, \tag{7}$$

where $k_o = lnA - lnln(1 + 1/\gamma)$. This equation predicts the breakdown voltage as a function of the product of pressure and gap distance, pd, which is also known as Paschen's curve.

Accurately modeling the dielectric strength of gas mixtures is crucial for optimizing the voltage ratings of power applications. Accuracy in the regression process of α/p is a decisive factor for accurate approximation for A and B values, which determine the accuracy of dielectric strength estimation. However, the work presented here discovered that the conventional formulae of α/p do not provide the best accuracy in the regression process of α/p, and hence do not guarantee the best accuracy

in the values of A and B. To improve accuracy in the regression process, this study proposes a new formula that can adjust the sensitivity of the ionization coefficient to the applied electric field. The new formula incorporates a generalization factor m that adjusts the sensitivity of the ionization coefficient to the applied electric field as well as allows improved regression accuracy in α/p. Except for the fact that the new formula for α/p is used, the derivation of dielectric breakdown strength is similar to the conventional method, which is based on the Townsend breakdown criterion [56].

2.6 Plasma Parameter Diagnostics

Dielectric breakdown phenomena in gases occur in the form of plasma. In low gas pressures, a breakdown event can lead to a self-sustaining plasma, which manifests in the form of glow discharges that are used in halogen lamps and semiconductor processing devices [20, 21, 44, 61]. In high gas pressures, a breakdown event leads to the formation of arc discharges, which can be seen in lightings, abnormally disconnected high-voltage transmission lines, and high power switchgears. Hence, studying the parameters of plasmas provides understanding on plasma properties including plasma temperature (*i.e*, effective electron energy) and plasma density (*i.e*., electron density), which could be used for evaluating the dielectric properties of gases. For the measurement and characterization of plasmas, electrostatic probes (*i.e*., Langmuir probes) are essential [48–50, 62]. The fact that these probes could measure local plasma characteristics for a wide range of discharge conditions makes them powerful. The measurement procedure involves inserting the probe into a plasma. Inside a plasma, only the probe tip is exposed while the rest of the probe is electrically isolated from the plasma to minimize electric field distortions and plasma perturbations that could occur during the measurement. Plasma measurements generate I-V characteristic curves, which are measured by biasing the probe tip with a range of electric potential while measuring the probe current [29, 30]. Plasma parameters including

plasma temperature (T_e) and plasma density (n_e) are derived from the measured I-V data with the use of several techniques.

The classical Langmuir technique assumes a Maxwellian distribution for electron energies for the analysis of I-V curves. According to this method, plasma temperature T_e is defined as the inverse slope of a semi-logarithmic scale of an I-V curve [56].

$$T_e = \Big(\frac{d\ln I_e}{dV_p}\Big)^{-1} \tag{8}$$

Subsequently, by using the plasma temperature T_e data, plasma density n_e can be derived from the electron saturation current [56].

$$I_{es} = \frac{1}{4} e n_e A_p \sqrt{\frac{8eT_e}{\pi m_e}} \tag{9}$$

Another technique that is used in obtaining the plasma parameters is by using the ion part of the I-V characteristic curve. This method finds the plasma temperature T_e from the slope of the I-V characteristics curve near floating potential V_f [29].

$$T_e = eI_i\Big(\frac{dI_e}{dV_p}\Big)^{-1} \quad at \quad V_p = V_f, \tag{10}$$

where I_i is either approximated by a linear or parabolic extrapolation of ion current towards the plasma potential.

Unfortunately, these conventional techniques have been proven to be limited in applicability and accuracy. The limitation in the classical Langmuir technique is due to the fact that it applies only when the electron distributions are Maxwellian. But most low-temperature plasmas are not in thermal equilibrium and their electron distribution functions are not Maxwellian, rendering the classical Langmuir technique

not suitable for such plasmas [29]. The technique that uses the ion part of the I-V characteristic curve is also not accurate since the probe current near the floating potential V_f mainly consists of high-energy electrons rather than including electrons in the entire range of electron energy. Since this method does not utilize the entire I-V curve, where also low-energy electron information exists, the estimated electron temperatures are generally higher than the actual electron temperature. As reported by Godyak *et al*. [29], the Druyvesteyn method is a technique that can be applied to arbitrary electron energy distribution functions. The Druyvesteyn method is based on the fact that EEDF's are proportional to the second-order derivative of I-V characteristic curves.

$$f(\epsilon) \propto \frac{d^2 I_e}{dV_p^2} \tag{11}$$

This method does not assume any specific type of electron distribution function and uses the entire I-V curve, not just a portion of it. The plasma parameters including the plasma temperature and plasma density obtained through the Druyvesteyn method are not confined to Maxwellian EEDF nor limited to high or low energy electrons of a measured I-V curve. The Druyvesteyn method remains the only useful technique for experimental studies on EEDF and has been widely used for studying low-temperature and non-thermal-equilibrium plasmas [48–50].

Since dielectric breakdown events in gases such as arc, corona, surface flashover, partial discharge are all in the form of plasmas, measuring plasmas is a way of studying the dielectric characteristics of the gases that were used to generate the plasmas. In this dissertation, low-pressure dc plasmas containing the mixtures of potential gaseous cryogens are measured and analyzed using the Druyvesteyn method.

CHAPTER III

RESEARCH OBJECTIVES

The dielectric properties of gaseous cryogens are related to the electron kinetic processes that describe the growth of electron ensemble in gaseous environments. Studying the electron kinetics involves numerically solving the Boltzmann equation with a simplification method known as the two term approximation. This approach, also known as the Boltzmann analysis, requires the electron scattering cross section data of gas species as an input for solving the Boltzmann equation. The solution of the Boltzmann analysis is the electron energy distribution function (EEDF), which contains the most complete set of information regarding the electron ensemble of a gas. EEDF's are subsequently used for the calculation of electron kinetics coefficients that are used to compare the dielectric properties of cryogenic gas mixtures.

Although the coefficients of electron kinetics provide a good qualitative understanding for the dielectric behavior of gas mixtures, these coefficients cannot provide the quantitative predictions of dielectric strength such as breakdown voltages. Gas dielectric models have been developed in the past, but the conventional models cannot accurately predict the dielectric strength of gases: neither can they estimate dielectric variations when gas composition changes. To improve the dielectric strength estimation performance, this study introduces a new modeling procedure, which can predict the dielectric strength of gasses and its variation as a function of the composition of gas mixtures.

In addition to the theoretical approaches for improving the dielectric properties of cryogenic gases, an experimental plasma diagnostics method is utilized to estimate the electron kinetics of gas mixtures. A dc plasma experiment is designed, which includes

the development of electrostatic probes, a plasma chamber, and a gas mixing system. The experiment, known as the Langmuir probing method, derives the plasma density and plasma temperature, which are essential in predicting the dielectric strength of gas mixtures.

The primary objectives of this dissertation are:

- To predict and map dielectric strength variations in potential gaseous cryogens under various cryogenic operating conditions while preventing condensation (Chapters 4–6).
- To develop a dielectric strength model that is more accurate than the conventional models and capable of tracking the dielectric strength variation in gas mixtures when gas composition changes (Chapter 7).
- To design and conduct plasma experiments to obtain the electron energy distribution functions and plasma parameters, which are used for evaluating the dielectric behavior of gas mixtures (Chapter 8).

The outline of the succeeding chapters is listed below.

- Chapter 4 investigates the variation in the dielectric properties of potential binary and ternary cryogenic gas mixtures.
- Chapter 5 discusses the methodology for identifying gas compositions suitable for a given temperature and pressure primarily to prevent condensations under cryogenic operating conditions.
- Chapter 6 maps the maximum-achievable dielectric strength of gas mixtures over the wide range of cryogenic operating conditions.

- Chapter 7 presents a new dielectric strength model that provides improved accuracy in estimating the dielectric strength of pure gases and the capability of tracking the variation of dielectric strength in gas mixtures.
- Chapter 8 develops a plasma diagnostics experiment for evaluating the dielectric properties of gas mixtures by measuring the electron energy distribution function.
- Chapter 9 draws broad conclusions of the dissertation.
- Chapter 10 discusses the future outlook of this research and potential topics that need to be studied to further the understanding on dielectric gases.
- Chapter 11 lists all journal and conference papers published by the author.

CHAPTER IV

DIELECTRIC PROPERTIES OF BINARY AND TERNARY GAS MIXTURES

4.1 Motivation

As discussed in Chapter 1, the relatively weak dielectric strength of gaseous cryogens is one of the major challenges for the realization and the wide-spread application of gas-cooled HTS power devices. With the goal of developing a process for identifying gaseous cryogenic media with improved dielectric strength, this chapter discusses the dielectric properties of various mixtures of potential gaseous cryogens for high-temperature superconducting (HTS) power applications. The study analyzes the electron kinetics of cryogenic gas mixtures to understand the dielectric breakdown phenomena in gases and the key factors that determine the dielectric strength of gases. Using the knowledge of electron kinetics, the study predicts dielectric strength variations in the binary and ternary mixtures of cryogenic gases. The analysis involves solving the Boltzmann equation with the two-term approximation method based on the electron scattering cross section data of gas species in question. The study provides insights into important characteristics and correlations that lead to the enhanced dielectric strength of gas mixtures and predicts further enhancements in the dielectric strengths of binary mixtures by introducing various tertiary gas species. The results of the study will aid in the development of HTS power applications incorporating gaseous cryogens.

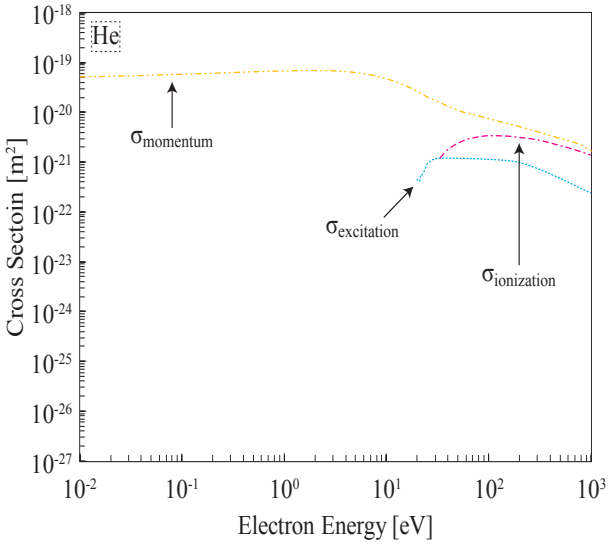

Figure 8: The electron scattering cross section of He. [5]

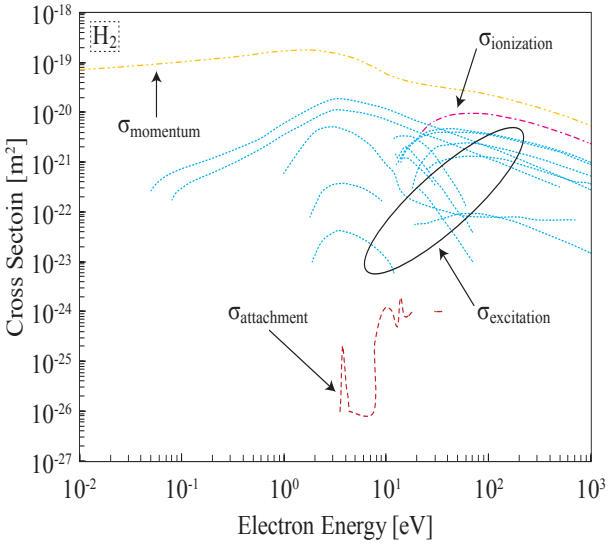

Figure 9: The electron scattering cross section of H_2. [5, 95]

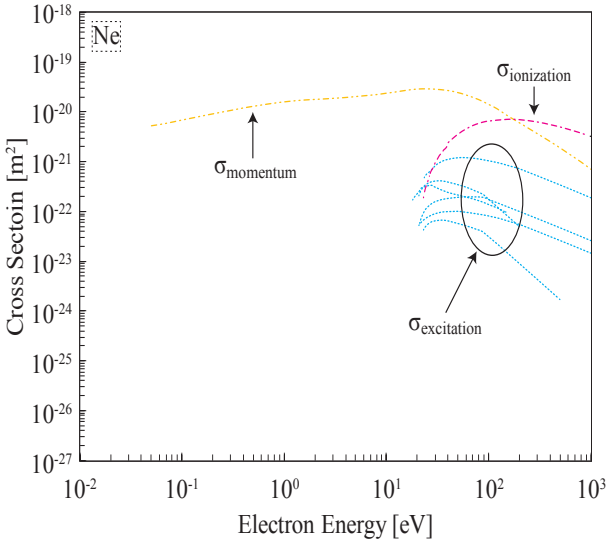

Figure 10: The electron scattering cross section of Ne. [2]

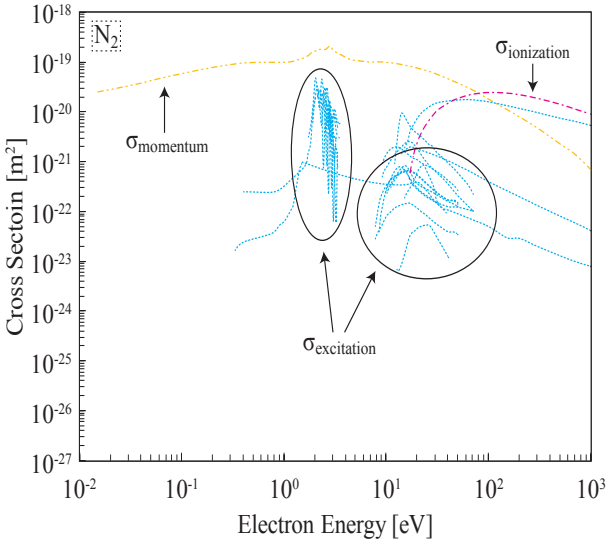

Figure 11: The electron scattering cross section of N_2. [2]

4.2 Possible Gaseous Cryogens

4.2.1 Electron Scattering Cross Sections

Figures 8-11 show the electron scattering cross section data of He, H_2, Ne, and N_2. The data are chosen from numerous datasets available in the LXcat database [1]. For the work discussed in the dissertation, the cross section data from Phelps database [5]

was used for the analysis of He and H_2 (the attachment electron scattering cross section of H_2 is from Yoon *et al.* [95]), and those from SIGLO database [2] for Ne and N_2. All of the four gas species show large momentum-transfer electron scattering cross sections over the entire electron energy range and ionization electron scattering cross sections at a relatively high electron energy. Note that although the electron scattering cross sections stop at 1,000 eV in the figures, there is no physical limit of electron energy. It should be also noted that the excitation electron scattering cross section of He in Figure 8 is a summation of all excitation electron scattering cross sections. A comparison between the electron scattering cross sections of monatomic gases (He and Ne) to diatomic gases (H_2 and N_2) indicates that diatomic gases (*i.e.*, molecular gases) have numerous vibrational and rotational excitation electron scattering cross sections in addition to the electronic excitation cross sections, both of which contribute to the electron energy dissipation that leads to higher dielectric strength.

4.2.2 Validity of the Computation Method

This section confirms the validity of the electron scattering cross section data and the accuracy of the computation method (*i.e.*, Boltzmann analysis with the two-term approximation method) by comparing the calculated α/N values of He, H_2, Ne, and N_2 to those from the literature [8, 10, 16, 17, 22, 40, 41, 46, 56, 58, 85, 90], as presented in Figures 12 and 13.

The calculated α/N values of He show a close agreement with those in the literature [8,17,22,56] with a higher degree of agreement with the data from Phelps *et al.* [8] (Figure 12). The α/N values of H_2 obtained in this study and the literature [56,58,90] also show a close agreement except with the values reported by Engel *et al.* [90], which deviate from the rest at E/N lower than 250 Td (Figure 12). The α/N values of Ne and N_2 are also compared with those in the literature [10, 16, 40, 41, 46, 56, 85, 90], which show a close agreement (Figure 13). Note that the α/N of H_2 exceeds that

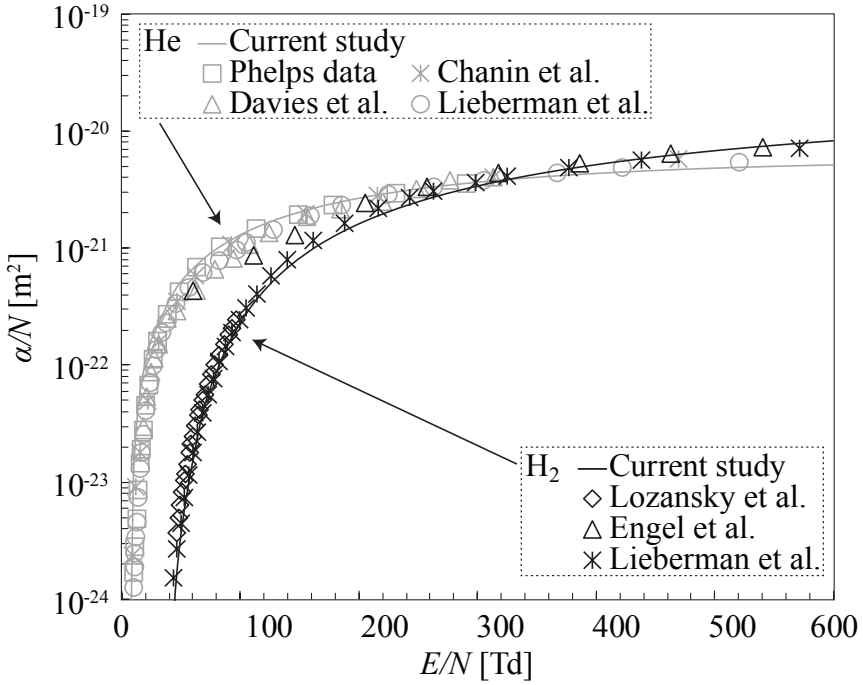

Figure 12: Comparison between the density-reduced ionization coefficient values of He and H_2 from the current study and those from the literature. (Phelps data, [8] Chanin *et al.*, [17] Davies *et al.*, [22] Lieberman *et al.*, [56] Lozansky *et al.*, [58] Engel *et al.* [90])

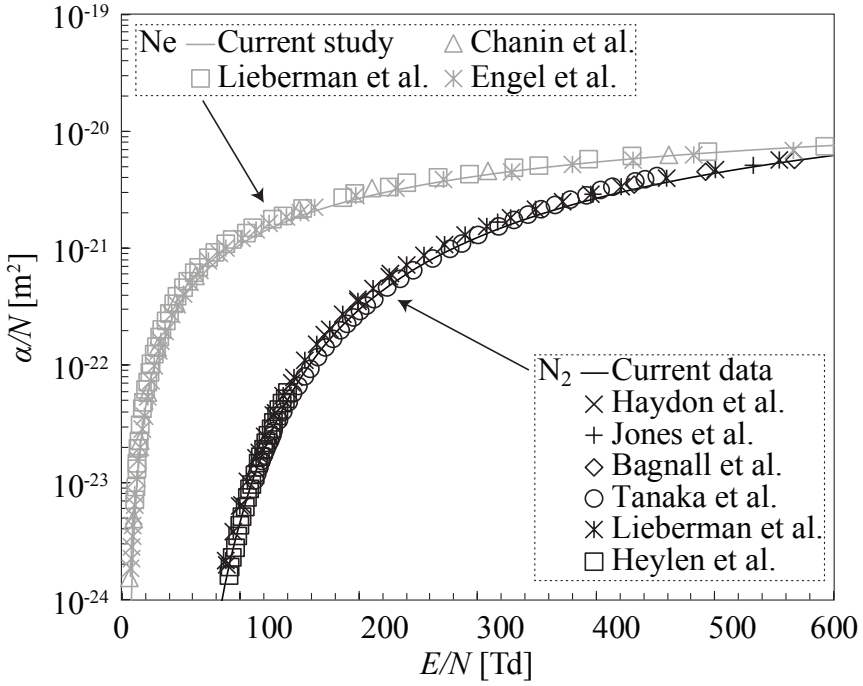

Figure 13: Comparison between the density-reduced ionization coefficient values of Ne, N_2 from the current study and those from the literature. (Chanin *et al.*, [16] Lieberman *et al.*, [56] Engel *et al.*, [90] Haydon *et al.*, [40] Jones *et al.*, [46] Bagnall *et al.*, [10] Tanaka *et al.*, [85] Heylen *et al.* [41])

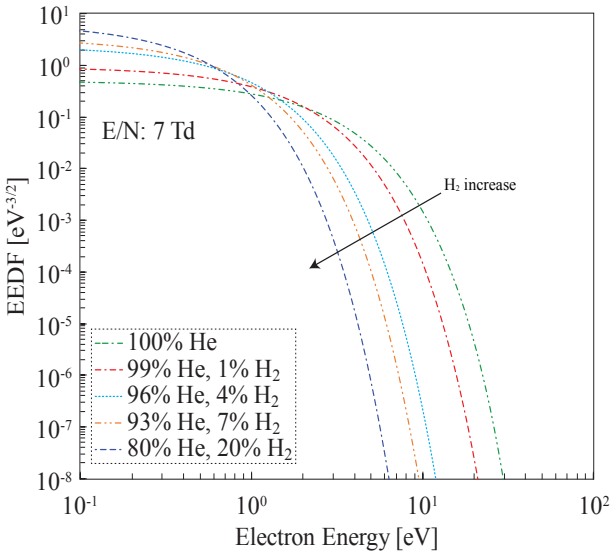

Figure 14: Correlation between the amount of H_2 in the binary gas mixture and the electron energy distribution function.

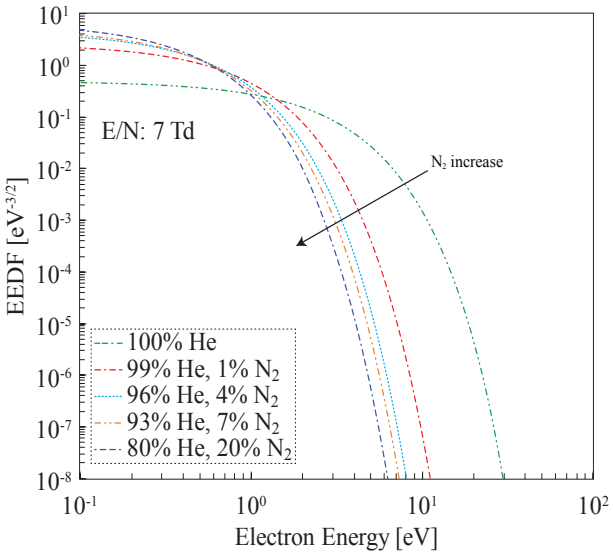

Figure 15: Correlation between the amount of N_2 in the binary gas mixture and the electron energy distribution function.

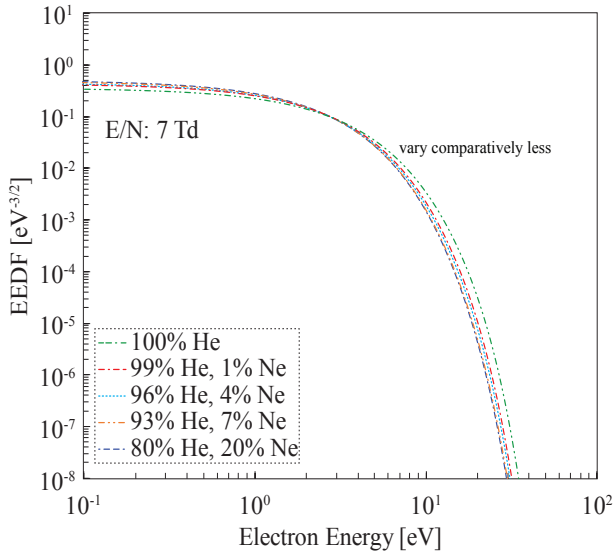

Figure 16: Correlation between the amount of Ne in the binary gas mixture and the electron energy distribution function.

of He above 350 Td, which is likely due to the large ionization electron scattering cross section of H_2 compared to that of He combined with the decreasing excitation electron scattering cross sections of H_2 at higher electron energy (Figures 8 and 9). A similar reasoning is valid for understanding the trend of α/N for N_2, which increases

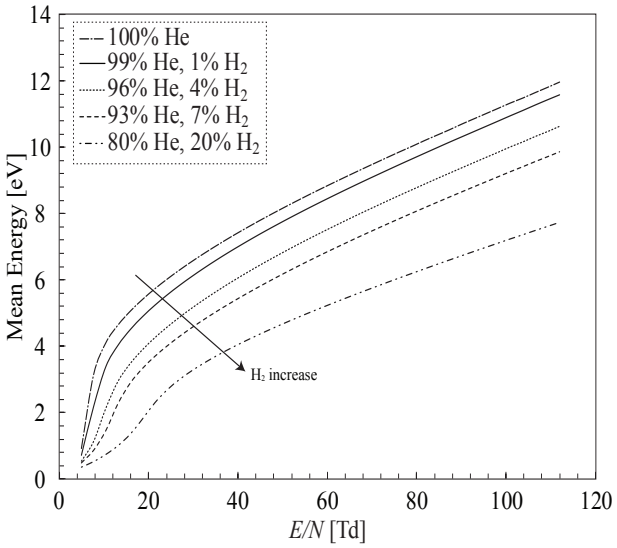

Figure 17: Correlation between the amount of H_2 in the binary gas mixture and the mean electron energy.

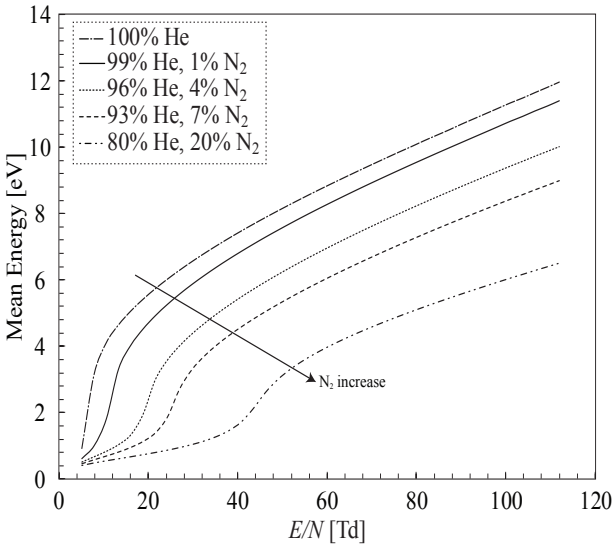

Figure 18: Correlation between the amount of N_2 in the binary gas mixture and the mean electron energy.

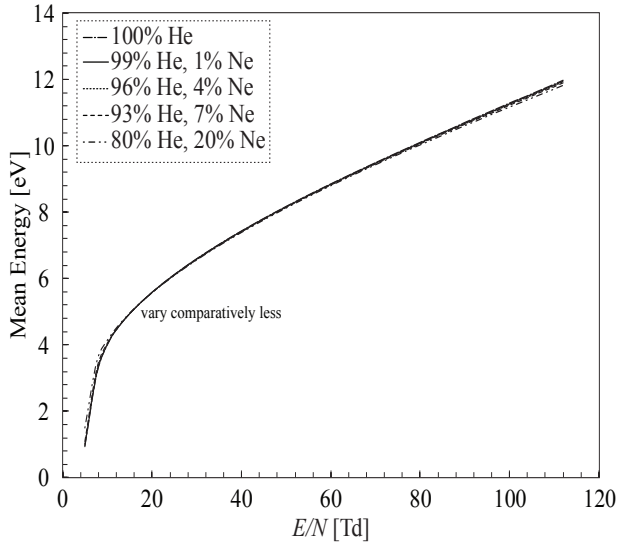

Figure 19: Correlation between the amount of Ne in the binary gas mixture and the mean electron energy.

more rapidly than that of Ne at high E/N (Figures 10 and 11).

The agreement between the results obtained from the calculations of this study and those from the literature confirms that the computation method used in the dissertation is valid and suitable for furthering the investigation.

4.3 Dielectric Properties of Binary Gas Mixtures

4.3.1 Electron Energy Distribution Function and Mean Electron Energy

Variations in the EEDF and the mean electron energy of binary gas mixtures including He-H_2, He-N_2, and He-Ne mixtures with the E/N of 7 Td obtained from the Boltzmann analysis are presented in Figures 14-16 and Figures 17-19, respectively. EEDF shifts to a lower energy region (direction of the arrow) with its values increasing in lower electron energy and decreasing in higher electron energy as the mole fractions of H_2 and N_2 increase in He-H_2 and He-N_2 mixtures (Figures 14 and 15). The results demonstrate a negative correlation between the mean electron energies of the gas mixtures and the mole fractions of H_2 and N_2 (Figures 17 and 18).

Unlike in the He-H_2 and He-N_2 gas mixtures, a comparatively small variation is observed in the values of EEDF, which slightly shifts to a higher energy region, as the mole fraction of Ne increases in the He-Ne mixture (Figure 16). The results indicate a relatively weak correlation between the mole fraction of Ne and the mean electron energy of the gas mixture (Figure 19).

4.3.2 Density-Reduced Ionization Coefficient

Figures 20-22 show α/N values calculated based on the EEDF of He-H_2, He-N_2, and He-Ne mixtures, respectively, as a function of E/N. The results show that α/N values decrease (direction of the arrow) as the mole fractions of H_2 and N_2 increase in the He-H_2 and He-N_2 mixtures, which indicate a negative correlation between the mole fractions of H_2 and N_2, and the α/N values of the gas mixtures (Figures 20 and 21).

Unlike the α/N values of the He-H_2 and He-N_2 gas mixtures, those of the He-Ne gas mixture show a comparatively small variation with values slightly increasing in the lower E/N range as the mole fraction of Ne increases (Figure 22). The results show a relatively weak correlation between the mole fraction of Ne and the α/N values of the gas mixture. This trend is consistent with that seen in the results of the EEDF

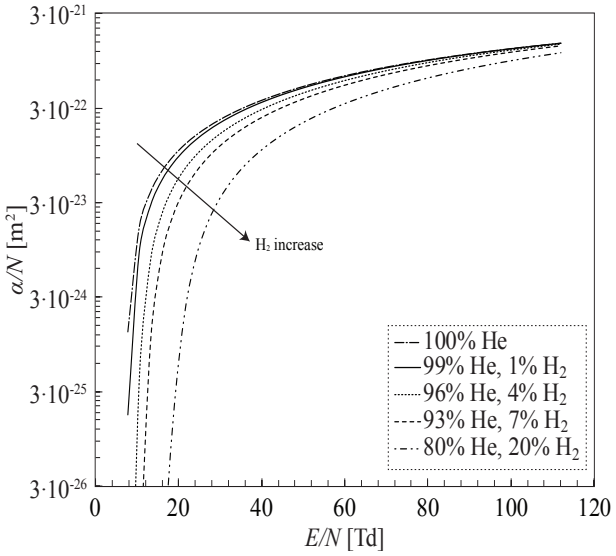

Figure 20: Correlation between the amount of H_2 in the binary gas mixture and density-reduced ionization coefficient α/N.

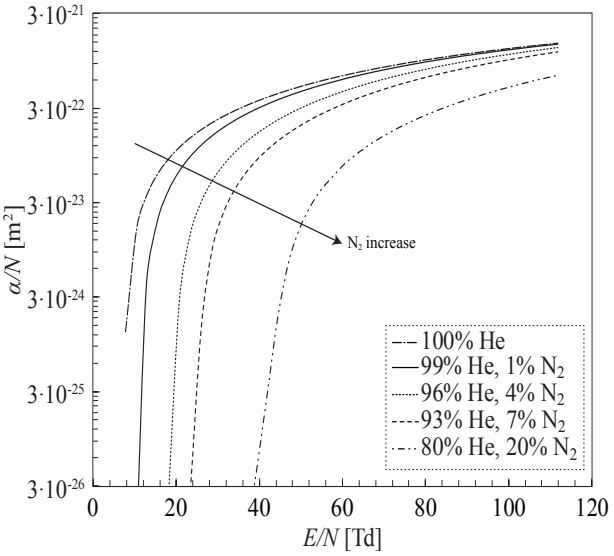

Figure 21: Correlation between the amount of N_2 in the binary gas mixture and density-reduced ionization coefficient α/N.

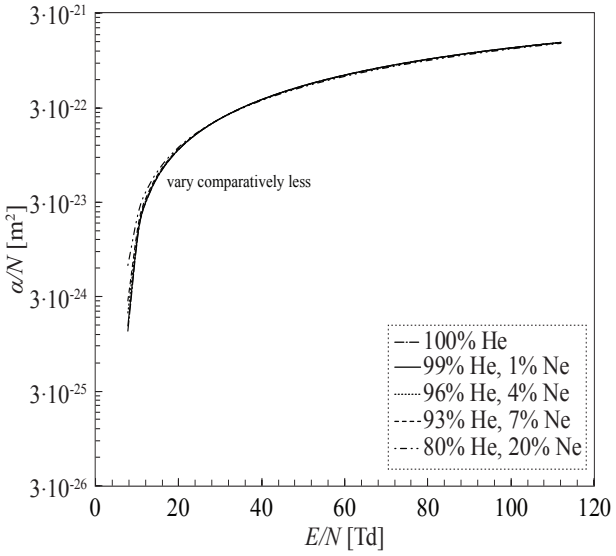

Figure 22: Correlation between the amount of Ne in the binary gas mixture and density-reduced ionization coefficient α/N.

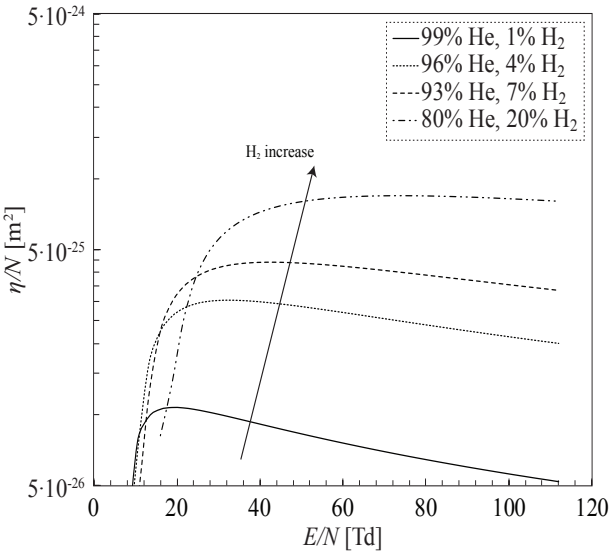

Figure 23: Correlation between the amount of H_2 in the binary gas mixture and density-reduced attachment coefficient η/N.

discussed in the previous section.

Table 1: $(E/N)_{cr}$ of the Binary Gas Mixtures

$He:H_2$ [mol%]	99:1	96:4	93:7	80:20
$(E/N)_{cr}$ [Td]	7.1	9.5	11.6	18.5

4.3.3 Density-Reduced Attachment Coefficient

The η/N values of He-H_2 gas mixtures calculated from the EEDF are presented in Figure 23 as a function of E/N. It should be noted that η/N values do not exist for He-N_2 or He-Ne mixtures since the gases in these mixtures do not have attachment electron scattering cross sections. The calculated η/N values increase (direction of the arrow) as the mole fraction of H_2 increases in the He-H_2 mixture, which shows a positive correlation between the mole fraction of H_2 and the η/N of the gas mixture.

4.3.4 Density-Reduced Effective Ionization Coefficient and Density-Reduced Critical Electric Field

From the results of α/N and η/N, the values of $(\alpha - \eta)/N$, which represent the net ionization process, are calculated. The binary gas mixture of He-H_2 shows a decrease in $(\alpha - \eta)/N$ values as the mole fraction of H_2 increases. This finding indicates that $(\alpha - \eta)/N$ values become positive at higher E/N as the mole fraction of H_2 increases. The variation in $(\alpha - \eta)/N$ is mainly caused by the reduction in α/N and the increase in η/N (Figures 20 and 23). As a result, $(E/N)_{cr}$, the value of E/N corresponding to the rate of ionization collisions equivalent to that of attachment collisions, increases as the mole fraction of H_2 increases in the gas mixture, as shown in Table 1.

4.3.5 Interpretation of the Binary Mixture Results

The collective trend observed in the previous sections shows increasing dielectric strength with the increasing mole fractions of H_2 and N_2 in the mixtures. The results of the EEDF presented in Figures 14 and 15 can be explained mainly by the various types of excitation electron scattering cross sections existing in H_2 and N_2 (Figures 9 and 11). Each excitation collision results in the consumption of electron energy

equivalent to the threshold energy of the corresponding excitation collision in addition to the transfer of kinetic energy. The dissipation of electron energy through this process is the main cause of the reducing trend of the mean electron energies shown in Figures 17 and 18. This trend is promising from the viewpoint of dielectric strength since decreasing mean electron energy leads to a corresponding reduction in the rate of ionization collisions (Figures 20 and 21), a key process that develops into a dielectric breakdown. The results are also, to some extent, influenced by the relatively large momentum-transfer electron scattering cross sections of H_2, which span over the entire range of electron energy, and those of N_2, which range from 0.1–400 eV, compared to those of He. In addition, the attachment electron scattering cross sections of H_2 located in the range of electron energy between 3.5–18 eV contribute to the removal of electrons within that energy range.

Relatively small variations are seen in the results of the increasing mole fractions of Ne (Figures 16,19, and 22). These results are mainly due to the excitation electron scattering cross sections of Ne concentrated in the electron energy range above 16.62 eV, which is similar to those of He (Figures 8 and 10). The similarity in the excitation electron scattering cross sections of the two gases causes a comparatively minute variation in the electron energy dissipation process (*i.e.*, collision process), since both He and Ne allow electrons to gain energy as high as 16-19 eV without substantial dissipation of energy by excitation collisions and by a loss of only a negligible amount of kinetic energy (on the order of 10^{-4} times the kinetic energy of an electron) through elastic collisions. The slight increase in the EEDF at electron energy above 3 eV, shown in Figure 16, could be partially due to the relatively small momentum-transfer electron scattering cross sections of Ne below 20 eV, at which kinetic energy transfers are mainly caused by elastic collisions. In addition, the slightly increasing α/N values in the low E/N range, shown in Figure 22, are likely due to the lower ionization threshold energy and larger ionization electron scattering cross section of

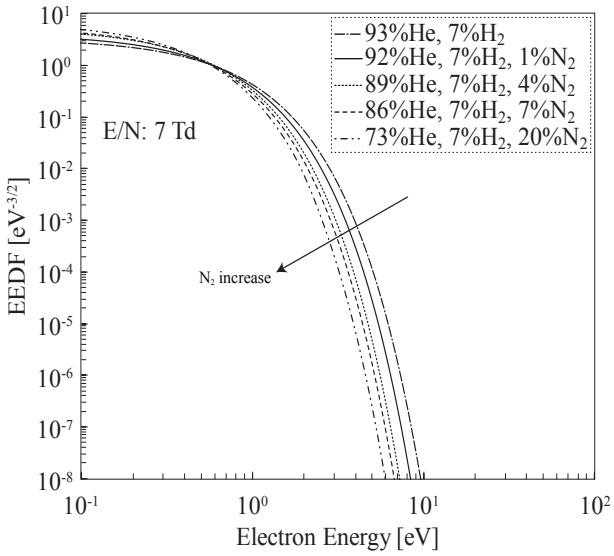

Figure 24: Correlation between the amount of N_2 in the He-H_2-based ternary gas mixture and the electron energy distribution function.

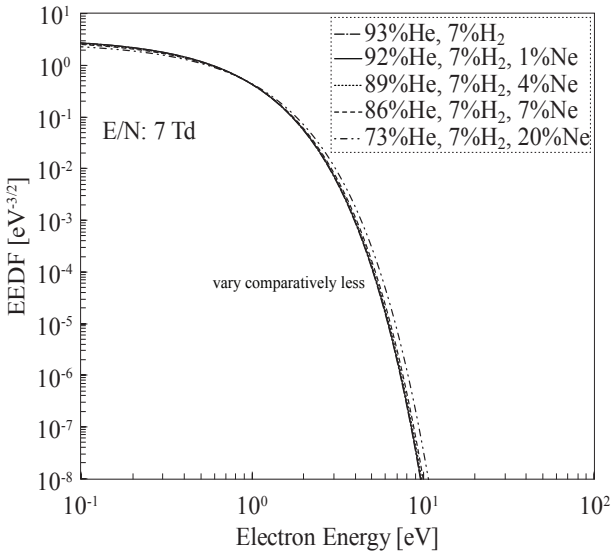

Figure 25: Correlation between the amount of Ne in the He-H_2-based ternary gas mixture and the electron energy distribution function.

Ne than those of He.

EEDF showing larger values at low electron energy, smaller α/N and $(\alpha - \eta)/N$, and larger η/N and $(E/N)_{cr}$ are the indications of an increasing dielectric strength. According to the results discussed in this section, mixing either H_2 or N_2 with He increases the dielectric strength of a gas mixture. In an effort to explore opportunities for further enhancements in dielectric strength, the study continues to examine He-H_2-based ternary gas mixtures in the following section.

4.4 Dielectric Properties of Ternary Gas Mixtures

4.4.1 Electron Energy Distribution Function and Mean Electron Energy

The EEDF and mean electron energy of the ternary gas mixtures of He-H_2-N_2 and He-H_2-Ne are shown in Figures 24–25 and Figures 26–27, respectively. A fixed 7 mol% of H_2 is selected for the study as it is the reported maximum amount of H_2 that can be used without any risk of flammability [70, 86]. With the fixed mole fraction of H_2, either the He-N_2 or He-Ne gas mixture is added with various combination ratios.

The results presented in Figure 24 show that the EEDF shifts to the lower energy

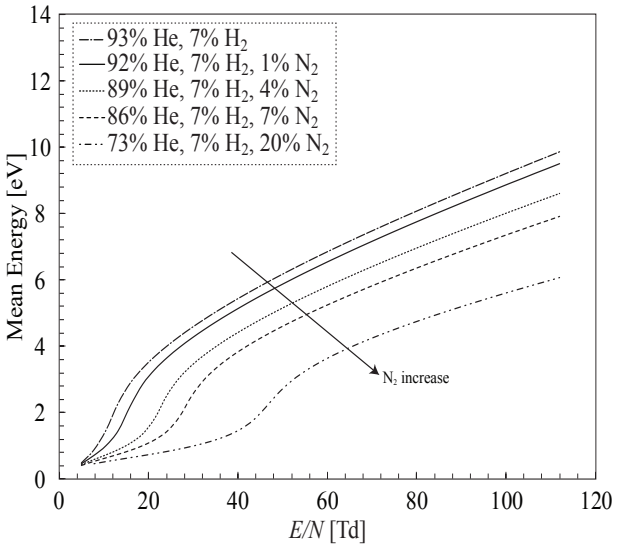

Figure 26: Correlation between the amount of N_2 in the He-H_2-based ternary gas mixture and the mean electron energy.

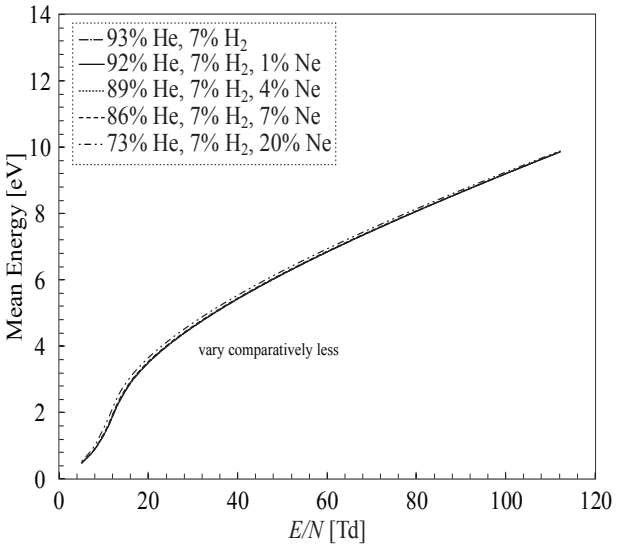

Figure 27: Correlation between the amount of Ne in the He-H_2-based ternary gas mixture and the mean electron energy.

region (direction of the arrow) with increasing values at electron energy below 0.6 eV and decreasing values at electron energy above 0.6 eV as the mole fraction of N_2 increases in the He-H_2-N_2 mixture. Note that the mole fraction of He decreases as the mole fraction of N_2 increases to balance the mixture. The result demonstrates that a negative correlation exists between the mole fraction of N_2 and the mean electron energy of the He-H_2-N_2 gas mixture (Figure 26).

Unlike the variations seen in the EEDF of the He-H_2-N_2 mixture, the variation in the EEDF of the He-H_2-Ne mixture is comparatively small, slightly shifting to the higher energy region with values above 1 eV slightly increasing as the mole fraction of Ne increases (Figure 25). The results indicate a relatively less distinct correlation between the mole fraction of Ne and the mean electron energy of the He-H_2-Ne gas mixture (Figure 27).

4.4.2 Density-Reduced Ionization Coefficient

The α/N values of the ternary gas mixtures of He-H_2-N_2 and He-H_2-Ne are presented as functions of E/N in Figures 28 and 29, respectively. The results show that α/N

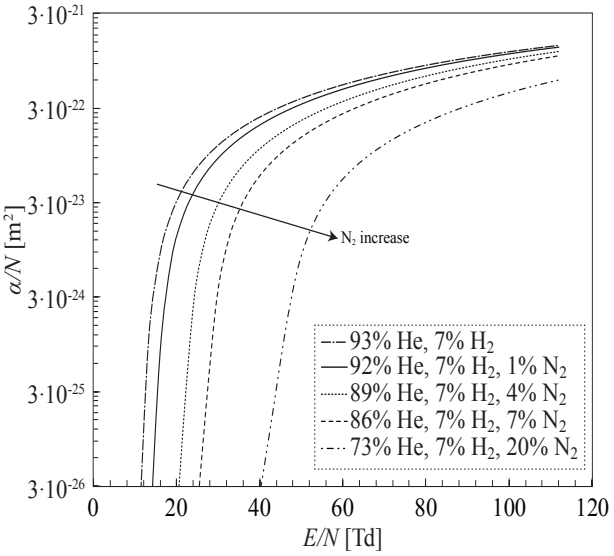

Figure 28: Correlation between the amount of N_2 in the He-H_2-based ternary gas mixture and density-reduced ionization coefficient α/N.

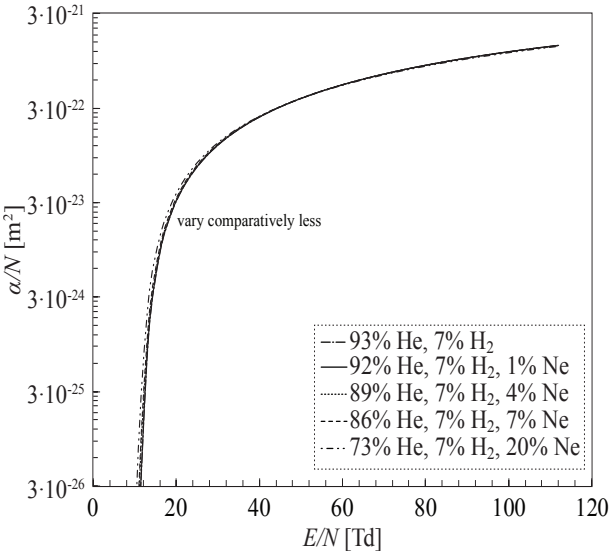

Figure 29: Correlation between the amount of Ne in the He-H_2-based ternary gas mixture and density-reduced ionization coefficient α/N.

decreases (direction of the arrow) with an increase in the mole fraction of N_2 in the He-H_2-N_2 mixture, which indicate a negative correlation between the mole fraction of N_2 and α/N of the gas mixture (Figure 28).

Unlike the α/N values of the He-H_2-N_2 mixture, those of the He-H_2-Ne mixture slightly increase at E/N below 40 Td as the mole fraction of Ne increases (Figure 29). The results exhibit a relatively weak correlation between the mole fraction of Ne and the α/N values of the He-H_2-Ne mixture, which are consistent with the results of the EEDF and the mean electron energy of the He-H_2-Ne gas mixture discussed in the previous section.

4.4.3 Density-Reduced Attachment Coefficient

The η/N values of the ternary gas mixtures of He-H_2-N_2 and He-H_2-Ne are presented in Figures 30 and 31, respectively. The results show that η/N decreases (direction of the arrow) as the mole fraction of N_2 in the He-H_2-N_2 mixture increases, which indicate a negative correlation between the mole fraction of N_2 and the η/N of the

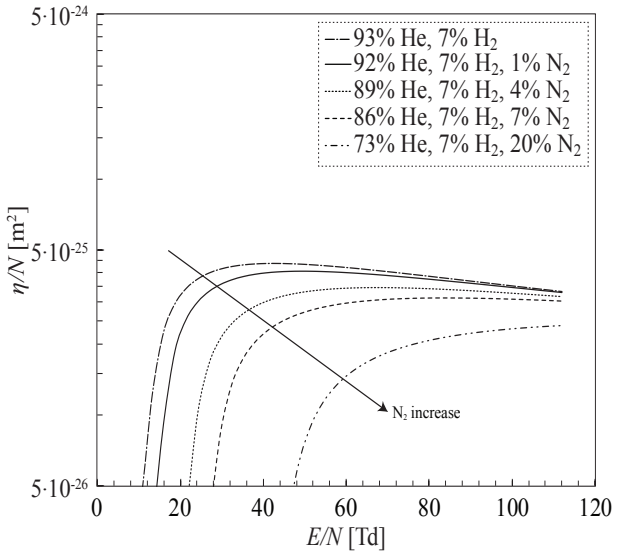

Figure 30: Correlation between the amount of N_2 in the He-H_2-based ternary gas mixture and density-reduced attachment coefficient η/N.

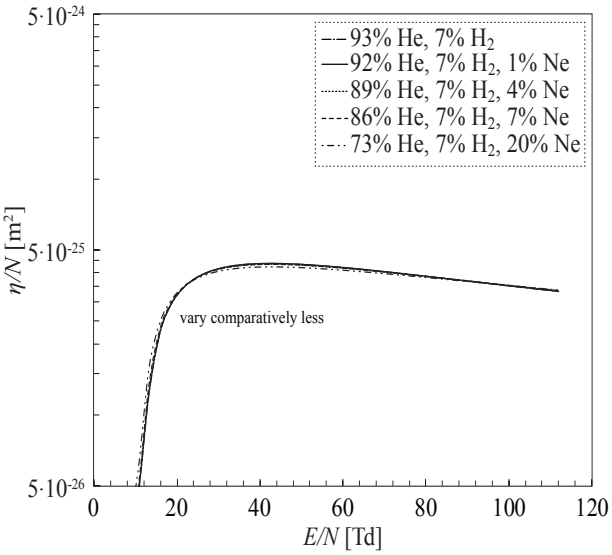

Figure 31: Correlation between the amount of Ne in the He-H_2-based ternary gas mixture and density-reduced attachment coefficient η/N.

gas mixture (Figure 30).

Unlike the η/N values of the He-H_2-N_2 mixture, those of the He-H_2-Ne mixture show a comparatively small variation as the mole fraction of Ne increases, which indicate a relatively weak correlation between the mole fraction of Ne and the η/N of the He-H_2-Ne mixture (Figure 31). The results are consistent with those of the EEDF and the mean electron energy of the He-H_2-Ne gas mixture, which also exhibit a weak correlation with the increasing mole fraction of Ne, as discussed in the previous section.

4.4.4 Density-Reduced Effective Ionization Coefficient and Density-Reduced Critical Electric Field

From the previous results of α/N and η/N, the study calculates the $(\alpha-\eta)/N$ values of the ternary gas mixtures of He-H_2-N_2 and He-H_2-Ne and predict a decrease in the $(\alpha-\eta)/N$ values of the He-H_2-N_2 mixture as the mole fraction of N_2 increases. This finding indicates that $(\alpha-\eta)/N$ values become positive at higher E/N as the mole fraction of N_2 increases. The variation in $(\alpha-\eta)/N$ is mainly caused by the reduction

Table 2: $(E/N)_{cr}$ of the Ternary Gas Mixtures

$He:H_2:N_2$ [mol%]	93:7:0	92:7:1	89:7:4	86:7:7	73:7:20
$(E/N)_{cr}$ [Td]	11.0	13.7	19.8	24.5	40.0
$He:H_2:Ne$ [mol%]	93:7:0	92:7:1	89:7:4	86:7:7	73:7:20
$(E/N)_{cr}$ [Td]	11.0	10.9	10.9	10.8	10.8

in α/N, which is several orders of magnitude greater than that in η/N (Figures 28 and 30). As a result, $(E/N)_{cr}$ increases as the mole fraction of N_2 increases in the gas mixture as presented in the first row of Table 2.

In the previous sections, EEDF, α/N, and η/N showed a relatively subtle correlation with the increasing mole fraction of Ne. Hence, the study predicts a relatively subtle change in the $(\alpha - \eta)/N$ values of the He-H_2-Ne mixture. As expected, the values of $(E/N)_{cr}$ show a comparatively small variation with the increase in the mole fraction of Ne as presented in the second row of Table 2.

4.4.5 Interpretation of the Ternary Mixture Results

The results of the ternary gas mixtures show a trend similar to those of the binary mixtures. A decrease in α/N and $(\alpha - \eta)/N$, which indicate an enhancement in dielectric strength, are observed as the mole fraction of N_2 increases in the He-H_2-based ternary gas mixture. The increase in dielectric strength with the addition of N_2 is mainly due to the numerous excitation electron scattering cross sections of N_2 dissipating electron energy. A notable result is that η/N decreases as the mole fraction of N_2 increases in the He-H_2-N_2 mixture. This finding is likely due to the substantial electron energy dissipation caused by numerous excitation collision processes resulting from the increase in N_2, which reduces the mean electron energy of the He-H_2-N_2 mixture below the electron energy, in which attachment collisions mainly occur (*i.e.*, 3.5–18 eV). This finding is counterintuitive because a decrease in η/N is not necessarily an indication of an enhancement in the dielectric strength. Nevertheless, the increasing mole fraction of N_2 enhances the dielectric strength of the

ternary gas mixture because the effect of the reduction in η/N is negligible compared to that in α/N.

The results show a relatively less obvious influence of the increasing mole fraction of Ne in the ternary gas mixtures, which is consistent with the results of the binary gas mixtures. The similarity in the results of both binary and ternary gas mixtures is primarily due to the similarity in the range of electron energy, in which the excitation electron scattering cross sections of Ne and those of He are located (Figures 8 and 10). In other words, the electron energy dissipation and the variation in dielectric strength resulting from the addition of Ne are similar to those resulting from the addition of He. A relatively small increase in α/N and η/N is observed below 20 Td (Figures 29 and 31), which is likely due to the slightly increasing values of the EEDF above 1 eV (Figure 25) and those of the mean electron energy (Figure 27).

4.5 Summary

The results of the study presented in this chapter showed an overall trend of decreasing EEDF, mean electron energy, α/N, and $(\alpha - \eta)/N$, but increasing $(E/N)_{cr}$ with the increasing mole fractions of H_2 and N_2 in the binary and ternary gas mixtures. On the contrary, an increase in the mole fraction of Ne caused a relatively weak variation in the dielectric properties of both the binary and ternary gas mixtures. The collective trend in the electron kinetic parameters indicated that the dielectric strength increases as the mole fractions of H_2 and N_2 increase in the gas mixtures; however, a relatively weak correlation exists between the mole fraction of Ne and the dielectric strengths of the gas mixtures. The difference was mainly caused by the existence of various vibrational and rotational excitation modes in molecular gases (*i.e.*, H_2 and N_2) and the lack of those excitation modes in monatomic gases (*i.e.*, He and Ne). The study analyzed the results in detail based on the electron scattering cross section data and the associated energy losses of each gas species.

The results and the correlations identified through this study serves as a guideline for identifying the potential gas mixtures with enhanced dielectric strength in He-based binary and ternary gas mixtures containing various mole fractions of H_2, Ne, and N_2. The study results are useful for the development of gaseous cryogen-cooled HTS power applications with higher operating voltages, and aid in the dielectric design of superconducting power applications incorporating gaseous cryogens.

CHAPTER V

PREVENTING POTENTIAL CONDENSATIONS IN CRYOGENIC GAS MIXTURES

5.1 Motivation

According to the results of the binary and ternary gas mixtures presented in the previous chapter, gaseous H_2 and N_2 contribute to dielectric strength enhancements mainly because these gases have various excitation electron scattering cross sections that substantially dissipate electron energy, which results in the reduction of mean electron energy and α/N. Therefore, the He-H_2-N_2 gas mixture can reach the maximum dielectric strength of a gaseous cryogen by increasing the mole fractions of H_2 and N_2 to their maximum. However, one of the issues of incorporating N_2 into a cryogenic gas mixture is the high boiling point (*i.e.*, low vapor pressure) of N_2, 77 K at 1 atm, compared to that of the rest of the gas species in this study. The higher boiling point indicates that maintaining the gas phase of pure N_2 below 77 K at 1 atm is impossible. Nevertheless, incorporating N_2 is not completely impossible if the mole fractions of N_2 are limited and the rest is mixed with gas species that have relatively high vapor pressures. That is, it is necessary to limit the mole fractions of N_2 or any potential gas constituents with low vapor pressures such that they will not condense under the potential operating conditions of cryogenic systems. To identify the mole fractions limit of constituent gases, the study calculates the vapor pressure of each constituent gas and then the condensation pressure of their mixtures. Once the condensation points are calculated, the maximum allowed mole fractions of constituent gas species are determined by the gas pressure and gas temperature. This chapter presents the estimated vapor pressures and dew points of the He-H_2-N_2 gas mixtures

and identifies the maximum allowed amount of N_2 that can be used over the range of cryogenic operating conditions. Subsequently, the corresponding dielectric strength of the mixture under such conditions is discussed.

5.2 Condensation Conditions

To estimate the condensation conditions, vapor pressures of each constituent gas species are required. The study begins with the use of Antoine equation to estimate the vapor pressures (P_v) of individual gas species as a function of gas temperature (T).

$$ln(P_v) = a - \frac{b}{T - c} \tag{12}$$

The values of a, b, and c are the Antoine parameters, which are shown in Table 3 [88]. It should be noted that the Antoine parameters are valid in temperature ranges near the boiling point of each species. Therefore it is not recommended to use the Antoine parameter values for estimating vapor pressures at temperatures far away from the temperature ranges shown in Table 3. Based on the Antoine equation and parameters, the P_v values of He, H_2, and N_2 are calculated and plotted in Figure 32. Since the temperature of interest in the present study ranges from 50–80 K, the vapor pressures of N_2 can be accurately estimated.

Once the vapor pressures of all gas species are estimated, Raoult's law is used for the estimation of the condensation points (*i.e.*, dew points) of gas mixtures. Raoult's law uses the previously calculated P_v values in the estimation of the condensation

Table 3: Antoine Parameters [88]

Gas Species (T_{min}–T_{max} [K])	He (4–4)	H_2 (14–25)	N_2 (54–90)	F_2 (59–91)	O_2 (63–100)
a	12.25	13.63	14.95	15.67	15.41
b	33.73	164.90	588.72	714.1	734.55
c	1.79	3.19	-6.60	-6.00	-6.45

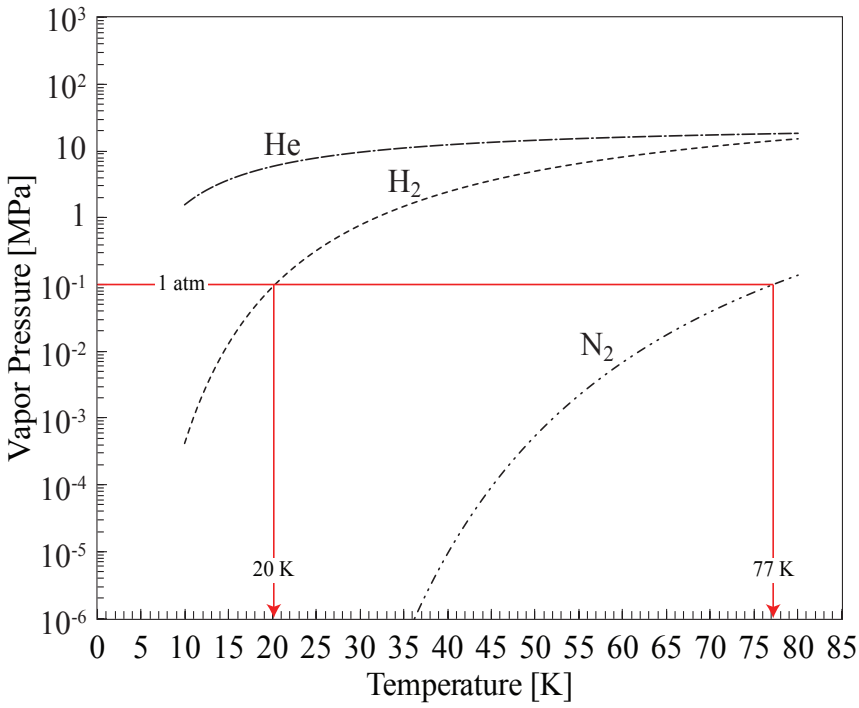

Figure 32: Vapor pressures of individual gas species as a function of temperature.

points of gas mixtures as shown in the following equations.

$$x_A P_{vA} = y_A P, \tag{13}$$

$$x_B P_{vB} = y_B P, \tag{14}$$

where P is the gas pressure, x_A and x_B are the liquid mole fractions of species A and B, y_A and y_B are the gas mole fractions of species A and B, and P_{vA} and P_{vB} are the vapor pressures of species A and B, respectively. By rearranging (13) and (14) in terms of x_A and x_B, respectively, and substituting those into $x_A + x_B = 1$, the dew point of A-B mixture is derived as the following.

$$P = \left(\frac{y_A}{P_{vA}} + \frac{y_B}{P_{vB}} \right)^{-1} \tag{15}$$

For mixtures of multiple (more than two) species, dew points are estimated as

$$P = \Big(\sum_{n=A}^{\infty} \frac{y_n}{P_{vn}} \Big)^{-1}, \tag{16}$$

where P_{vn} is the vapor pressure and y_n is the mole fraction of gas species n. The estimated dew points of He-H_2-N_2 mixtures are presented as an example in Figure 33, in which the x-axis is the mole fraction of N_2 in the gas mixture and the y-axis is the condensation pressure of the gas mixture. Note that the study does not examine mixtures incorporating gaseous Ne because the addition of Ne does not contribute to enhancements in the dielectric properties of the gas mixtures as discussed in Chapter 2. Multiple curves, each representing a gas temperature, are plotted. The estimated values show that at higher temperatures, greater pressure can be applied and larger mole fractions of N_2 can be incorporated to the gas mixture while preventing the condensation of N_2. The operable regions of the gas mixtures at various temperatures are limited to the area below each curve in Figure 33. The x and y-axis values corresponding to the points on each curve serve as boundaries of the operable conditions at each gas temperature. For example, the shaded area in Figure 33 represents the operation region marked by 9.2 mol% N_2 and 1 MPa, which serve as the boundary of the operable condition for the He-H_2-N_2 gas mixture at 77 K.

5.3 Dielectric Strength While Preventing Condensation

An increase in pressure with a constant volume and temperature, a decrease in temperature with a constant volume and pressure, and an increase in the mole fraction of N_2 enhance the dielectric strength of gas mixtures. However, simultaneously increasing the gas pressure and the mole fraction of N_2 while preventing the condensation of N_2 is possible only to a certain extent because of the limitation in the operable region shown in Figure 33. A similar limitation exists with the gas temperature and the

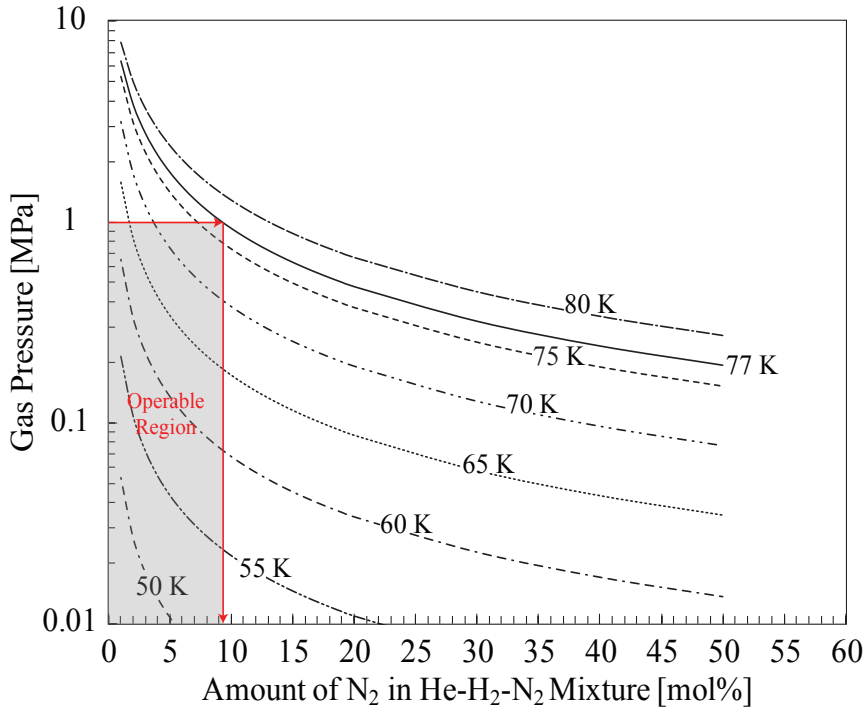

Figure 33: Dew points of He-H_2-N_2 mixtures in various temperatures as a function of the mole fraction of N_2.

mole fraction of N_2. Decreasing the gas temperature and simultaneously increasing the mole fraction of N_2 under a constant volume and pressure condition would lead to the condensation of N_2. Therefore, gas density N and the mole fraction of N_2 involve a trade-off.

In this section, the study maps various potential operating conditions of a cryogenic system, observes variations in the dielectric strength of the He-H_2-N_2 gas mixtures, and discusses the influence of the trade-off between N and the mole fraction of N_2. Table 4 lists the potential cryogenic operating conditions of the He-H_2-N_2 mixtures and the maximum allowed mole fraction of N_2 at pressures ranging from 0.5–2.0 MPa and temperatures ranging from 55–80 K. The table does not include data for 50 K because not even the smallest amount of N_2 is able to remain gaseous at temperatures below 55 K. N values are calculated for all operating conditions under the assumption of an ideal gas condition. $(E/N)_{cr}$ values are obtained by balancing the ionization and attachment collision process in the He-H_2-N_2 mixtures containing

Table 4: Potential Cryogenic Operating Conditions for He-H_2-N_2 Mixtures

Pressure [MPa]	Temperature [K]	[1]Mole Fraction of N_2 [mol%]	[2]N [/m^3]	$(E/N)_{cr}$ [Td]	E_{cr} [V/m]
0.5	55	0.0	6.58×10^{26}	11.0	7.24×10^{6}
0.5	60	1.3	6.03×10^{26}	13.5	8.14×10^{6}
0.5	65	3.3	5.57×10^{26}	18.8	1.05×10^{7}
0.5	70	7.4	5.17×10^{26}	24.6	1.27×10^{7}
0.5	75	14.9	4.82×10^{26}	34.5	1.66×10^{7}
0.5	77	19.0	4.70×10^{26}	38.1	1.79×10^{7}
0.5	80	27.1	4.52×10^{26}	44.4	2.01×10^{7}
1	55	0.0	1.32×10^{27}	11.0	1.45×10^{7}
1	60	0.0	1.21×10^{27}	11.0	1.33×10^{7}
1	65	1.7	1.11×10^{27}	16.3	1.81×10^{7}
1	70	3.8	1.03×10^{27}	19.7	2.03×10^{7}
1	75	7.2	9.65×10^{26}	24.6	2.37×10^{7}
1	77	9.2	9.40×10^{26}	27.4	2.58×10^{7}
1	80	13.1	9.04×10^{26}	32.5	2.94×10^{7}
2	55	0.0	2.63×10^{27}	11.0	2.89×10^{7}
2	60	0.0	2.41×10^{27}	11.0	2.65×10^{7}
2	65	0.0	2.23×10^{27}	11.0	2.45×10^{7}
2	70	1.9	2.07×10^{27}	16.3	3.37×10^{7}
2	75	3.2	1.93×10^{27}	18.8	3.63×10^{7}
2	77	4.2	1.88×10^{27}	19.7	3.70×10^{7}
2	80	6.1	1.81×10^{27}	23.6	4.27×10^{7}

various mole fractions of N_2. Then, $(E/N)_{cr}$ and N values are multiplied to obtain the values of the critical electric field (E_{cr}). Since $(E/N)_{cr}$ values are normalized by N, the study uses E_{cr} values to investigate the absolute dielectric strengths of gas mixtures under various pressure and temperature conditions.

At a constant gas temperature, $(E/N)_{cr}$ decreases as the gas pressure increases as long as the maximum allowed mole fraction of N_2 is a nonzero value. This trend results from the reduction in the maximum allowed mole fraction of N_2 caused by the increase in pressure, which eventually leads to the decrease in $(E/N)_{cr}$. Nevertheless, it should be noted that E_{cr}, which indicates an absolute dielectric strength, increases as the gas pressure increases. This finding is due to the comparatively rapid increase in N overriding the effect of decreasing $(E/N)_{cr}$. For example, when the gas pressure increases from 0.5 MPa to 2.0 MPa at 77 K, N increases four times as much, but $(E/N)_{cr}$ decreases less than one-fourth as much. Therefore, even though $(E/N)_{cr}$ decreases as a result of the decreasing maximum allowed mole fraction of N_2, dielectric

strength E_{cr} increases because of the effect of increasing N.

At a constant gas pressure and volume, one would predict that the dielectric strength of a gas mixture will decrease as the gas temperature increases resulting from the decrease in N. Nevertheless, E_{cr} increases as the gas temperature increases. This finding is due to the relatively rapid increase in the maximum allowed mole fraction of N_2 leading to the rapid increase in $(E/N)_{cr}$, which overrides the effect of the reduction in N. For example, when the gas temperature increases from 55 K to 80 K at 2.0 MPa, N decreases by 31%, but $(E/N)_{cr}$ increases by more than 100%. Therefore, even though N decreases as the gas temperature increases, dielectric strength E_{cr} increases because of the effect of the increase in the maximum allowed mole fraction of N_2.

5.4 Summary

This chapter discussed how to identify and prevent gas mixtures from condensing under cryogenic operating conditions. The process involved using the Antoine equation to calculate the vapor pressures of each gas species and Raoult's law to calculate the condensation points of gas mixtures. In essence, potential condensation in gas mixtures can be prevented by limiting the concentration of constituent gases with low vapor pressures. Due to the limited concentration of individual gas species, the dielectric properties of gas mixtures also changes, which alters the maximum achievable dielectric strength at a cryogenic operating condition.

CHAPTER VI

MAXIMUM ACHIEVABLE DIELECTRIC STRENGTH IN CRYOGENIC POWER SYSTEMS

6.1 Motivation

As an extension of Chapter 2, this chapter focuses on practical aspects in estimating the dielectric strength of gas mixtures in terms of the critical electric field (E_{cr}) over the extended temperature range of 10–100 K at pressures between 1.0 and 2.0 MPa. The study focuses on these temperature and pressure ranges since they cover most of the operating conditions of superconducting power applications. For gas-cooled cryogenic systems, condensation must not occur during operation. To prevent condensation, the study determines the maximum allowed mole fractions of gas species consisting cryogenic gas mixtures by accounting for the operating conditions of cryogenic applications. Subsequently, the study estimates the dielectric strength of the gas mixtures in terms of the density-reduced critical electric field ($(E/N)_{cr}$), obtained by solving the Boltzmann equation with the two-term approximation method. Using the values of $(E/N)_{cr}$, the study calculates the critical electric field (E_{cr}) over the extended cryogenic operation range of 10–100 K at pressures between 1.0 and 2.0 MPa. The results show that the dielectric strength of cryogenic gas mixtures varies as a function of temperature at a constant operating pressure and reaches its minimum at the condensation point of each gas mixture. The results also suggest that $(E/N)_{cr}$ cannot accurately represent the maximum achievable dielectric strength of a gas mixture unless the maximum allowed mole fractions of gas species have been taken into account. Hence, the study discusses $(E/N)_{cr}$ values that are derived from the regulated concentration of gas constituents, which will prevent the components of gas

mixtures from condensing. This study provides recommendations on the suitability of gas mixtures and useful reference data for the dielectric design of superconducting and cryogenic applications.

6.2 Operating Conditions of Cryogenic Power Systems

6.2.1 Temperature Ranges

Typically, a cryogenic power system consists of a superconducting motors and generators, superconducting cables, and cryogenic power converters. Each section has distinct temperature requirements that are determined by factors including background magnetic field, system cooling efficiency, and coefficient of thermal expansion (CTE) mismatch. The temperature requirement determines the type of cryogenic gases that can be used and thus the dielectric strength (*i.e.*, voltage rating) of each section.

For example, superconducting motors and generators operate at the lower end of cryogenic temperatures (20–40 K) to compensate for the reduction of critical current density caused by background magnetic fields [13]. Superconducting cables generally operate in the temperature range of 50–80 K depending on load conditions to take advantage of the higher efficiencies of cryogenic systems at higher operating temperatures [65]. Furthermore, operating power electronic converters at cryogenic temperatures will substantially increase the system-wide efficiency of superconducting power networks. Corresponding research efforts on realizing the cryogenic operation of power electronics technology including the experimental data of Graber *et al.* with insulated-gate bipolar transistors (IGBT) at 77 K have been reported [35].

The optimal operating temperature for cryogenic power-electronic devices has not been determined yet. However, accounting for the fact that the efficiency of cooling decreases at lower temperatures, and that the difference in the coefficient of thermal expansion (CTE) of various materials comprising power electronic converters would

be a bigger challenge at lower temperatures, the study assumes as high as 100 K is a potential temperature range for the cryogenic operation of power electronics devices. For these reasons, the temperature range of 10–100 K is investigated.

6.2.2 Pressure Ranges

In cryogenic power systems, high-pressure gases between 1.0 MPa and 2.0 MPa are used because high-pressure gases are more effective for removing heat from a heat source in the cryogenic power systems. Therefore, we focus on the pressure ranges of 1.0–2.0 MPa. It should be noted that the use of high-pressure gases for cooling is feasible for the development of cryogenic power systems although this approach does not provide the equivalent cooling efficiency as using liquid N_2.

6.3 Gas Mixtures for Cryogenic Operating Conditions

6.3.1 Feasible Gases

6.3.1.1 Electron Scattering Cross Sections

In Chapter 2, the study incorporated gaseous hydrogen (H_2) and N_2 into the cryogenic He gas, which significantly improved the dielectric properties of the gas mixture [68, 70, 71]. In the operating temperature range of 10–100 K, the use of fluorine (F_2) and oxygen (O_2) could also be considered in addition to He, H_2, and N_2. To further enhance the dielectric strength of gas mixtures potentially for those operating at temperatures between 80–100 K, this section investigates the benefit of adding F_2 and O_2, which respectively boils at 85 K and 90 K under atmospheric pressure [88]. As far as boiling points are concerned, gaseous argon (Ar) would also serve as a cryogenic cooling medium. However, it should be noted that this study does not investigate gas mixtures containing Ar because, as reported in our previous work, adding monatomic gases provides no dielectric enhancements. Chapter 2 had shown that adding neon (Ne), a monatomic gas, into gas mixtures results in no practical dielectric improvements [71]. The major difference between monatomic and diatomic

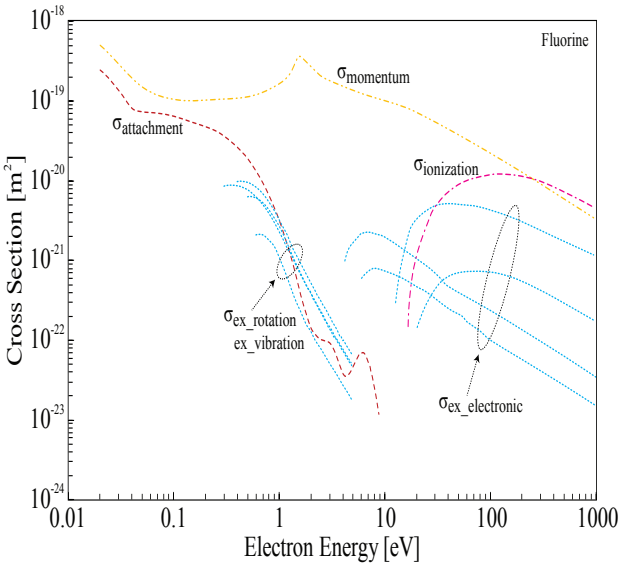

Figure 34: The electron scattering cross sections of F_2. [6]

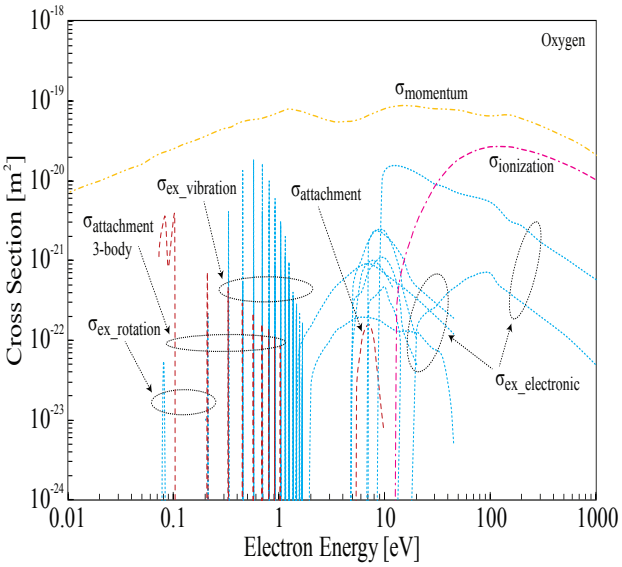

Figure 35: The electron scattering cross sections of O_2. [5]

gases is that diatomic gases (*i.e.*, molecular gases) have numerous vibrational and rotational excitation electron scattering cross sections in addition to the electronic excitation cross sections. The abundance of vibrational and rotational excitation collisions dissipate electron energy substantially and thus lead to dielectric strength enhancements.

According to our previous studies [70, 71], adding gaseous H_2 and N_2 to He contribute to dielectric strength enhancements mainly because of their numerous excitation electron scattering cross sections that substantially dissipate electron energy causing the reduction of mean electron energy and ionization process, leading to dielectric strength improvements. Figures 34 and 35 show that F_2 and O_2 have numerous excitation cross sections including vibrational and rotational excitation cross sections over a wide range of electron energy and electron attachment cross sections, which represent attachment collision processes that involve gas particles absorbing free electrons. In common, both gas species have large momentum-transfer cross sections over the entire energy range and ionization cross sections above 15 eV. However, the electron attachment cross sections of F_2 is several orders of magnitude larger than

that of O_2 and exists over the comparatively wide electron energy range of 0.02–10 eV, which are the indications of a strong electron attaching gas. For O_2, the study also take into account its three-body electron attachment process. As reported by Phelps *et al.*, [15, 51] three-body attachment process becomes more active at low electron energy as gas pressure increases. To account for the influence of gas pressure, the study uses density-normalized cross section data for the three-body attachment process. [5] As an example, Figure 35 shows the three-body attachment cross section of O_2 at 600 Torr (1 Torr = 133.32 Pa), 293 K, which is a measurement condition of Yousfi *et al.*'s data shown in Figure 37. Throughout the study, gas density is used to update the three-body attachment process of O_2. Although reported studies have shown the temperature dependency of cross sections [84], the present study have not accounted for this effect due to the scarcity of data for the entire temperature range of this study. Based on the cross section data of F_2 and O_2 shown in Figures 34 and 35, dielectric strength improvements are expected by the addition of these gases to He. The cross section data were taken from datasets available in the LXcat database [1]. The study use the cross section data from Morgan database [6] for the analysis of F_2 and those from Phelps database [5] for O_2. Note that there is no physical limit in electron energy although the electron scattering cross sections stop at 1,000 eV in the figures.

6.3.1.2 Three-Body Attachment Process

The three-body process, which involves a third neutral or ion particle in the collisions between electrons and neutral gas molecules, becomes increasingly active as gas pressure increases. The study takes into account the three-body electron attachment collision processes of O_2, since the cryogenic operating conditions are generally at high pressure and low temperature. To incorporate the effect of three-body process

in the Boltzmann analysis, the study utilizes the density-normalized three-body electron attachment cross sections of O_2. The study calculates the gas number density for each operating temperature and pressure conditions of a cryogenic power system. Then, the calculated gas density is multiplied with the density-normalized three-body electron attachment cross sections of O_2. This procedure implements the effect of increased three-body processes in high density cryogenic gases.

6.3.1.3 Validity of the Cross Section Data

The validity of our electron scattering cross section data and our calculation accuracy is confirmed by comparing the calculated density-reduced effective ionization coefficient ($(\alpha-\eta)/N$) values of F_2 and O_2 to those published in the literature [39,96,98,99]. The comparisons are presented in Figures 36 and 37. The $(\alpha - \eta)/N$ of F_2 and O_2 show close agreement with values in the literature while showing the highest degree of agreement with the values of Yousfi *et al.* [96] in the case of O_2. Note that we accounted for the three-body attachment process of O_2 to obtain both of the data discussed in Figure 37. The figure shows that the three-body attachment process of O_2 results in comparatively low $(\alpha - \eta)/N$ values at low E/N at a high pressure condition (2.0 MPa, 293 K), but results in comparatively high $(\alpha - \eta)/N$ values at low E/N at a low pressure condition (600 Torr, 293 K), which agree well with the literature data. The reduction in $(\alpha - \eta)/N$ values at the high pressure condition is mainly due to increased three-body electron attachment processes that increases η/N at low E/N. The agreement between the calculation results of this study and the values of the literature confirms that the calculation method and the electron scattering cross section data of F_2 and O_2 are suitable for the study.

6.3.2 Electron Kinetics of Feasible Gas Mixtures

By solving the Boltzmann equation with the two-term approximation, the study predicted an increase in dielectric strength as the mole fraction of H_2 is increased in the

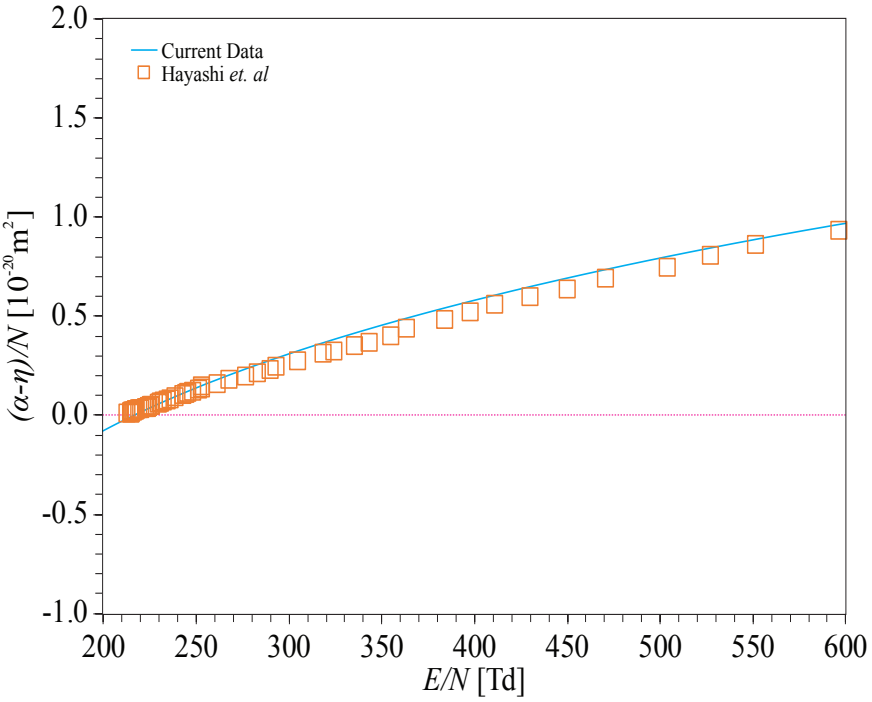

Figure 36: The effective ionization coefficient of F_2 from the current study and the literature. (Hayashi *et al.*, [39])

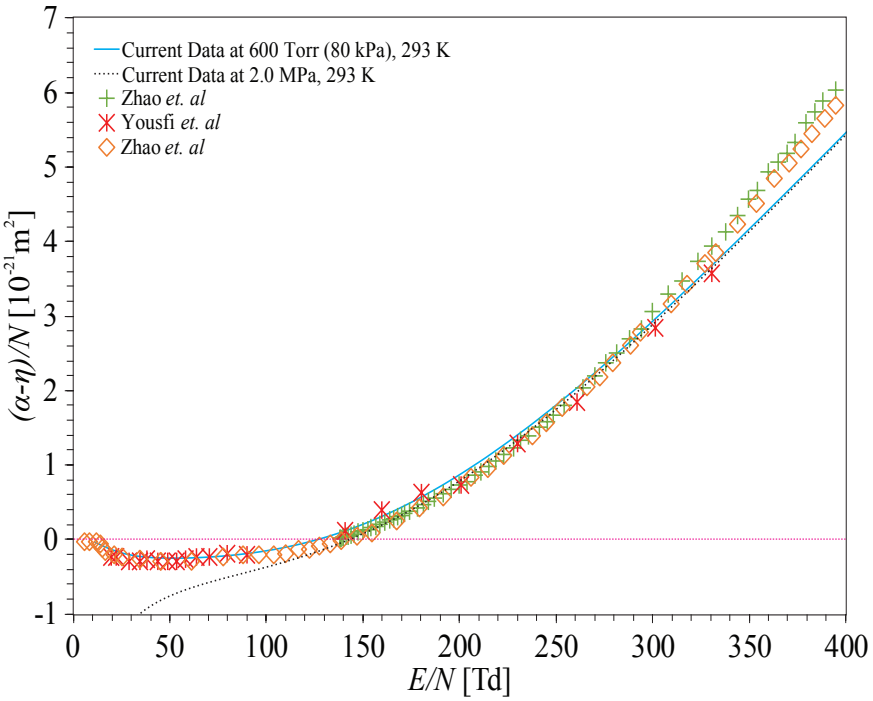

Figure 37: The effective ionization coefficient of O_2 from the current study and the literature. (Zhao *et al.*, [98] Yousfi *et al.*, [96] Zhao *et al.*, [99])

He-H_2 mixture and experimentally validated the prediction in our publications [18,70]. Based on the same method of analysis, this study also predicted that increasing the mole fraction of N_2 will further enhance the dielectric properties of cryogenic He-H_2-N_2 mixture [71]. This section discusses the variation in dielectric properties caused by introducing F_2 and O_2 into gas mixtures based on the coefficients of electron kinetic processes. The study compares the α/N, η/N, and $(\alpha-\eta)/N$ values of He-N_2, He-F_2, He-O_2, He-H_2-N_2, He-H_2-F_2, and He-H_2-O_2 mixtures, which are the representative gas mixtures of this study. For simplicity, all binary gas mixtures consist of 90 mol% He mixed with the 10 mol% of N_2, F_2, or O_2. Similarly, all ternary gas mixtures consist of 83 mol% He and 7 mol% H_2 mixed with the 10 mol% of N_2, F_2, or O_2. Note that H_2 was fixed to 7 mol% because it is the maximum allowed amount of H_2 that can be used without flammability issues [70]. Also, note that the three-body attachment cross sections of O_2 that apply to the low-pressure condition of Figure 37 are used for the calculations in this section.

6.3.2.1 Density-Reduced Ionization Coefficient

Figure 39 presents the α/N values of the gas mixtures as functions of E/N. The results show that He-F_2 has the highest α/N indicating the most active ionization collision process whereas He-H_2-N_2 has the lowest α/N indicating the least active ionization collision process.

In general, α/N values decrease from high to low values in gas mixtures containing F_2, O_2, and N_2. The trend is mainly due to the difference in the variety of excitation cross sections among the three gas species. Among the three, F_2 has the least, and N_2 has the most diverse excitation cross sections including numerous vibrational and rotational excitation cross sections. Excitation collisions substantially dissipate the electron energy of gas mixtures that lead to a reduction in mean electron energy (Figure 38) and lower ionization collision process. Note that the mean electron energy

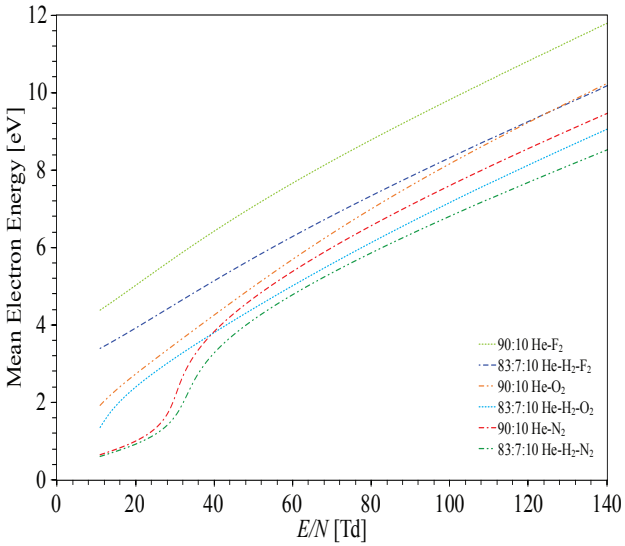

Figure 38: The mean electron energy of He-N_2, He-F_2, He-O_2, He-H_2-N_2, He-H_2-F_2, and He-H_2-O_2.

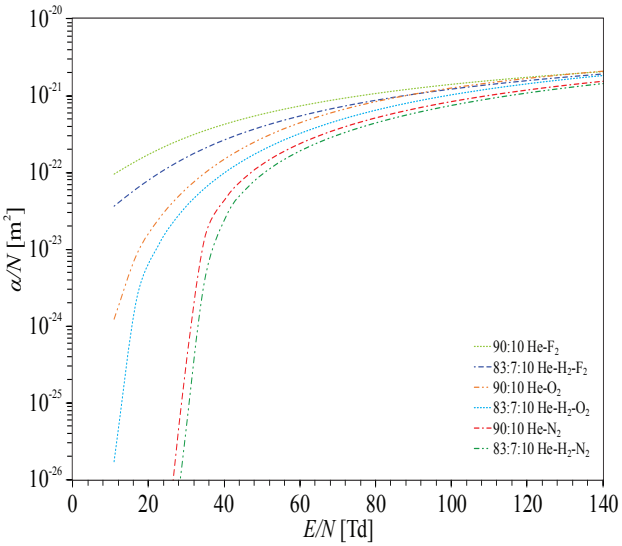

Figure 39: The density-reduced ionization coefficient of He-N_2, He-F_2, He-O_2, He-H_2-N_2, He-H_2-F_2, and He-H_2-O_2.

also shows a decreasing trend in its values in gas mixtures containing F_2, O_2, and N_2. Furthermore, the ternary gas mixtures containing 7 mol% H_2 have lower α/N than their binary counterparts (e.g., the He-H_2-N_2 mixture has a lower α/N than the He-N_2 mixture). The difference in α/N of the binary and ternary gas mixtures indicates that increasing the mole fractions of the diatomic gases reduces the mean electron energy (Figure 38) and the ionization process of gas mixtures (Figure 39).

6.3.2.2 Density-Reduced Attachment Coefficient

Figure 40 presents the η/N values of the gas mixtures as functions of E/N. The results show that He-H_2-F_2 has the highest η/N indicating the most active attachment process whereas He-H_2-N_2 has the lowest η/N indicating the least active attachment process.

In general, η/N values descend from high to low in gas mixtures containing F_2, O_2, and N_2. The descending trend is mainly due to difference in the electron attachment cross sections of the gas species. Among the three gas species, F_2 not only has the largest, but also the widest electron attachment cross sections that exist over

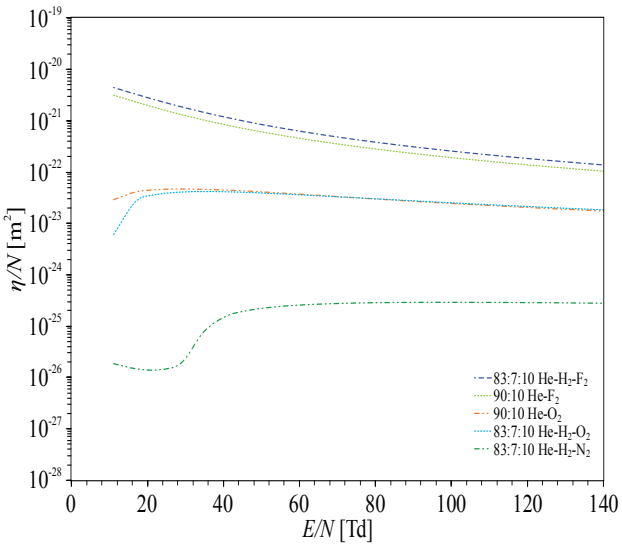

Figure 40: The density-reduced attachment coefficient of He-N_2, He-F_2, He-O_2, He-H_2-N_2, He-H_2-F_2, and He-H_2-O_2.

0.02–10 eV. In contrast, the electron attachment cross sections of O_2 are orders of magnitude smaller and narrower than that of F_2. Note that N_2 does not have electron attachment cross sections.

The decreasing η/N values of He-H_2-F_2 and He-F_2 mixtures at high E/N mainly result from the increasing mean electron energy of gas mixtures at high E/N (Figure 38). Higher mean electron energy reduces the attachment process since the electron attachment cross sections of F_2 decrease at higher electron energy. In addition, the η/N of He-H_2-O_2 and He-O_2 mixtures and that of He-H_2-N_2 mixture increase around 18 Td and 35 Td. The increase in η/N occurs as the electron energy distribution shifts to higher energy as E/N increases such that more electrons would have enough energy to interact with collision processes corresponding to the electron attachment cross sections of O_2 (5.3–11.4 eV) and H_2 (3.5–18 eV).

6.3.2.3 Density-Reduced Effective Ionization Coefficient and Density-Reduced Critical Electric Field

From the results of α/N and η/N, the study calculates $(\alpha - \eta)/N$, which represents the net ionization processes of gas mixtures. According to Figure 41, He-H_2-F_2 and

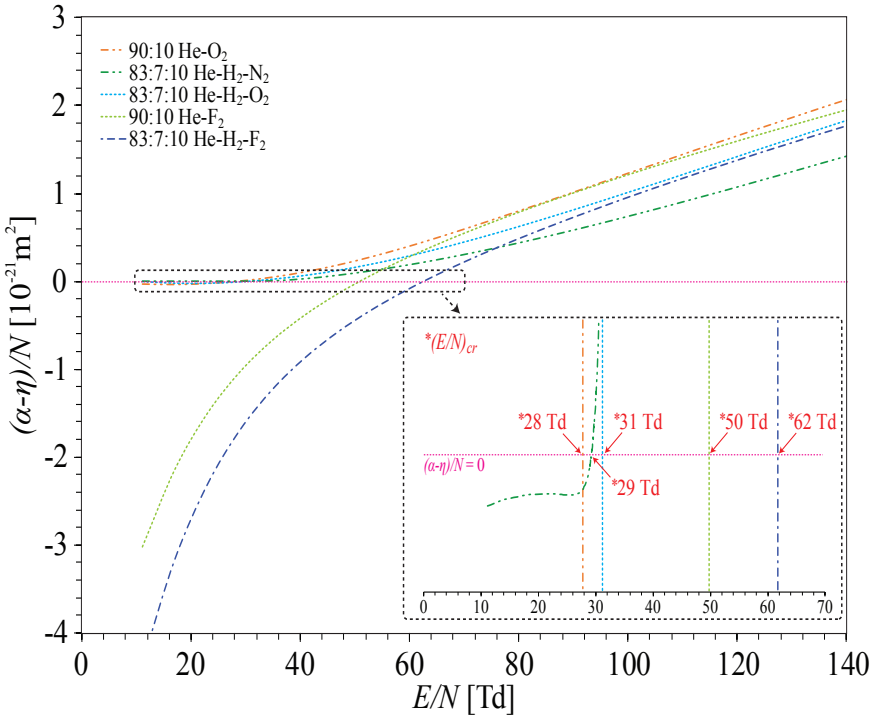

Figure 41: The density-reduced effective ionization coefficient of He-N_2, He-F_2, He-O_2, He-H_2-N_2, He-H_2-F_2, and He-H_2-O_2. (Note that the dashed box is a close-up view of the zero-crossing points.)

He-F_2 mixtures show rapidly decreasing $(\alpha - \eta)/N$ at low E/N. This trend is likely due to the increasing η/N of He-H_2-F_2 and He-F_2 mixtures at low E/N caused by increasing electron attachment process. In contrast, the $(\alpha - \eta)/N$ values of the gas mixtures without F_2 (*i.e.*, He-H_2-N_2, He-N_2, He-H_2-O_2, and He-O_2 mixtures) show a comparatively small decreasing trend at low E/N because the η/N values of the gas mixtures without F_2 are several orders of magnitude smaller than those of the gas mixtures with F_2.

E/N values corresponding to the zero crossing points of $(\alpha - \eta)/N$ are $(E/N)_{cr}$, which are shown in the closer view of Figure 41. According to the figure, the He-O_2 mixture has the lowest $(E/N)_{cr}$ value of 28 Td while the He-H_2-N_2 and He-H_2-O_2 mixtures have $(E/N)_{cr}$ at 29 Td and 31 Td, respectively. Furthermore, gas mixtures containing F_2 show much higher $(E/N)_{cr}$ values because of the strong electron attaching properties of F_2: the He-F_2 and He-H_2-F_2 mixtures have $(E/N)_{cr}$ at 50 Td

and 62 Td, respectively.

6.3.2.4 Predicted Dielectric Improvements

Numerous studies have used $(E/N)_{cr}$ as means to assess the dielectric strength of gas mixtures because $(E/N)_{cr}$ indicates a transition from the attachment-process-dominant state to the ionization-process-dominant state of electron kinetic process (*i.e.*, $\alpha - \eta = 0$) [43, 57, 60]. Using the same method, the present study refers to the $(E/N)_{cr}$ values shown in Figure 41 to compare the dielectric strength of gas mixtures. Among the gas mixtures shown in Figure 41, the He-O_2 mixture has the lowest dielectric strength and the He-H_2-F_2 mixture has the highest dielectric strength. Among the ternary gas mixtures, the He-H_2-N_2 mixture shows a lower dielectric strength than both He-H_2-O_2 and He-H_2-F_2 mixtures.

A direct comparison of $(E/N)_{cr}$ may be suitable for estimating the dielectric strength of gas mixtures in applications, in which the condensation of a component gas will not occur [85]. However, as the condensation of a component gas is a potential issue in gas-insulated high voltage applications, it is also a potential issue for gas-cooled cryogenic systems. Hence, we will explain in the following sections that the $(E/N)_{cr}$ of gas mixtures cannot accurately represent the achievable dielectric strengths at cryogenic operating conditions unless the condensation of one or more gas constituents in a gas mixture has been taken into account.

6.4 Maximum Achievable Dielectric Strength of Cryogenic Gas Mixtures

6.4.1 Preventing Condensation in Gas Mixtures

The previous section showed that He-H_2-F_2 has the highest $(E/N)_{cr}$ among the studied gas mixtures, which indicates that He-H_2-F_2 should provide the highest dielectric strength. However, it is not always possible to use the gas mixture with the highest

dielectric strength for all cryogenic operating conditions because of the potential condensation of gas mixtures, which must be prevented in gas-cooled cryogenic systems. Again, as much as the dielectric strength is important, preventing the condensation of gas mixtures is also important in operating gas-cooled cryogenic systems. To avoid conditions that cause the condensation of gas mixture constituents during operation, limiting the concentration of individual gas species comprising gas mixtures is necessary. As discussed in Chapter 3, the study initially solves the chemical phase equilibrium (*i.e.*, Antoine equation and Antoine parameters are presented in Table 3) to estimate the vapor pressure of He, H_2, N_2, F_2, and O_2. Then, the study uses the calculated vapor pressure and Raoult's law to calculate the condensation conditions of gas mixtures for the operating temperature and pressure ranges of an actual cryogenic power system, through which the maximum allowed mole fractions of individual gas species that will not cause any condensation are identified.

Based on the procedure, the condensation curves (*i.e.*, dew points) of He-H_2, He-H_2-N_2 He-H_2-F_2, and He-H_2-O_2 mixtures are calculated for 10–100 K to estimate the maximum allowed mole fractions of constituent gas species at 1.0, 1.5, and 2.0 MPa.

6.4.2 Density-Reduced Critical Electric Field of Gas Mixtures Over the Extended Range of Cryogenic Operating Conditions

The $(E/N)_{cr}$ values of various gas mixtures were compared in Figure 41, which shows that the 83:7:10 He-H_2-N_2 mixture has a lower $(E/N)_{cr}$ than that of the 83:7:10 He-H_2-F_2 mixture. However, not all of these gas mixtures may be suitable for a comparison under cryogenic operating conditions because gas composition will be changed to prevent condensation under such conditions. That is, the $(E/N)_{cr}$ values of gas mixtures should take into account the adjusted gas composition for avoiding condensation under cryogenic conditions and the increased three-body attachment process of O_2 at high pressures to represent the actual achievable dielectric strength of a system. Hence, the study calculates the maximum allowed mole fractions of

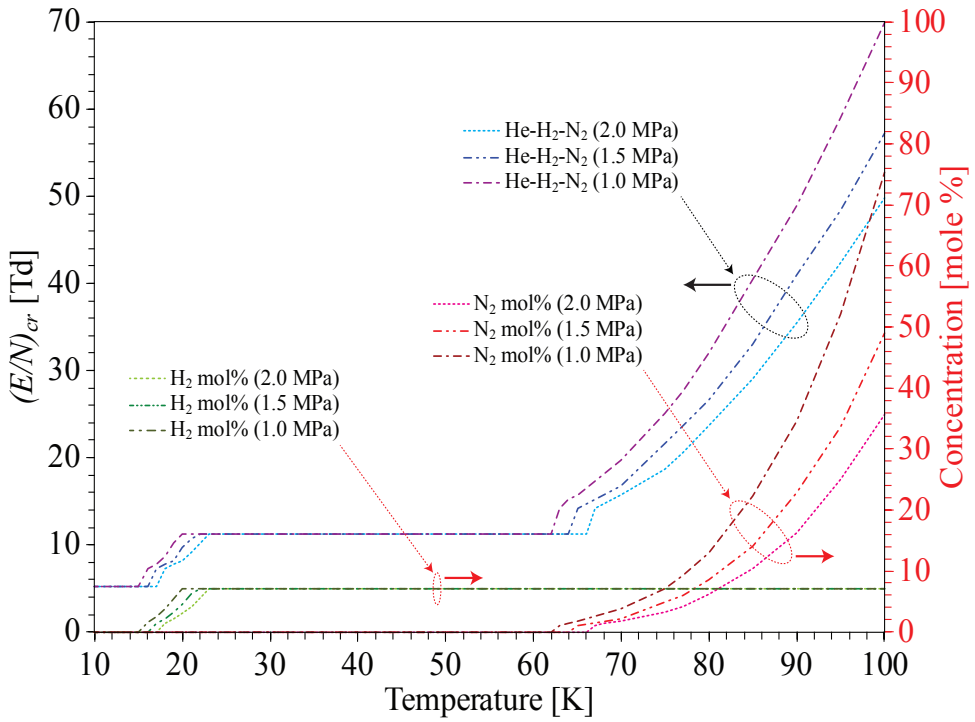

Figure 42: The density-reduced critical electric field of He-H_2-N_2 mixture and the concentration of component gas species at 1.0–2.0 MPa in the temperature range of 10–100 K.

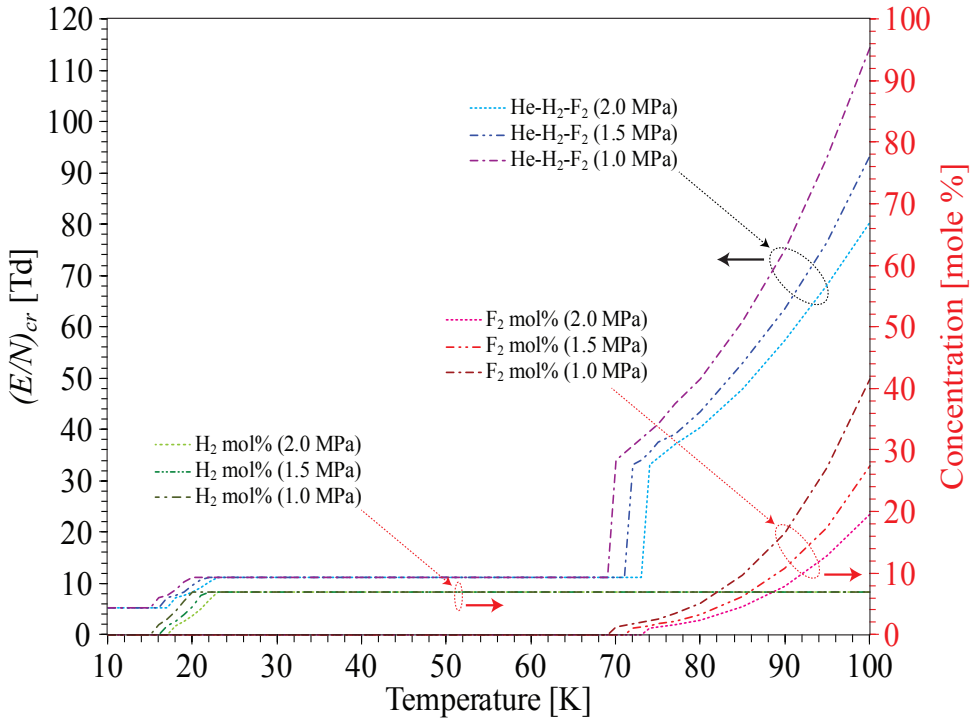

Figure 43: The density-reduced critical electric field of He-H_2-F_2 mixture and the concentration of component gas species at 1.0–2.0 MPa in the temperature range of 10–100 K.

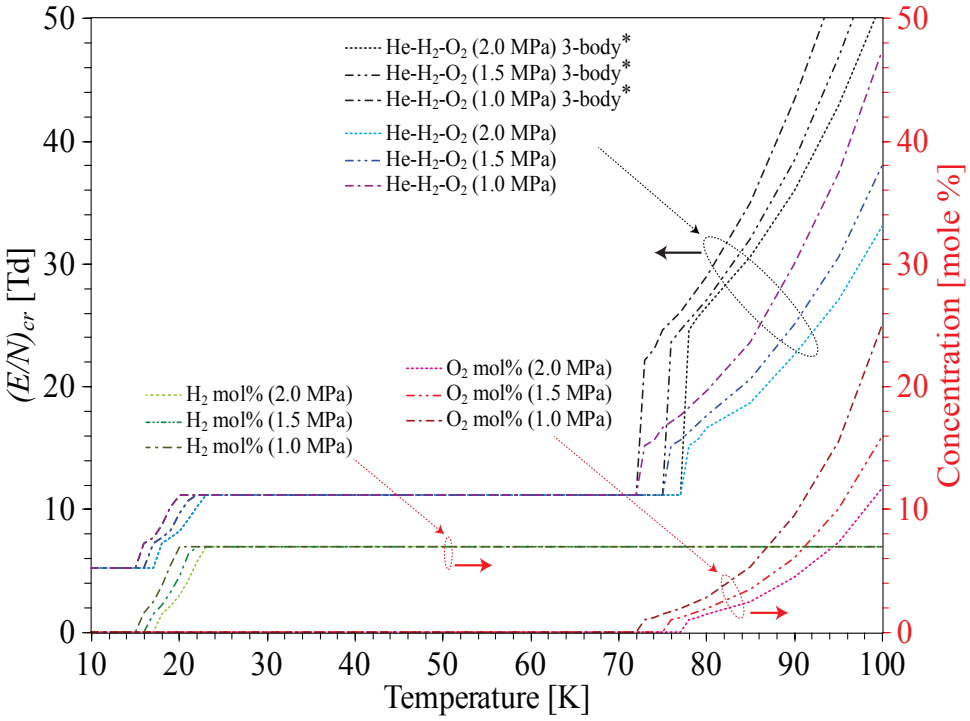

Figure 44: The density-reduced critical electric field of He-H_2-O_2 mixture and the concentration of component gas species at 1.0–2.0 MPa in the temperature range of 10–100 K. $^*(E/N)_{cr}$ that accounts for the three-body attachment process of O_2. The three-body attachment cross sections of O_2 are updated at each operating condition.

gas species that are suitable for each cryogenic operating condition and use the three-body attachment cross section of O_2 corresponding to the respective gas densities to derive $(E/N)_{cr}$ values over the extended range of cryogenic operating conditions.

Figures 42–44 map the $(E/N)_{cr}$ values of various gas mixtures that could be used to achieve the maximum dielectric strength while preventing condensation over the wide range of cryogenic operating conditions. These figures also show the varying mole fraction of individual gas species in He-H_2, He-H_2-N_2, He-H_2-F_2, and He-H_2-O_2 mixtures as a function of gas temperature. The three figures show that H_2 could be mixed with He at comparatively low gas temperatures while N_2, F_2, and O_2 could be mixed at higher temperatures. Difference in the amount of gas species that could be used at different temperatures results in $(E/N)_{cr}$ values that vary as a function of gas temperature. The dashed lines on the upper part of Figures 42–44 (*i.e.*, purple, dark

blue, light blue, and black, which shows the effect of three-body attachment processes in mixtures containing O_2) represent the $(E/N)_{cr}$ values of gas mixtures while the rest plotted on the lower part of each figures represent the maximum allowed mole fractions of individual gas species that could be added into the gas mixtures. In all three figures, it is possible to commonly observe a stepwise increase in $(E/N)_{cr}$ as gas temperature increases. The stepwise increase in $(E/N)_{cr}$ occurs when gas temperature reaches a point where an additional gas species can be added into the gas mixture. H_2, for example, can be added at 15, 16, and 17 K for 1.0, 1.5, and 2.0 MPa, respectively. The addition of H_2 leads to the stepwise increase in $(E/N)_{cr}$, which are observed at the corresponding temperatures (*i.e.*, 15, 16, and 17 K). If there were no flammability concerns regarding the use of H_2, $(E/N)_{cr}$ and the mole fraction of H_2 would have increased gradually while condensation is prevented as gas temperature increases. However, to prevent potential fire hazards, the mole fraction of H_2 is limited to 7 mol% and thus $(E/N)_{cr}$ values plateau once the 7 mol% is reached. The region of plateau in Figures 42–44 represents the 93:7 He-H_2 mixture. The plateau continues until gas temperature increases to a high value that enables the use of another gas species that has even a lower vapor pressure. The second stepwise increases of $(E/N)_{cr}$ in Figures 42–44 are caused by the addition of N_2, F_2, and O_2, respectively. In the case of He-H_2-N_2 mixture, N_2 concentration begins to increases at 62, 64, and 66 K for 1.0, 1.5, and 2.0 MPa, respectively. Similarly, in the case of He-H_2-F_2 mixture, F_2 concentration begins to increase at 69, 71, and 73 K for 1.0, 1.5, and 2.0 MPa, respectively. Finally, in the case of He-H_2-O_2 mixture, O_2 concentration begins to increase at 72, 75, and 77 K for 1.0, 1.5, and 2.0 MPa, respectively. Due to the pressure dependence of three-body attachment process in O_2, the largest step-wise increase in $(E/N)_{cr}$ is observed in He-H_2-O_2 (2.0 MPa) 3-body* at 77 K while the lowest step-wise increase is observed in He-H_2-O_2 (1.0 MPa) 3-body* at 72 K. Note that Figure 44 also presents $(E/N)_{cr}$ values that do not account for the

three-body attachment process of O_2. The two cases (*i.e.*, with and without three-body attachment process) show similar trends, but show significant differences in the $(E/N)_{cr}$ values, which indicates that the three-body attachment process should be taken into account for achieving accurate dielectric strength estimations in gas mixtures incorporating O_2.

6.4.3 Critical Electric Field of Gas Mixtures Over the Extended Range of Cryogenic Operating Conditions

For the actual dielectric design of cryogenic systems, $(E/N)_{cr}$ may not be the most practical value to use since it is normalized by gas density N. Therefore, this section calculates gas density N assuming the ideal gas condition (*i.e.*, $N = P/(kT)$, where P is pressure, k is the Boltzmann constant, and T is temperature) and use $(E/N)_{cr}$ and N to derive E_{cr}, which provides the most practical information regarding the dielectric strength of gas mixtures.

According to the ideal gas law, at a constant gas pressure, N decreases as gas temperature increases. Reduction in N results in an increased electron mean free path that increases the mean electron energy, which also corresponds to high E/N. Increased mean electron energy generally leads to higher ionization process and lower attachment process, which decreases the dielectric strength of gas mixtures. However, it should be noted that the positive correlation between N and the dielectric strength of gas mixtures only holds for conditions that apply to the right hand side of the Paschen's minimum. If the conditions apply to the left hand side of the Paschen's minimum, the dielectric strength of gas mixtures would increase when N is decreased. Under this condition, the electron mean free path is greater than the distance between electrodes that the ionization collisions cannot frequently occur because of the lack of interacting gas particles. Since the cryogenic operating conditions of this study involve high density gases, it is assumed that N is always positively correlated to the dielectric strength, which applies to the right hand side of the Paschen's minimum.

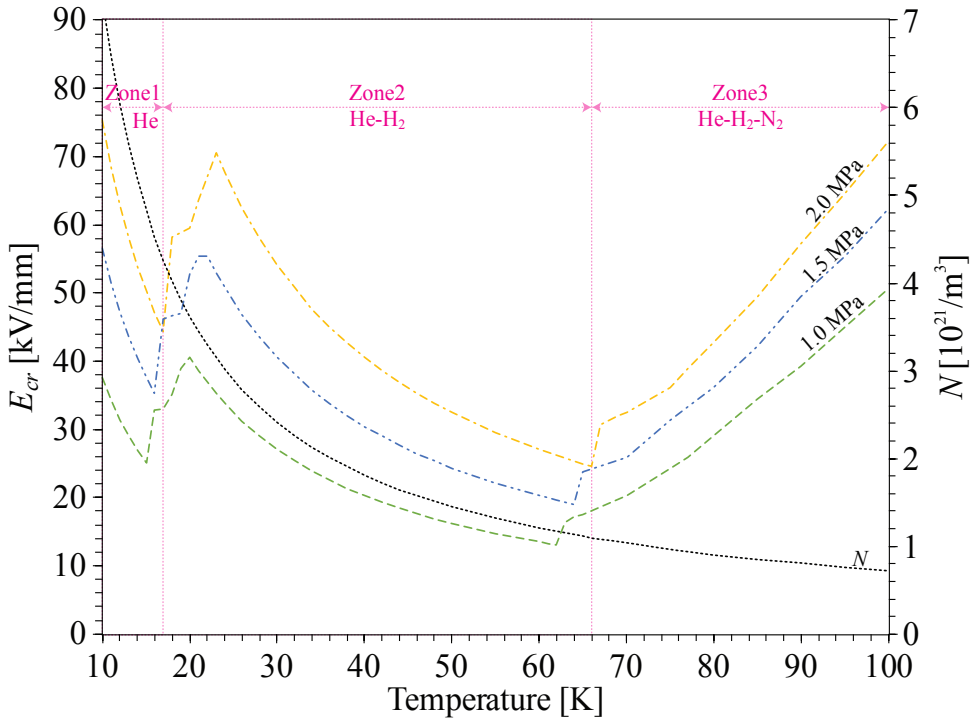

Figure 45: The critical electric field of He-H_2-N_2 mixture and the gas particle density at 1.0–2.0 MPa in the temperature range of 10–100 K.

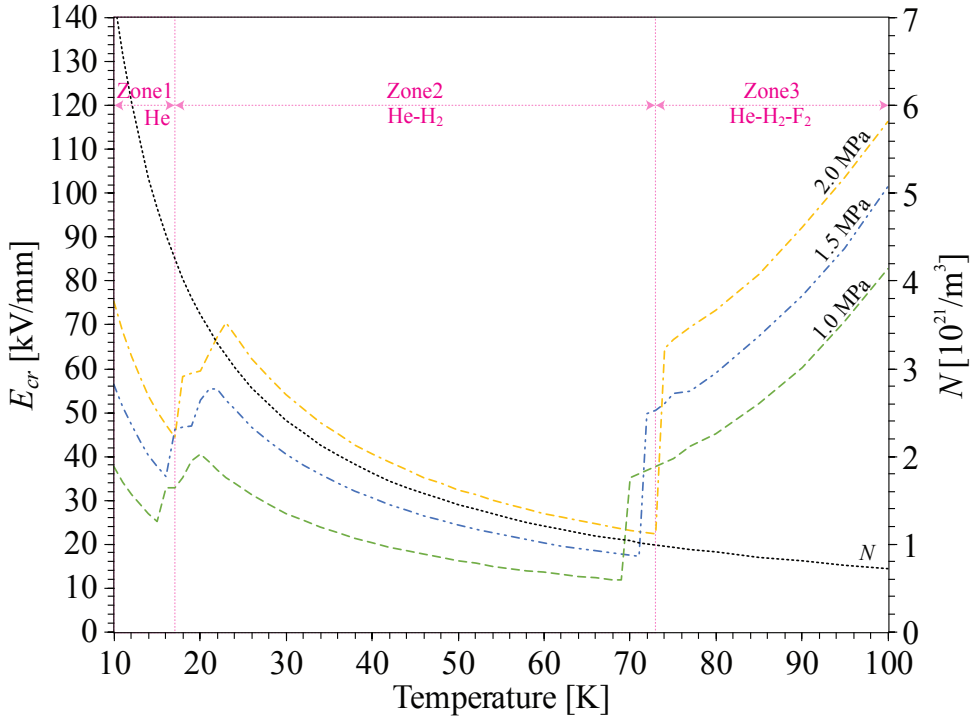

Figure 46: The critical electric field of He-H_2-F_2 mixture and the gas particle density at 1.0–2.0 MPa in the temperature range of 10–100 K.

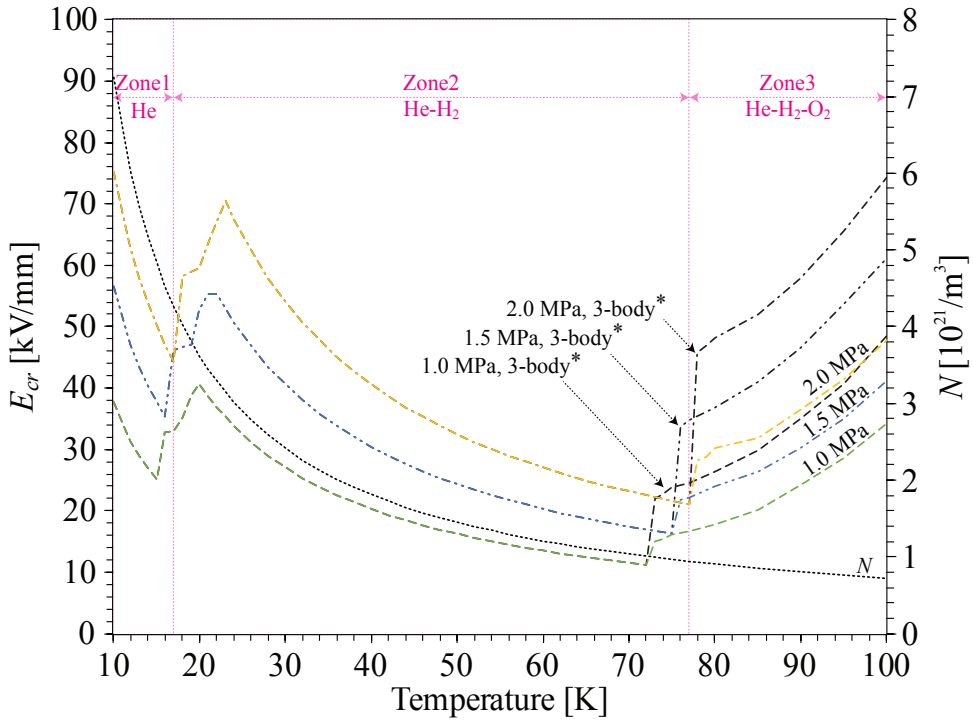

Figure 47: The critical electric field of He-H_2-O_2 mixture and the gas particle density at 1.0–2.0 MPa in the temperature range of 10–100 K. $^*E_{cr}$ that accounts for the three-body attachment process of O_2.

Accordingly, Figures 45-47 show the decreasing trend of N as a gas temperature increases, which are plotted in black dotted lines. As a result, E_{cr}, which is obtained by multiplying $(E/N)_{cr}$ by N, decreases as gas temperature is increased except at temperature ranges, in which $(E/N)_{cr}$ increases due to the addition of new gas species. Colored dashed lines in Figures 45-47 represent the E_{cr} of He-H_2-N_2, He-H_2-F_2, and He-H_2-O_2 mixtures, respectively. All three gas mixtures commonly show a decreasing trend in E_{cr} as gas temperature increases, which corresponds to the decreasing trend of N except when new gases are added into the gas mixture. Due to the several decrease and subsequent increase in E_{cr}, dielectric strength minimums are observed in Figures 45-47.

E_{cr} curves can be divided into three zones. *Zone* 1 consists of pure He, and E_{cr} decreases as gas temperature increases because N decreases while $(E/N)_{cr}$ is constant. *Zone* 1 is in the lowest temperature range, so no other gas species other

than He can exist in gas phase. For all three figures, *Zone* 2 begins with increasing E_{cr} at 15, 16, and 17 K, which are caused by the addition of H_2 at 1.0, 1.5, and 2.0 MPa, respectively. Even in *Zone* 2, N gradually decreases as gas temperature increases. Nevertheless, because the rate of increase in $(E/N)_{cr}$ caused by adding H_2 outweighs that of decreasing N, E_{cr} increases as long as the mole fraction of H_2 is increased. However, as discussed earlier, the mole fraction of H_2 is limited to 7 mol% to prevent flammability issues and thus E_{cr} stops increasing and decreases again at 20, 22, and 23 K. E_{cr} decreases as gas temperature increases until it reaches *Zone* 3, in which another gas can be incorporated into the gas mixture. The beginning of *Zone* 3 in a gas mixture vary depending on the species of the additional gas. N_2 has the highest vapor pressure while O_2 has the lowest one. Hence, the *Zone* 3 of the He-H_2-N_2 mixture begins at the lowest temperature among the three gas mixtures. *Zone* 3 of the He-H_2-O_2 mixture (Figure 47) consists of two sets of E_{cr} values: one with the three-body attachment process (marked as 3-body*) and the other without. The magnitude of E_{cr} is clearly lower in the curves that do not account for the three-body attachment process of O_2. The difference again shows the significance of the three-body process in O_2 at high pressure conditions. Note that E_{cr} gradually increases throughout the entire temperature range of *Zone* 3, which is due to the rapid increase of $(E/N)_{cr}$ outweighing the decreasing N.

6.4.4 Discussion

6.4.4.1 Gas Mixture Comparison

Figure 48 compares the dielectric strength of He-H_2-N_2, He-H_2-F_2, and He-H_2-O_2 mixtures operating at 2.0 MPa. *Zone* 1 and *Zone* 2 are identical for all three gas mixtures since *Zone* 1 contains pure gaseous He and *Zone* 2 contains He-H_2 gas mixtures. *Zone* 3, however, contains distinct gas mixtures. N_2, which has a higher vapor pressure than F_2 and O_2 can be added into the gas mixture at 66 K. Then, F_2 and O_2 can be added at 73 K and 77 K, respectively. Therefore, at 2.0 MPa, we

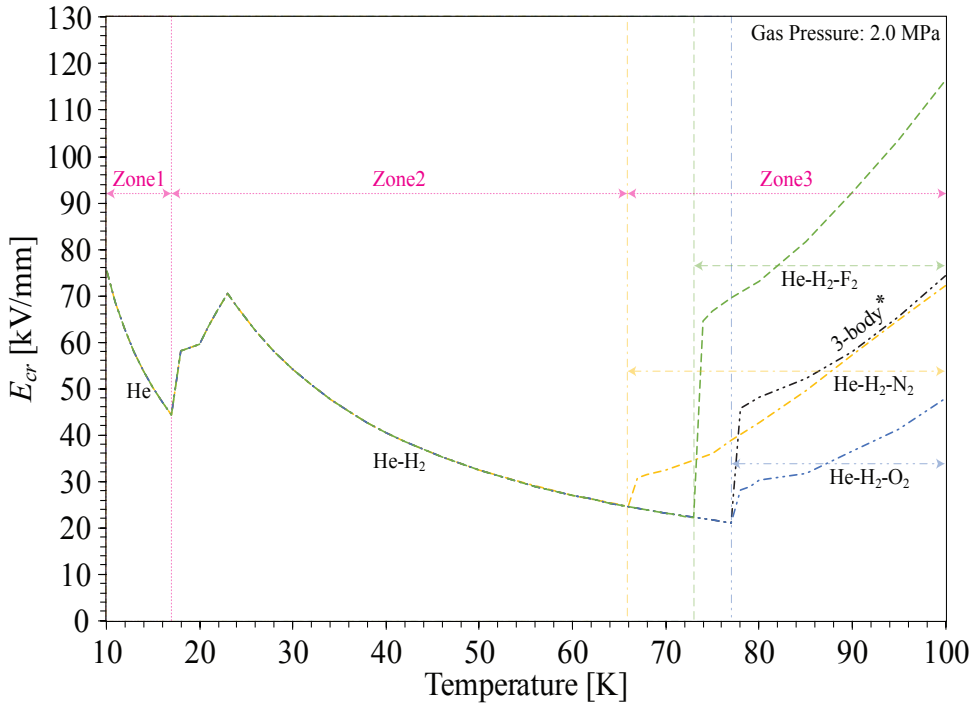

Figure 48: The critical electric field of He-H_2-N_2, He-H_2-F_2, and He-H_2-O_2 mixture at 2.0 MPa in the temperature range of 10–100 K. $^*E_{cr}$ that accounts for the three-body attachment process of O_2. (Note that the results at 1.0 and 1.5 MPa are not presented because they show similar trends to that of 2.0 MPa.)

recommend using the He-H_2-N_2 mixture between 66–73 K to maximize the dielectric strength. At temperature above 73 K, however, the He-H_2-F_2 mixture should be used since it has a substantially stronger dielectric strength than the other two gas mixtures. Even for the He-H_2-O_2 mixture, which involves three-body attachment processes, the dielectric strength is lower than that of the He-H_2-F_2 mixture. Note that similar trends are expected at the gas pressures of 1.5 and 1.0 MPa.

An interesting finding is that the achieved dielectric strength of He-H_2-N_2 is higher than that of He-H_2-F_2 and He-H_2-O_2 at 66–73 K as shown in Figure 48 even though Figure 41 have shown that the $(E/N)_{cr}$ of He-H_2-N_2 is lower than that of He-H_2-F_2 and He-H_2-O_2, which indicated that He-H_2-F_2 and He-H_2-O_2 are better dielectric media from the electron kinetics perspective. The actual achievable dielectric strength of He-H_2-N_2 is higher at 66–73 K mainly because N_2 has a higher vapor pressure than

F_2 and O_2, so higher mole fractions of N_2 can be added into the gas mixture at a lower gas temperature.

6.4.4.2 Minimum Dielectric Strength

For all three gas mixtures presented in Figures 45-47, the dielectric strength of gas mixtures decreases as gas temperature increases to the point, at which a new gas can be added. As the new gas is introduced into the gas mixture, $(E/N)_{cr}$ rapidly increases than the decreasing rate of N resulting in the increase of dielectric strength. The subsequent increase in dielectric strength following the decreased dielectric strength creates a dielectric strength minimum. In Figure 45, the dielectric strength minimum of He-H_2-N_2 mixture occurs at 62 K (1.0 MPa), 64 K (1.5 MPa), and 66 K (2.0 MPa). Similarly, Figure 46 shows the dielectric strength minimum of He-H_2-F_2 mixture occurring at 69 K (1.0 MPa), 71 K (1.5 MPa), and 73 K (2.0 MPa). Likewise, Figure 47 shows the dielectric strength minimum of He-H_2-O_2 mixture occurring at 72 K (1.0 MPa), 75 K (1.5 MPa), and 77 K (2.0 MPa). Hence, in the case of He-H_2-N_2 gas mixture, operating a cryogenic system at 62 K (1.0 MPa), 64 K (1.5 MPa), and 66 K (2.0 MPa) should be avoided if maximizing the dielectric strength is the key factor in its design. To achieve higher dielectric strength, designers could either increase or decrease the operating temperature. It should be noted that from the cooling efficiently perspective, maintaining gas temperature at higher temperatures requires less effort and energy loss. Hence, operating cryogenic systems at relatively higher temperatures to reduce the cooling effort and to increase the voltage level achieved by enhanced dielectric strength might be a good decision for non-superconducting devices that require cryogenic operation such as cryogenic power electronics applications. However, increasing the operating temperature could be an issue for superconducting applications because increased temperature reduces current density in superconductors (current density doubles per 10 K temperature

drop). Nevertheless, increasing the voltage rating of a cryogenic system by increasing its operating temperature could enable the same amount of electric power even though the current density is reduced: but this option would additionally require the entire system to be designed for higher voltage levels.

6.5 Special Note

We recognize the potential toxicity and possible chemical reactions between the constituent gases in the mixtures consisting of H_2, F_2, and O_2. In the absence of detailed knowledge on the products of chemical reactions, the kinetics of reactions, and the recombination of the products at cryogenic temperatures, the present study does not include the effect of chemical reactions on the dielectric behavior of the mixtures. Instead, the study focused on mapping the practical temperature and pressure ranges of the mixtures, in which they stay in gas phase without any condensation to ensure that initial gas compositions are maintained.

6.6 Summary

This chapter extended the work on the dielectric strength estimation of cryogenic gas mixtures by introducing F_2 and O_2. By using the electron scattering cross section data, the study analyzed variations in the electron kinetic processes of gas mixtures containing F_2 and O_2 in detail by solving the Boltzmann equation with the two-term approximation. Since preventing condensation is crucial in operating gas-cooled cryogenic systems, the study estimated the vapor pressure of each gas species and calculated the condensation conditions of various gas mixtures. Based on the condensation data, the study estimated the maximum allowed mole fraction of gases including F_2 and O_2, which will not condense in cryogenic conditions, and mapped $(E/N)_{cr}$. Then, assuming the ideal gas condition, the study calculated E_{cr} values over the extended range of cryogenic operating conditions (*i.e.*, 10–100 K at 1.0–2.0 MPa). The results have revealed that the dielectric strength of gas mixtures decreases at higher

temperatures due to decreasing gas density N, but increases when gas temperatures reach values, in which additional gases can be added into the gas mixtures. That is, $(E/N)_{cr}$ increases faster than the decreasing rate of N and thus E_{cr} increases. In addition, dielectric strength minimums were observed by the combined effect of temperature increase that decreased gas density N and the increased maximum allowed mole fractions of additional gas species at higher temperatures that rapidly increased $(E/N)_{cr}$. The study identified the cryogenic operating conditions of dielectric strength minimums and suggested to avoid operating under such conditions to prevent dielectric failures in cryogenic power systems.

This study provides useful reference data for identifying the achievable maximum dielectric strength of He-based binary and ternary gas mixtures under the extended cryogenic operating conditions while gas mixture condensation is prevented. The results show operating conditions corresponding to the dielectric minimums, which should be avoided for the development and design of gas-cooled cryogenic applications that require high voltage rating.

CHAPTER VII

IMPROVED DIELECTRIC STRENGTH MODEL FOR CRYOGENIC GAS MIXTURES

7.1 Motivation

The dielectric strength of cryogenic gas mixtures is one of major design constraints that determine the voltage ratings of high temperature superconducting (HTS) power applications. To enhance the dielectric properties of cryogenic gas mixtures, in Chapter 2, the addition of various mole fractions of gaseous H_2 and H_2 was proposed, which showed substantial enhancements in dielectric strength [18, 19, 33, 69–71]. Chapter 4 extended the study of Chapter 2 to further improve the dielectric strength of gas mixtures by introducing F_2 and O_2. Yet making practical use of the previous findings requires a development of models that provide accurate estimations on the dielectric strength of individual gases and their mixtures. To model the dielectric strength of gas mixtures, the study uses the Townsend gas discharge theory. According to this theory, determining the coefficients A and B of the empirical formula of the pressure-normalized ionization coefficient (α/p), which describes the number of ionization collisions per unit length in the direction of electric field normalized by gas pressure, is a key step in the development of dielectric strength models. Coefficients A and B in the formula of α/p are obtained through a regression process, which utilizes the formula of α/p and α/p values obtained via experiment or numerical calculation. Conventionally, studies have used the formula of $\alpha/p = Ae^{-Bp/E}$, which relates pressure-normalized electric field E/p to α/p, to derive dielectric strength models [9, 28, 36, 43, 56, 57, 64, 74, 75, 78, 82, 89]. However, some studies used the formula of $\alpha/p = Ae^{-B(p/E)^{1/2}}$ in the dielectric strength modeling process of inert gases,

since it provides higher accuracies during the regression process [57,78]. Nevertheless, the two formulas of α/p, which are referred to as the conventional formulas of α/p in the present study, show limited accuracy in the regression process of α/p under circumstances when the mole fraction or density of a gas varies. Errors in the regression process of α/p lead to limited accuracy in the values of A and B coefficients, which eventually compromise the accuracy of dielectric strength estimations. The main cause of the limited accuracy in the regression process of the conventional formulas of α/p, which eventually impairs the accuracy of estimated dielectric strengths, is the lack of versatility in these equations. To overcome this limitation, the study proposes a versatile formula for α/p by introducing a generalization factor m into the conventional formula. Versatility provided by m enables enhanced accuracy in the regression process leading to improved dielectric strength estimation and accounts for variations in the mole fraction and density of gas mixtures. Based on this idea, the study proposes a versatile modeling procedure which generates an improved dielectric strength model, which can not only predict the dielectric strength of pure gases, but also various gas mixtures with improved accuracy.

7.2 Versatile Modeling Procedure

7.2.1 Overview

The proposed modeling procedure is shown in Figure 49. Initially, the Boltzmann equation is numerically solved based on the two-term approximation method. Solving the Boltzmann equation results in coefficients representing electron kinetic processes including pressure-reduced ionization coefficient α/p [38], which is used in the regression process with the proposed versatile formula of α/p shown in Figure 49(b). The red circles of Figure 49(b) indicate α/p values resulting from the Boltzmann analysis, and the blue lines represent calculated values from the versatile formula of α/p. The multiple blue lines in Figure 49(b) demonstrate the variation in α/p resulting from

the variation in m. Figure 49(c) shows root-mean-square error (RMSE) values, which represent the difference between α/p values from the Boltzmann analysis (*i.e.*, red circles) and the versatile formula of α/p (*i.e.*, blue lines), as a function of m. Subsequently, the m values corresponding to the lowest RMSE are used in the versatile dielectric strength model shown in Figure 49(d). The entire procedure is conducted for each individual gas or gas mixture.

7.2.2 Obtaining the Swarm Parameters (Step 1)

The first step of the versatile modeling procedure is calculating the electron energy distribution function (EEDF) of each gas mixture by solving the Boltzmann equation with the two-term approximation (*i.e.*, Boltzmann analysis) [38]. The Boltzmann equation describes the variation of macroscopic quantities such as particle number and energy.

$$\frac{\partial f}{\partial t} + \upsilon \cdot \nabla f - \frac{e}{m} E \cdot \nabla_{\mathrm{v}} f = C[f], \tag{17}$$

where f is the electron distribution function, υ is the velocity vector, ∇ is the gradient in the position space, e is the elementary charge, m is the electron mass, E is the electric field, ∇_{v} is the gradient in the velocity space, and $C[f]$ is the collision term that represents the rate of change in f. The two-term approximation is used to simplify the Boltzmann equation [38]. However, the accuracy of the two-term approximation method is low when E/N (E: electric field in V/m, N: number of particles per m^3) values are high, in which inelastic collisions are dominant and the electron distribution is highly anisotropic [14, 70]. Nevertheless, the two gases investigated in this study have large elastic momentum-transfer electron scattering cross sections over the entire electron energy, and the E/N is as high as 120 Td (Townsend, 1 Td = 10^{-21} Vm^2), which ensures the accuracy of the two-term approximation method [71]. Once the

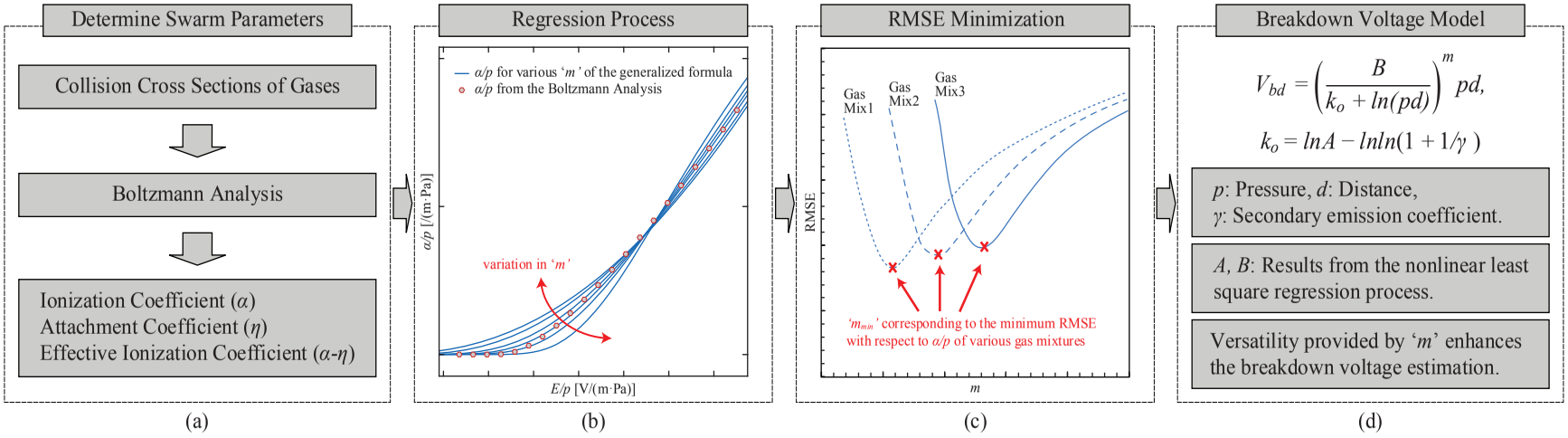

Figure 49: Overview of the proposed versatile modeling procedure: (a) Step 1: Boltzmann Analysis, (b) Step 2: Regression Process, (c) Step 3: Determine m for Best Fit, (d) Step 4: Breakdown Voltage Model Derivation

EEDF is obtained via Boltzmann analysis, α/N is calculated with the use of electron scattering cross sections [38]. The validity of the Boltzmann analysis on gaseous He and H_2 was reported in our previous studies [70, 71] and thus is not discussed here. It should be noted that since α/N is a density-normalized value, this is multiplied by N/p, where p is the gas pressure, to derive α/p.

7.2.3 The Regression Process (Step 2)

To enhance the accuracy of regression processes, this study proposes a versatile formula of α/p. The conventional formula and the proposed versatile formula are shown below.

$$Conventional\ Formula:\ \alpha/p = Ae^{-Bp/E}, \tag{18}$$

$$Versatile\ Formula:\ \alpha/p = Ae^{-B(p/E)^{1/m}}, \tag{19}$$

where A and B are coefficients, which will be determined by the regression process. The difference between the conventional and proposed formula is in the new coefficient m, which is introduced in the exponent of p/E shown in equation (19). With m, the proposed formula of α/p has a degree of freedom that enables adjustment in the regression accuracy, which leads to a higher accuracy in the values of A and B, as shown in Figure 49(b). Note that $1/m$ at the exponent of p/E represents the sensitivity of ionization process α/p with respect to electric field E/p. For example, as the value of $1/m$ increases, α/p increases more rapidly with respect to the increasing values of E/p.

7.2.4 The Root Mean Square Error (Step 3)

α/p values of the Boltzmann analysis and those from the versatile formula of α/p are compared while m is varied. The difference between the two is evaluated in terms of

root-mean-square error defined as

$$\text{RMSE} = \sqrt{\frac{\sum_{k=1}^{n}\left(x_k^* - x_k\right)^2}{n}}, \tag{20}$$

where x_k^* is the true value, x_k is the value from the regression, and n is the number of samples. Once RMSE values are calculated for all m, the value corresponding to the lowest RMSE (*i.e.*, highest regression accuracy) of each gas mixture is identified as m_{min} (Figure 49(c)).

7.2.5 The Breakdown Voltage Model (Step 4)

The versatile dielectric strength model is derived with the use of m_{min} for each gas mixture based on the Townsend breakdown criterion [56, 78].

$$e^{\alpha d} = 1 + \frac{1}{\gamma}, \tag{21}$$

where α is the ionization coefficient, d is the distance between the electrodes, and γ is the secondary electron emission coefficient. The Townsend breakdown criterion describes the condition, in which the discharge current grows to infinity. Substituting equation (18) and (19) into equation (21), respectively, and taking the natural logarithm result in the conventional dielectric strength model (22) and proposed versatile dielectric strength model (23), respectively.

$$Conventional\ Model:\ V_{bd} = \frac{B}{k_o + ln(pd)}pd, \tag{22}$$

$$Versatile\ Model:\ V_{bd} = \left(\frac{B}{k_o + ln(pd)}\right)^m pd, \tag{23}$$

where $k_o = lnA - lnln(1 + 1/\gamma)$. Similar to the difference between (18) and (19), the difference between the conventional and versatile dielectric strength model is in the existence of m.

7.2.6 The Secondary Electron Emission Coefficient

A process, in which free electrons are released from a cathode surface as particles bombard its surface, is called the secondary electron emission. This process generates secondary and subsequent electrons that lead to avalanches required for the growth of current in gas dielectric breakdown and thus plays an important role in the breakdown criterion (21) and k_o of the dielectric strength models (22) and (23). Secondary electron emission coefficient γ is defined as a ratio between the number of released electrons and the number of particles bombarding the cathode surface. Various particles including ions, metastables, fast atoms, and photons contribute to the secondary electron emission. An accurate measurement of γ is not trivial since it depends on the cathode material, gas species, pressure, temperature, and electric field. The beam experiment, an experiment that projects ionic, atomic, molecular beam to the ionizing surface [76], and the swarm experiment, an experiment that requires dielectric breakdown measurements of gases [9, 36, 43], are the main methods used in identifying γ. In other words, obtaining the correct value of γ requires a separate experiment for each gas mixture, electrode material, pressure, and temperature conditions. According to the beam experiment [76], γ consists of ion-induced γ_i, metastable-particle-induced γ_m, photon-induced γ_{ph}, and fast-atom-induced γ_a, but typically dominated by ions (*i.e.*, γ_i) through the Auger process (*i.e.*, potential ejection) [28], which refers to a secondary electron emission process being weakly dependent on ion energy roughly below 500 eV [76]. Therefore, this study takes into account the Auger process, in which γ_i is on the range of 0.01–0.1, but not the kinetic

ejection by ions. The present study uses $\gamma = 0.1$ and $\gamma = 0.01$ for pure He and He-based gas mixtures containing H_2, respectively.

7.3 The Dielectric Strength Estimation of Helium and Hydrogen

This section compares the dielectric strength estimation of the versatile model, derived from the versatile modeling procedure, to that of the conventional model that uses values from the literature. The coefficients in the formula of α/p including m, A, B, and the range of E/p are included in Table 5. The table includes coefficients for He and H_2 gases from the literature and those obtained through the versatile modeling procedure of this study. The values of A and B in Table 5 are in SI units, which were converted from the original values in the literature. Note that the range of E/p is where A and B values remain constant (*i.e.*, the range of E/p that is used in the regression process to determine the values of A and B). Using the coefficients in Table 5, the dielectric strengths of He and H_2 gases are calculated and shown in Figures 4 and 5. The estimated dielectric strengths (*i.e.*, breakdown voltages) are plotted using lines, and the experimental measurements are in x-markers. In both Figures 4 and 5, blue solid lines represent the dielectric strength estimation from the versatile model, and the red broken lines represent those of the conventional model using coefficients from the literature.

The figures show that the closest agreement with the experimental measurements is reached by the dielectric strength estimation of the versatile model for both He and H_2 gases. Among the dielectric strength estimations of the conventional models, coefficients from Lieberman *et al.* [56] and Petrovic *et al.* [75] produce relatively close agreements with the experimental measurements in the case of He (Figure 52), but none of them does so in the case of H_2 (Figure 53). The accuracy in the dielectric strength estimation demonstrated by the versatile modeling procedure is mainly due to the generalization factor m, which provides versatility and accuracy in the

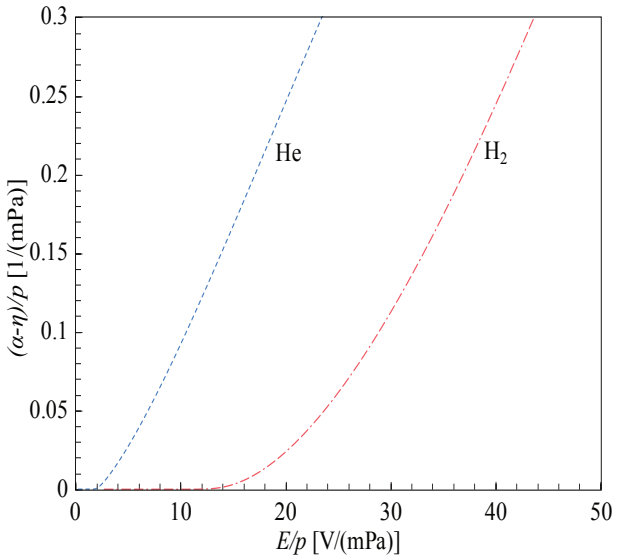

Figure 50: Pressure-normalized effective ionization coefficients of He and H_2.

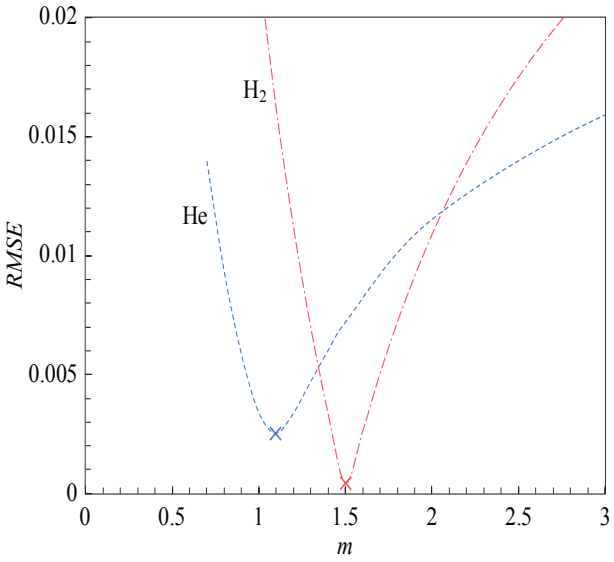

Figure 51: Root mean square error variations in He and H_2.

regression process of α/p.

Table 5 includes two different types of the conventional formulae of α/p: one with $m = 1$ and the other with $m = 2$. The limiting factor in the two conventional formula of α/p is the fixed value of m (*i.e.*, either fixed to 1 or 2). The lack of versatility of m in the conventional formula of α/p limits the accuracy in the regression process of α/p, which varies by gas species as shown in Figure 50. The difference in the α/p values of He and H_2 cannot be taken in to account by using the conventional formula of α/p. However, the versatile formula of α/p, which enables the use of any m value corresponding to the minimum regression error, can adjust to various gas species. Values corresponding to the minimum regression errors m_{min} are 1.1 for He and 1.5 for H_2 as shown in Figure 51. Because 1.1 is relatively close to 1 and 1.5 is't, the dielectric strength estimations from the conventional model and the versatile model would be closer in He than in H_2 (Figures 52 and 53).

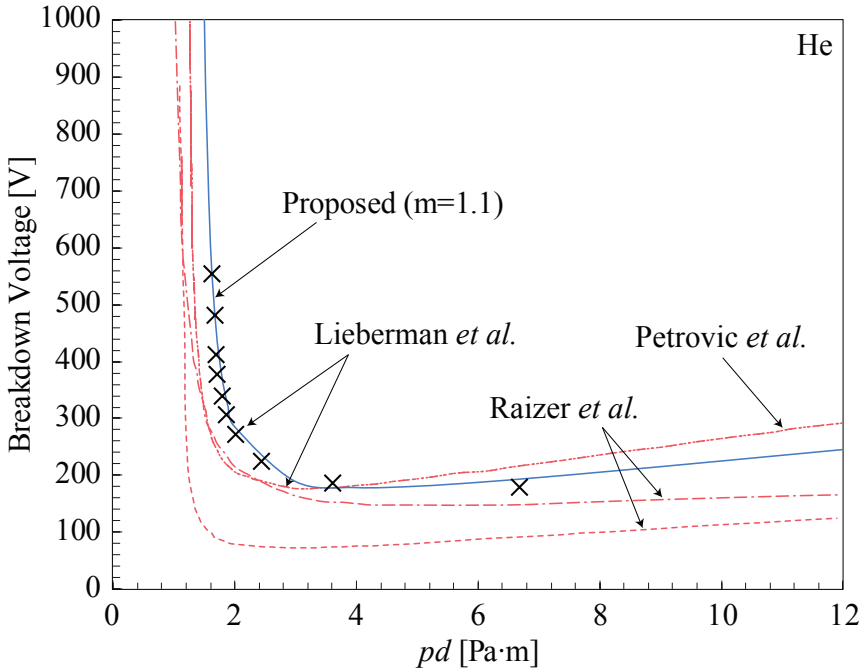

Figure 52: Breakdown voltage comparison of He: calculated values based on coefficients A and B from the proposed versatile modeling procedure (solid line), calculated values based on coefficients A and B from the literature (broken lines: Lieberman *et al.* [56], Raizer *et al.* [78], Petrovic *et al.* [75]), and experimental values (x markers: Lieberman *et al.* [56]).

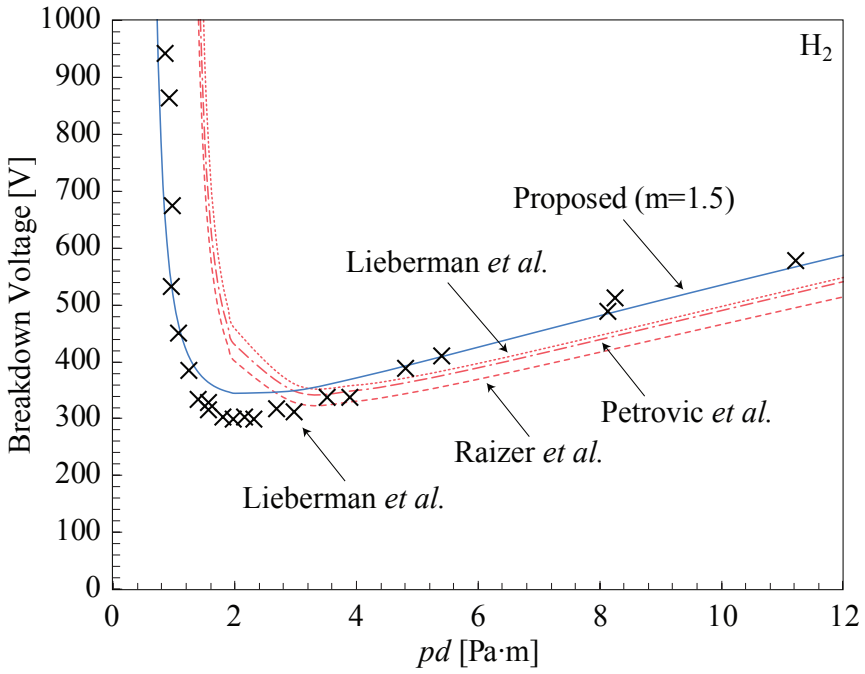

Figure 53: Breakdown voltage comparison of H_2: calculated values based on coefficients A and B from the proposed versatile modeling procedure (solid line), calculated values based on coefficients A and B from the literature (broken lines: Lieberman *et al.* [56], Raizer *et al.* [78], Petrovic *et al.* [75]), and experimental values (x markers: Lieberman *et al.* [56]).

Table 5: Original source and parameters used in the dielectric strength estimation of helium and hydrogen.

Original source of He	m	A [(m·Pa)$^{-1}$]	B [(V/(m·Pa))$^{1/m}$]	Range of E/p [V/(m·Pa)]
Lieberman *et al.* [56]	1	2.10	57.75	22.5–187.5
Raizer *et al.* [78], Go *et al.* [28]	1	2.25	25.50	15–112.5
Raizer *et al.* [78], Go *et al.* [28]	2	3.30	10.50	75–
Petrović *et al.* [75]	1	2.10	57.83	24.7–185
Present Study	1.1	1.73	33.61	49.7–51.9
Original source of H_2	m	A [(m·Pa)$^{-1}$]	B [(V/(m·Pa))$^{1/m}$]	Range of E/p [V/(m·Pa)]
Lieberman *et al.* [56]	1	3.60	102.01	11.2–450
Raizer *et al.* [78], Go *et al.* [28]	1	3.75	97.51	112.5–450
Raizer *et al.* [78], Go *et al.* [28]	2	-	-	-
Petrović *et al.* [75]	1	3.71	102.07	11.1–222
Present Study	1.5	9.02	42.19	39.8–49.4

7.4 The Dielectric Strength Estimation of Helium-Hydrogen Mixtures

7.4.1 AC Breakdown Experiment

To confirm the improved dielectric strength estimation performance of the proposed modeling procedure, the study conducted experimental AC breakdown measurements on various gas mixtures containing gaseous He and H_2. The breakdown measurements were conducted at 293 K and 77 K at gas pressures in the range of 0.5–2.0 MPa. The measurements demonstrate a closer agreement with the versatile model than with the conventional models.

AC breakdown measurements were performed to characterize the dielectric strength of gaseous He with various additions of H_2 at both 293 K and 77 K. The AC breakdown voltage of various types of gases were determined by measuring the voltage to arc across a pair of electrodes with an axially symmetric 25.1 mm diameter Bruce profile, which generates a uniform electric field [80]. The top electrode was connected to a 100 kV, 5 kVA, 60 Hz AC transformer, and the bottom electrode was grounded. The gap distance between the electrodes was set to a fixed distance of 2 mm for all experiments while the gas pressure was varied. Note that Paschen's law is valid when

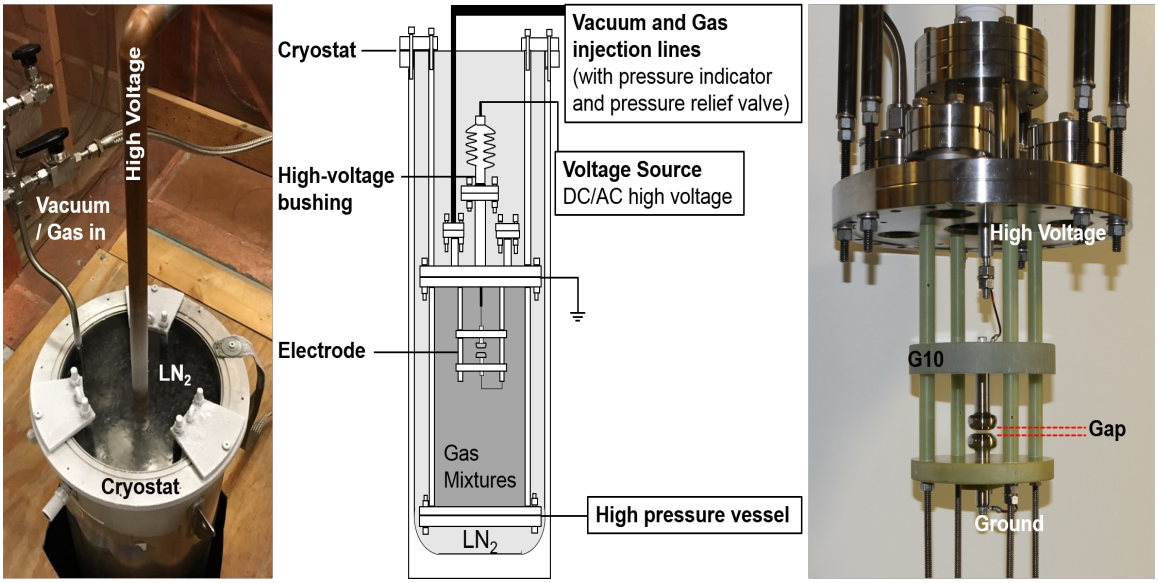

Figure 54: The electrode system with the uniform electric field in the gap between the electrodes [18].

the ratio of gap length to electrode radius is constant throughout the breakdown measurement. That is, one should change the gas pressure instead of the gap distance to change pd. If gap distance d is increased instead of gas pressure p, breakdown voltage will increase more than it would when p is increased while d is constant because of the increased radial diffusion of charged particles [57]. The electrode setup was installed within a sealed pressure vessel as shown in Figure 54, and care was taken to ensure a high purity environment before measurements were taken for each gas mixture. Initial AC breakdown measurements were performed to season the electrodes before collecting data. Fifteen AC breakdown measurements were performed at 2.0 MPa, 1.5 MPa, 1.0 MPa, and 0.5 MPa, respectively, for He-based gas mixtures with 0, 1, 2, and 4 mol% H_2 at 293 K and 77 K. There is a possibility for measurements to be carried out at a gap distance up to 4 mm, which will be undertaken in the future to add further verification to the results discussed in this paper. More information on the experimental setup and procedure are outlined in [18, 33].

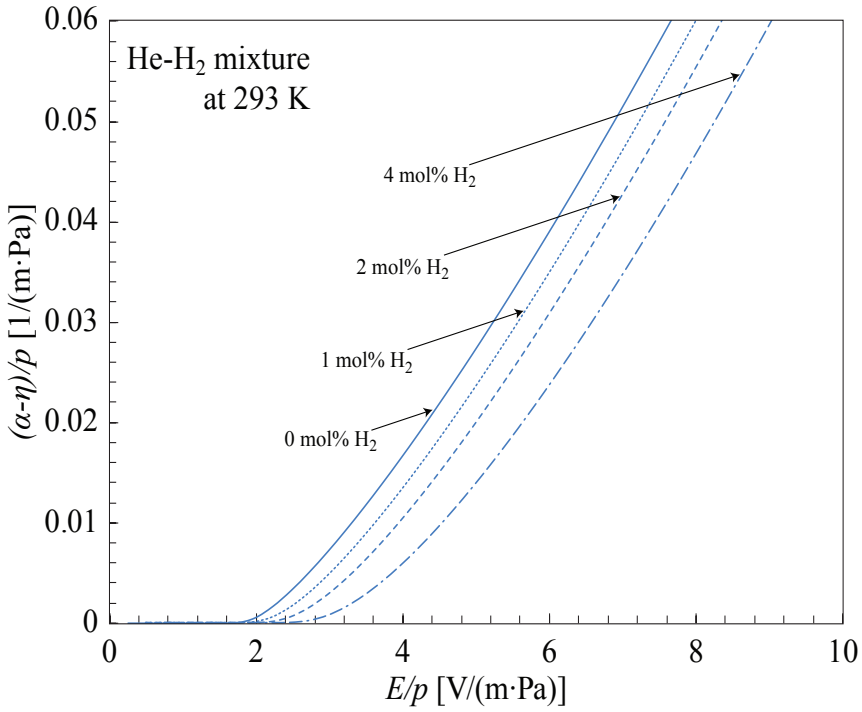

Figure 55: Pressure-normalized effective ionization coefficients of various He-H_2 mixtures at 293 K.

7.4.2 Helium-Hydrogen Gas Mixtures at 293 K

The versatile modeling procedure is not only capable of providing enhanced accuracy in the breakdown strength estimation, but also capable of maintaining the accuracy of a varying dielectric strength in gas mixtures. A gas mixture's dielectric strength changes when the mole fractions of the components of the gas mixture changes. In some cases, mole fractions are deliberately altered to enhance the dielectric properties of gas mixtures. Our previous studies on the dielectric properties of gaseous He have shown that increasing the mole fraction of H_2 in He-based gas mixtures reduces α/p and thus enhances the dielectric strength [18, 69–71]. The present study utilizes our previous findings to validate the versatile modeling procedure that can take α/p variations into account. Figure 55 shows a variation in α/p caused by increasing mole fraction of H_2 in a He-based gas mixture. According to the figure, α/p reduces and becomes positive at higher E/p values as the mole fraction of H_2 in the He-based gas

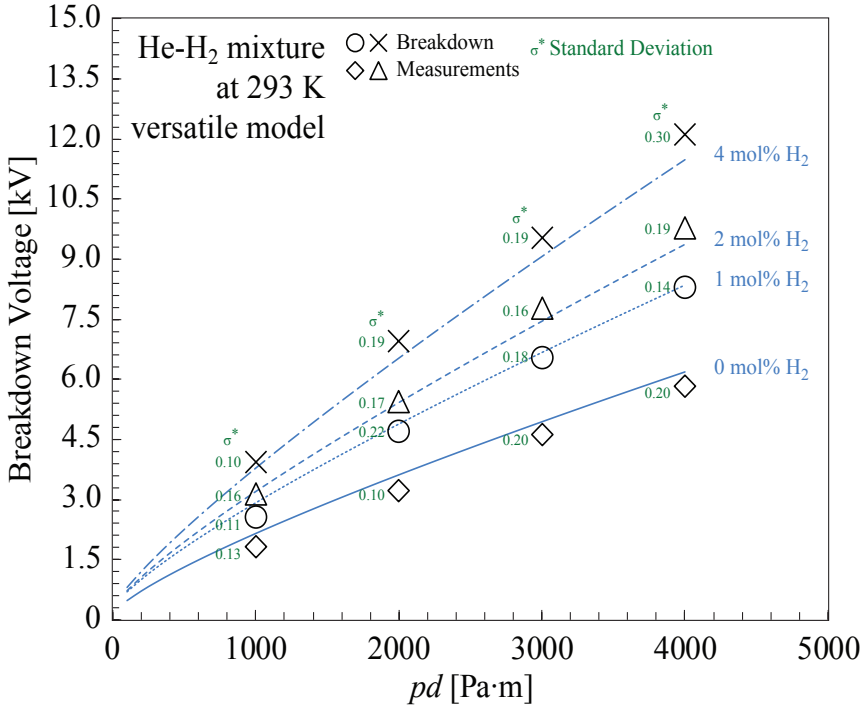

Figure 56: Breakdown voltage comparison of He-H_2 mixtures: experimental measurements vs. values of the versatile model at 293 K.

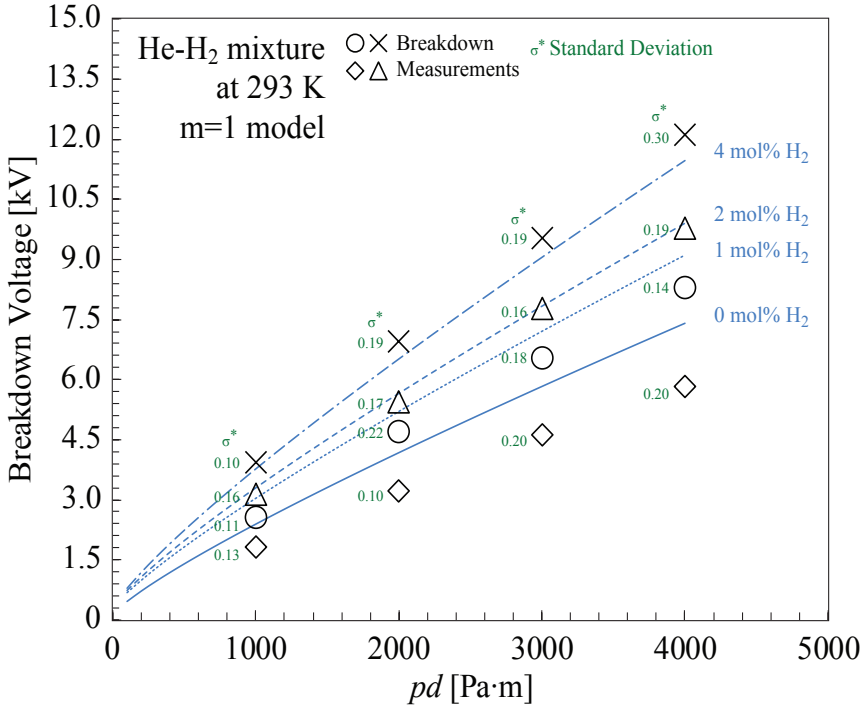

Figure 57: Breakdown voltage comparison of He-H_2 mixtures: experimental measurements vs. values of the conventional model with $m = 1$ at 293 K.

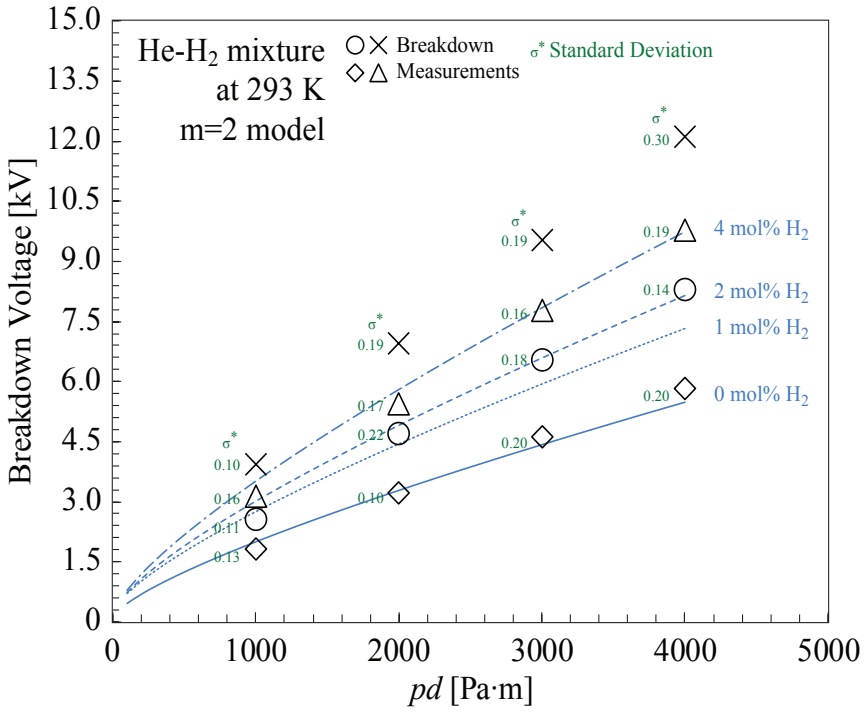

Figure 58: Breakdown voltage comparison of He-H_2 mixtures: experimental measurements vs. values of the conventional model with $m = 2$ at 293 K.

mixture increases, which indicates a reduction in the ionization collision process.

The study performs the regression process using both the conventional and versatile formula of α/p and apply the Townsend breakdown criterion to derive the conventional and versatile dielectric strength models of gas mixtures. The coefficients resulting from the regression process of He-H_2 gas mixtures at 293 K are listed in Table 6. Varying m_{min} values, which results from the proposed versatile modeling procedure, are shown in Table 6. For 96-4 mol% He-H_2 gas mixture, m_{min} is 1.0, which is equivalent to the conventional model with $m = 1$. As a result, the values of A and B are identical in the case of 96-4 mol% He-H_2 gas mixture as shown in the fifth and tenth rows of Table 6, which indicates that an identical dielectric strength estimation is generated from both the versatile and conventional (m=1) models. Based on the values of Table 6, the dielectric strength estimations of the conventional and versatile models are plotted in Figures 56–58. The markers indicate the data from breakdown measurements at 293 K described in the previous section, and the lines are the results

Table 6: Parameters used in the dielectric strength estimation of He-H_2 mixtures at 293 K.

He-H_2 [mol%]	m_{min} (Versatile)	A [(m·Pa)$^{-1}$]	B [(V/(m·Pa))$^{1/m}$]	Range of E/p [V/(m·Pa)]
100-0	1.5	0.681	9.41	0.25–8.65
99-1	1.3	0.534	10.8	0.25–8.65
98-2	1.2	0.490	12.3	0.25–8.65
96-4	1.0	0.374	16.6	0.25–8.65
He-H_2 [mol%]	m (Conventional)	A [(m·Pa)$^{-1}$]	B [(V/(m·Pa))$^{1/m}$]	Range of E/p [V/(m·Pa)]
100-0	1	0.263	11.3	0.25–8.65
99-1	1	0.291	12.6	0.25–8.65
98-2	1	0.317	13.9	0.25–8.65
96-4	1	0.374	16.6	0.25–8.65
He-H_2 [mol%]	m (Conventional)	A [(m·Pa)$^{-1}$]	B [(V/(m·Pa))$^{1/m}$]	Range of E/p [V/(m·Pa)]
100-0	2	1.784	9.37	0.25–8.65
99-1	2	2.246	10.2	0.25–8.65
98-2	2	2.875	11.2	0.25–8.65
96-4	2	4.464	12.9	0.25–8.65

from the conventional and versatile models. Note that the markers in Figures 56–58, which represent the experimental breakdown measurements at 293 K, are identical in all three figures. Figure 56 shows the estimation results of the versatile dielectric strength model. The validity of the versatile model is demonstrated by the close agreement of the results of breakdown measurements as the mole fraction of H_2 in the gas mixture increases. However, the conventional models derived from the formula of α/p with either $m = 1$ or $m = 2$ failed to maintain close agreements with the values of the breakdown measurements as shown in Figures 57 and 58. The conventional model with $m = 1$ shows the lowest agreement with the breakdown measurements of pure He (Figure 57). The conventional model with $m = 2$ shows close agreement with the breakdown measurements of pure He, but deviates as the mole fraction of H_2 increases (Figure 58). The limited performances of the two conventional models are mainly due to the lack of versatility in those models. Again, the conventional formula of α/p is not capable of fulfilling the accurate regression process of α/p values when α/p changes as the composition of a gas mixture varies, and this results in the limited accuracy of dielectric strength estimations.

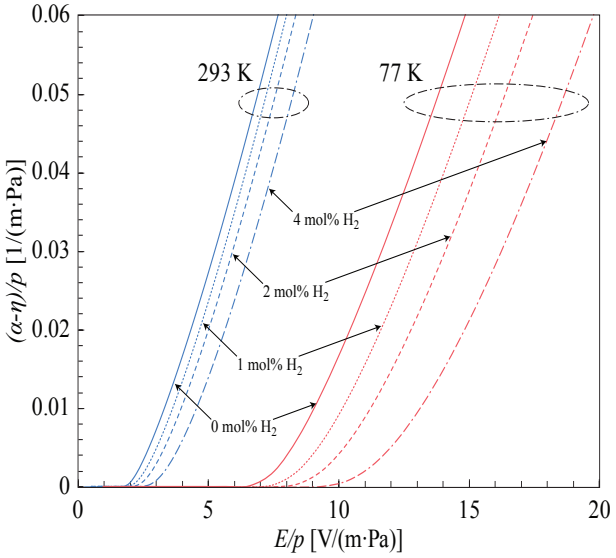

Figure 59: Variation in pressure-normalized effective ionization coefficients of 100-0 mol% He-H_2 mixture due to temperature decrease from 293 K to 77 K.

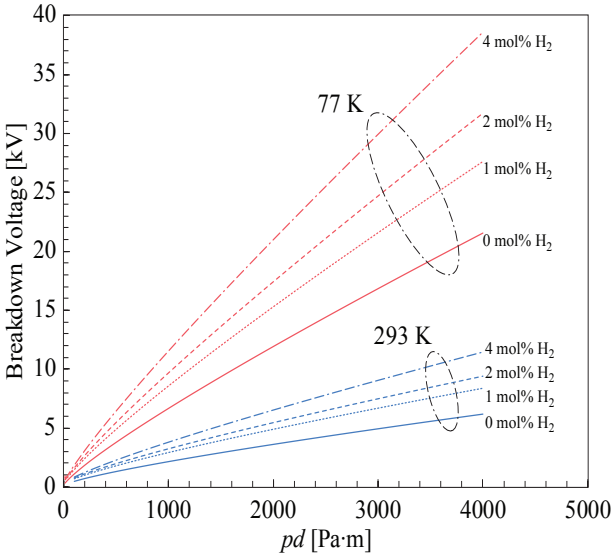

Figure 60: Variation in the dielectric strength of 100-0 mol% He-H_2 mixture due to temperature decrease from 293 K to 77 K.

7.4.3 Accounting for Gas Temperature (Density) Variations

The main advantage of using the versatile formula of α/p is that it can maintain the dielectric strength estimation performance even when α/p values vary. The variation in α/p is not only caused by the gas composition, but also by the gas temperature, which plays a role when α/N is converted into α/p. Solving the Boltzmann equation initially produces the density-reduced ionization coefficient α/N, which is then multiplied by N/p to become α/p. According to the ideal gas law, N/p is equivalent to $1/kT$ per volume, where k is the Boltzmann constant and T is the gas temperature. The relationship between N/p and $1/kT$ indicates an inversely proportional correlation between gas temperature T and gas density N. Therefore, variation in gas temperature alters gas density as well as the values of α/p. It should be noted that this procedure is not merely relating the dielectric strength of a gas mixture to the density N of the gas mixture. Rather it is the regression process of α/p values that takes into account the variation in α/p caused by the change of gas temperature.

The result of gas temperature decreasing from 293 K to 77 K in the He-based gas mixtures with 0–4 mol% H_2 is shown in Figure 59 and 60. All four α/p values of the He-H_2 gas mixtures at 77 K are lower than those of the He-H_2 gas mixture at 293 K, which suggests that even pure He gas at 77 K produces fewer free electrons through ionization collisions under certain E/p compared to 96-4 mol% He-H_2 gas mixture at 293 K. This trend also indicates that pure He gas at 77 K has a stronger dielectric strength than that of 96-4 mol% He-H_2 gas mixture at 293 K (Figure 59). Accordingly, the shifted α/p values result in new sets of coefficients, which lead to increasing the breakdown strengths of the gas mixtures at 77 K (Figure 60).

7.4.4 Helium-Hydrogen Gas Mixtures at 77 K

This section continues the verification process of the versatile model with various compositions of He-H_2 gas mixture at 77 K. Varying α/p, which is caused by increasing mole fraction of H_2, at 77 K is shown in Figure 61. Similar to the He-H_2 gas mixtures at 293 K, α/p also decreases and becomes positive at higher E/p values as the mole fraction of H_2 increases in the He-based gas mixture at 77 K.

The study performs the regression process using both the conventional and versatile formula of α/p and apply the Townsend breakdown criterion to derive the conventional and versatile dielectric strength models of gas mixtures. The coefficients resulting from the regression process of He-H_2 gas mixtures at 77 K are listed in Table 7. Varying m_{min} values, which results from the proposed versatile modeling procedure, are shown in Table 7. For pure He, the m_{min} is 1.0, which is equivalent to the conventional model with $m = 1$. As a result, the values of A and B are identical in the case of pure He as shown in the second and seventh rows of Table 7, which indicates that an identical dielectric strength estimation result from both versatile and conventional (m=1) models. Similar to the results of 293 K, m_{min}

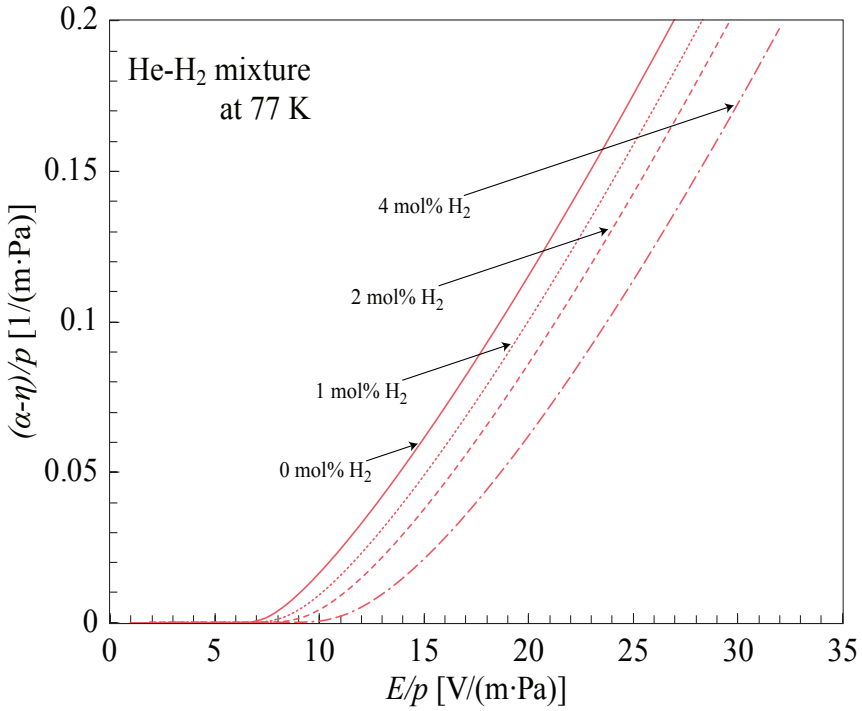

Figure 61: Pressure-normalized effective ionization coefficients of various He-H_2 mixtures at 77 K.

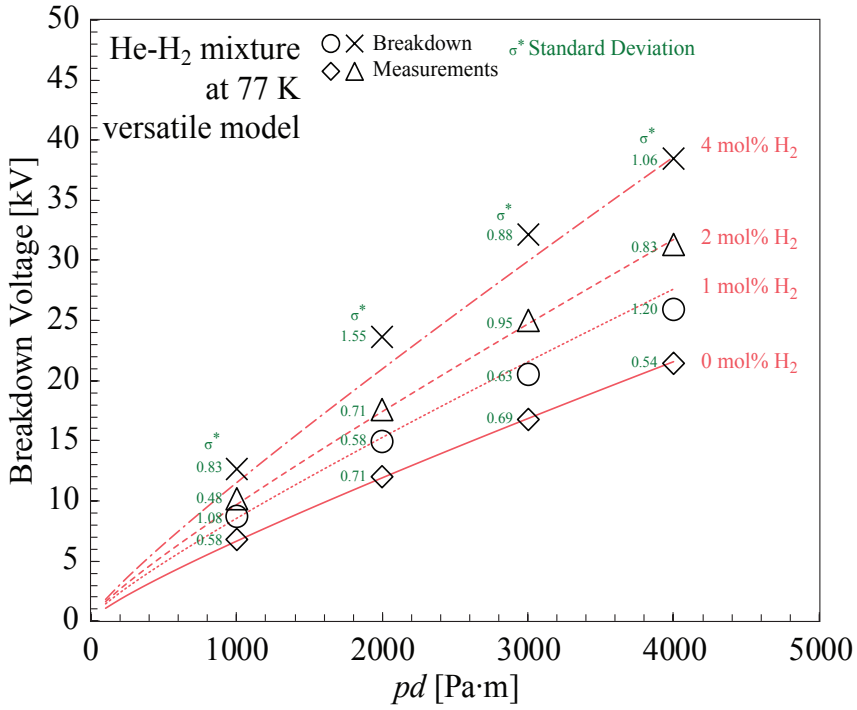

Figure 62: Breakdown voltage comparison of He-H_2 mixtures: experimental measurements vs. values of the versatile model at 77 K.

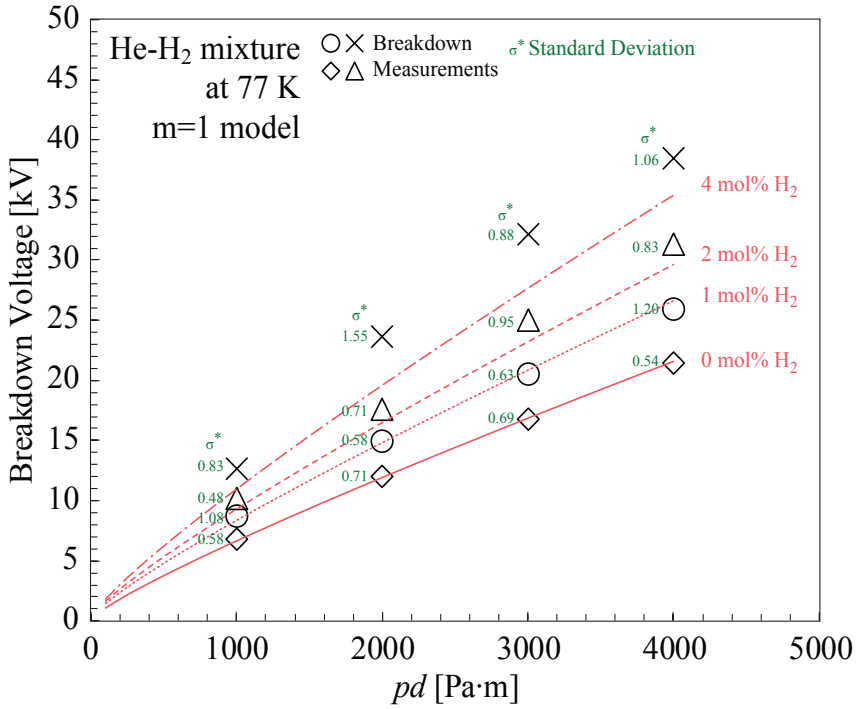

Figure 63: Breakdown voltage comparison of He-H_2 mixtures: experimental measurements vs. values of the conventional model with $m = 1$ at 77 K.

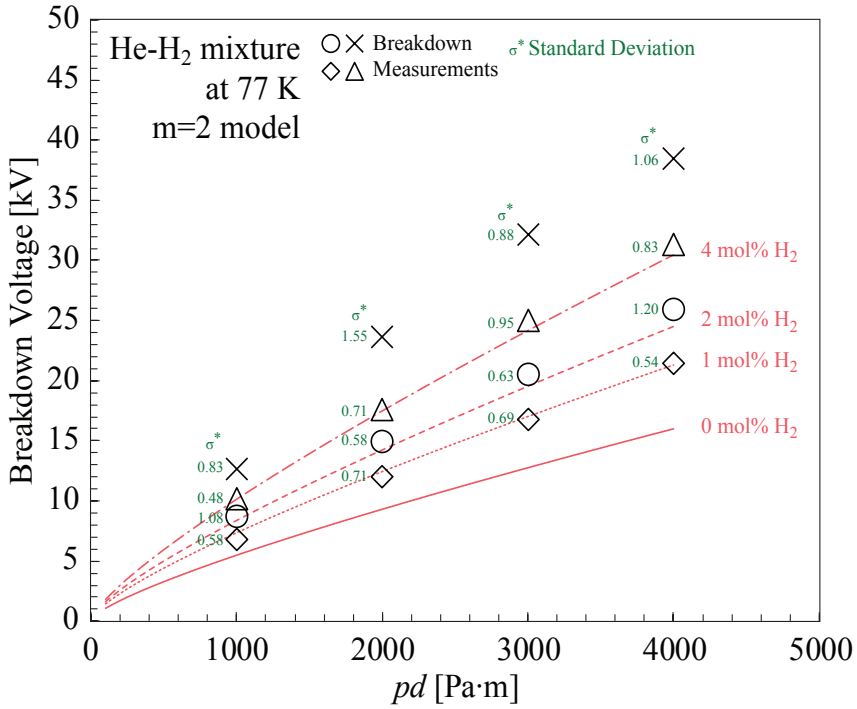

Figure 64: Breakdown voltage comparison of He-H_2 mixtures: experimental measurements vs. values of the conventional model with $m = 2$ at 77 K.

Table 7: Parameters used in the dielectric strength estimation of He-H_2 mixtures at 77 K.

He-H_2 [mol%]	m_{min} (Versatile)	A [(m·Pa)$^{-1}$]	B [(V/(m·Pa))$^{1/m}$]	Range of E/p [V/(m·Pa)]
100-0	1.0	0.813	38.9	0.25-6.18
99-1	0.9	0.736	55.3	0.25-6.18
98-2	0.8	0.632	83.8	0.25-6.18
96-4	0.7	0.553	157.0	0.25-6.18
He-H_2 [mol%]	m (Conventional)	A [(m·Pa)$^{-1}$]	B [(V/(m·Pa))$^{1/m}$]	Range of E/p [V/(m·Pa)]
100-0	1	0.813	38.9	0.25-6.18
99-1	1	0.943	44.7	0.25-6.18
98-2	1	1.091	50.8	0.25-6.18
96-4	1	1.424	63.0	0.25-6.18
He-H_2 [mol%]	m (Conventional)	A [(m·Pa)$^{-1}$]	B [(V/(m·Pa))$^{1/m}$]	Range of E/p [V/(m·Pa)]
100-0	2	8.097	19.0	0.25-6.18
99-1	2	11.33	21.2	0.25-6.18
98-2	2	17.16	23.8	0.25-6.18
96-4	2	34.24	28.4	0.25-6.18

decreases as the mole fraction of H_2 increases at 77 K. Based on the values of Table 7, the dielectric strength estimations of the conventional and versatile models are plotted in Figures 62–64. The markers indicate the data from experimental breakdown measurements described in Section 4.1, and the lines indicate the results of the conventional and versatile models. Note that the markers in Figures 62–64, which represent the experimental breakdown measurements at 77 K, are identical in all three figures. Figure 62 shows the results of the versatile dielectric strength model. The performance of the versatile model is validated by the close agreement with the values of the breakdown strengths obtained from the measurements as the mole fraction of H_2 increases. However, the conventional models failed to maintain close agreements with the values of the breakdown measurements as shown in Figures 63 and 64. The conventional model with $m = 1$ shows a relatively close agreement with the breakdown measurements of 0 and 1 mol% H_2 mixtures, but deviates as the mole fraction of H_2 further increases (Figure 63). All four mixtures of the conventional model with $m = 2$ show significant discrepancies with the breakdown measurements (Figure 64). Again, the limited performances of the two conventional models are mainly due to the lack of versatility in them.

7.5 Summary

This chapter presented a new procedure that improves the dielectric strength estimation of gas mixtures for cryogenic and superconducting applications, which provides enhanced accuracy in the estimation of breakdown strength of gases and the capability of maintaining the estimation accuracy while the dielectric strength of a gas mixture varies as the composition of it changes. The versatile formula of α/p, which serves as a basis in the versatile modeling procedure, provides versatility and enhanced accuracy in the regression process of α/p values that lead to improvements in the dielectric strength estimation of gas mixtures. The value of generalization factors that provide the highest accuracy in the regression process are identified and used for deriving versatile dielectric strength models for each gas mixture based on the Townsend breakdown criterion. The validity of the versatile modeling procedure was confirmed by comparing the dielectric strength estimation of the versatile model to the experimental breakdown measurements of various He-H_2 gas mixtures under ambient and cryogenic gas temperatures. According to the results of the present study, the versatile modeling procedure resulted in the closest agreement with the experimental measurements and maintained the quality of estimation throughout variation in temperature and the mole fraction of gas mixture.

CHAPTER VIII

EVALUATING THE DIELECTRIC STRENGTH OF CRYOGENIC GAS MIXTURES BY PLASMA PARAMETER MEASUREMENTS

8.1 Motivation

Electrostatic probe, known as the Langmuir probe, is a widely used tool for measuring plasma parameters in low-pressure and low-temperature plasmas. To obtain the plasma parameters, electron energy distribution functions (EEDF) are derived from measured I-V characteristic curves based on a method known as the Druyvesteyn method [29]. Unlike solving the Boltzmann equation with the two-term approximation, which is possible only when the electron scattering cross section data are available, the Langmuir probe plasma diagnostics method does not require cross section data for obtaining EEDF's. This chapter discusses the process of obtaining EEDF's without the electron scattering cross section data and how the plasma parameters are derived from the measured EEDF's.

In this chapter, low-temperature plasmas are generated in a vacuum chamber, I-V characteristic curves are measured with a lab-made electrostatic probe, EEDF's are calculated using the Druyvesteyn method, and plasma parameters are derived. In addition, the measured plasma parameters are compared with the values of the global model.

8.2 Experimental Setup

Figure 65 shows the experimental setup used for the plasma measurements discussed in this chapter. The experiments were conducted in a plasma chamber made with

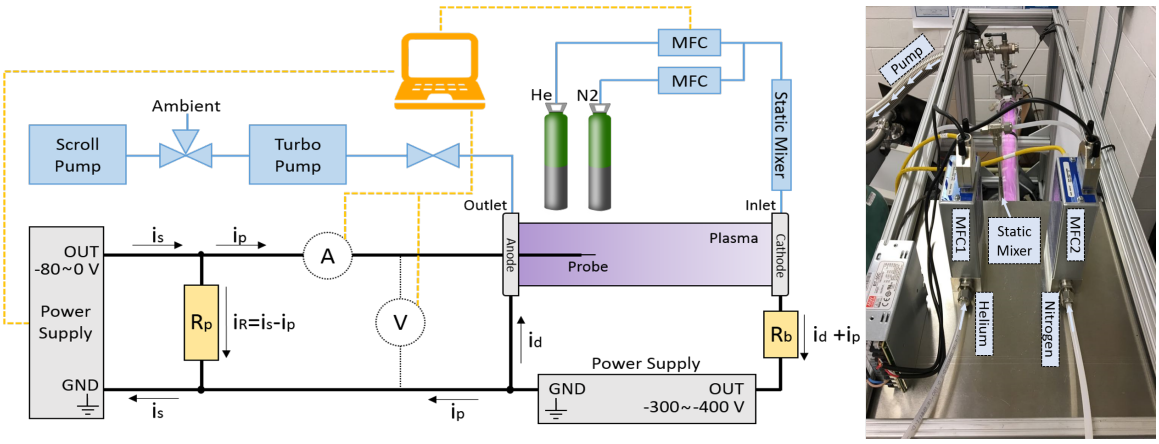

Figure 65: The experimental setup for the Langmuir probe plasma measurement.

a cylindrical borosilicate glass (Pyrex) tube with dimensions of 51 mm in diameter and 600 mm in length. The chamber is equipped with an anode and cathode made of stainless steel placed on each end. A negative DC voltage of -300 to -400 V was applied to the cathode using a DC power supply while keeping the anode grounded (*i.e.*, kept at 0 V). A static mixer and two mass flow controllers (MFC) were used to combine two different gases in required compositions by controlling the flow rates of individual gases in the units of sccm (standard cubic centimeter per minute). The gas pressure in the chamber was maintained and monitored at 30 mTorr (3.99 Pa) by a calibrated absolute capacitance manometer (MKS Baratron). A single-tip Langmuir probe made with a cylindrical tungsten wire with the dimensions of 0.125 mm in diameter and 10 mm in length was placed at the center of the positive column of DC plasmas generated by various combinations of He and N_2 gases. The I-V characteristic curves of the He-N_2 plasmas were measured through a digital multimeter (Rigol DM3058E) by sweeping the probe voltage from -80 to 0 V. Then, the Druyvesteyn method was used to convert the measured I-V curves into the electron energy probability function (EEPF), which can be easily converted into EEDF. It should be note that the single tip Langmuir probe method requires the plasma to be in contact with the grounded anode to form a closed circuit [73].

8.3 Experimental Conditions

8.3.1 Non-local Electron Kinetics

In DC plasmas, electrons mainly gain energy at the high-voltage sheath, the cathode fall region, and dissipates energy elsewhere in a plasma chamber. This process is known as non-local electron kinetics and becomes more active under lower gas pressures or when a gas forming the plasma has a simpler set of cross sections. At a relatively high gas pressure or when a gas with complex cross sections are used, electrons tend to dissipate energy in the vicinity of where they gained energy. When the location of electron energy gain and loss is similar, electron kinetics is local. For DC plasma diagnosis experiments, the local electron kinetics should be minimized since it causes striations, which is formed by repeating electron energy gain and dissipation through the plasma column. Non-local conditions in plasmas are confirmed by calculating the electron energy relaxation length, which represents the total length an electron would have to travel to entirely dissipate its energy. Calculating an electron energy relaxation length requires the cross section information (σ) and particle number density (n_g) of the subject gas.

$$\lambda_\epsilon = \sqrt{\frac{\lambda_m \lambda^*}{3}}, \tag{24}$$

where λ_m is a mean free path that accounts for the momentum transfer processes and λ^* is a mean free path that accounts for all collisional energy losses.

$$\lambda_m = \frac{1}{n_g \sigma_m}, \tag{25}$$

$$\lambda^* = \frac{1}{n_g[(2m/M)\sigma_{el} + \sigma_{ex} + \sigma_{iz}]} \tag{26}$$

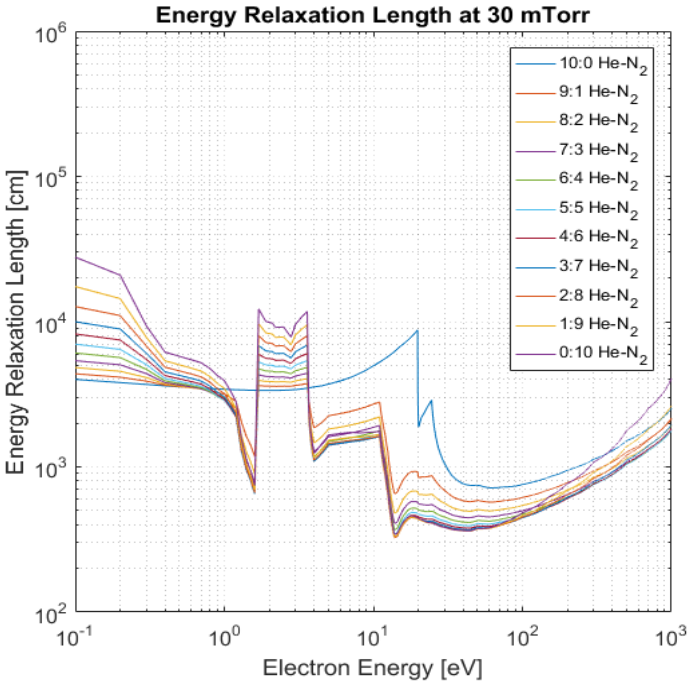

Figure 66: The electron energy relaxation length of He-N_2 plasmas at 30 mTorr.

Generally, one could ensure the non-local kinetics of a plasma when the energy relaxation length is greater than the discharge length. Figure 66 shows the calculated electron energy relaxation length of He-N_2 plasmas as a function of electron energy. As shown in the figure, the shortest energy relaxation length, which is longer than 100 cm, is observed around 15 eV in pure N_2 plasma. Since the total length of the plasma chamber is 60 cm and the discharge length is shorter than the chamber length, non-local condition is ensured in the experiment.

8.3.2 Collisionless Probe Sheath

Appling the Druyvesteyn method, which will be discussed in detail in Section 8.4.2, for the derivation of EEDF's from I-V characteristic curves, requires the condition of collision-less probe sheath. For the condition to be satisfied, the size of the probe tip should be small enough such that it satisfies the small probe inequality for cylindrical probes with radius r.

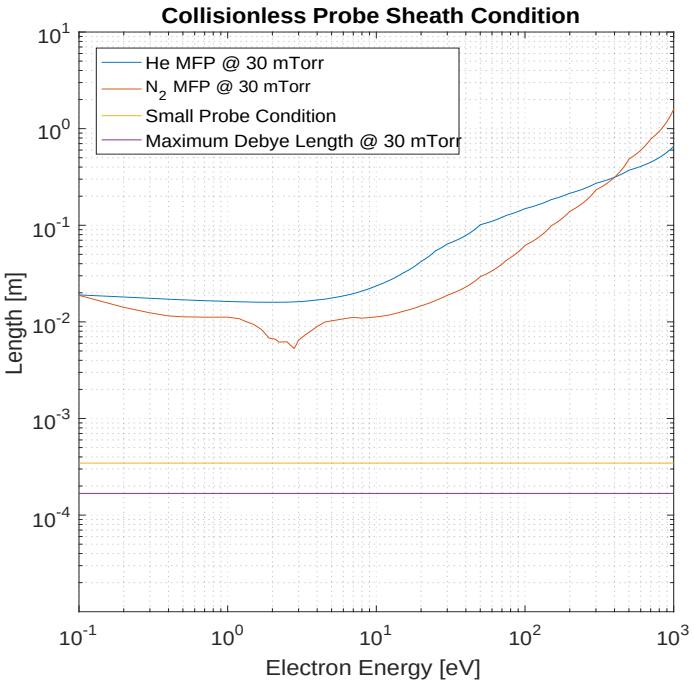

Figure 67: Electron mean free path and the collisionless probe sheath condition at 30 mTorr

$$r \ln\left(\frac{\pi l}{4r}\right), \ \lambda_D << \lambda_e, \tag{27}$$

where λ_e is the electron mean free path defined as follows.

$$\lambda_e = \frac{1}{\sigma_{tot} n_g}, \tag{28}$$

where σ_{tot} is the total cross section of a gas species and n_g is gas particle density. In the present study, the gas pressure of 30 mTorr is used, and the calculated results are presented in Figure 67. The figure shows that the mean free paths of He and N_2 are orders of magnitude longer than the small probe condition satisfying the inequality. Although 30 mTorr is low enough to satisfy the inequality for this study, lower gas pressure could be necessary when gas species with larger σ_{tot} are used in electrostatic probe DC plasma experiments.

8.4 Plasma Parameter Measurement

8.4.1 I-V Characteristic Curve

When the probe voltage is strongly negative, probe current mainly consists of ions, which generally have substantially larger mass and lower velocities than electrons. The larger mass of ions results in a comparatively small magnitude of negative ionic current. Note that the positive current direction points out from the probe tip. As the probe voltage is increased, probe current slowly increases and reaches a voltage, in which ionic current equals electronic current (*i.e.*, zero net current). The electric potential corresponding to this point is the floating potential. As the probe voltage is further increased, electron current increases exponentially until the probe voltage reaches the plasma potential. At plasma potential, probe potential and plasma potential are in equilibrium, which indicates the absence of electric potential barrier between the two. Due to the lack of electric potential barrier between the probe tip and plasma, electrons of all energy can enter the probe. Hence, the probe current, which is determined by the surface area of the probe and plasma density, saturates. However, in practice, a further increase in the probe potential increases the probe sheath thereby increasing the effective surface area of the probe, which enables the probe to collect more electronic current. Due to the increasing collection area, I-V curves don't show a clear knee as in their ideal from, but still show a change in their slope. Figure 68 shows an example of a measured I-V characteristic curve of a plasma. As discussed, it is difficult to identify the knee of the curve. It should be noted that larger probes generate more clear I-V curves. However, since larger probes have larger radius and surface area, larger probe current is extracted from the plasma during measurement, which could lead to plasma perturbation.

8.4.2 Druyvesteyn Method and EEDF

Deviation from Maxwellian EEDF due to non equilibrium electrons is typical in low temperature gas discharges. The typical conditions of low temperature plasmas are pressures ranging between 0.1–100 mTorr and plasma densities between 10^{12}–10^{20} m^{-3}. Under these conditions, the non thermal equilibrium is not only observed between electrons and neutrals or between electrons and ions, but also within the electron ensemble itself. Conventional techniques that utilize the ion and electron part of I-V curves without deriving EEDF's in obtaining plasma parameters are inadequate for low temperature plasma measurements. Inferring plasma parameters from the ion part of I-V curves is mainly inaccurate since the ion part only contains the high-energy electron information of EEDF's, which does not represent the effective electron energy of a plasma unless electrons are in thermal equilibrium. Furthermore, inferring plasma parameters from the electron part of I-V curves is not always accurate because the conventional Langmuir technique assumes Maxwellian electron distribution. In general, low pressure gas discharge EEDF's are non-Maxwellian even at energy below the threshold energy of inelastic collisions (*i.e.*, $\epsilon < \epsilon^*$). Therefore, beginning an analysis by assuming that an electron energy distribution is a certain type of distribution function (*i.e.*, Maxwellian) is not acceptable.

The most accurate way to obtain an EEDF is using the Druyvesteyn method. In 1931, Druyvesteyn demonstrated that EEPF's are proportional to the second order derivative of probe current as shown below [29].

$$f(\epsilon) = 2(2m_e)^{1/2}(e^3A)^{-1}\frac{d^2I_p}{dV_p^2}, \tag{29}$$

where m is the electron mass, e is the elementary charge, I_p is the probe current, V_p is the probe voltage, and A is the surface area of the probe tip. An example of an EEPF is presented in Figure 69. Once the EEPF's are obtained, the electron energy

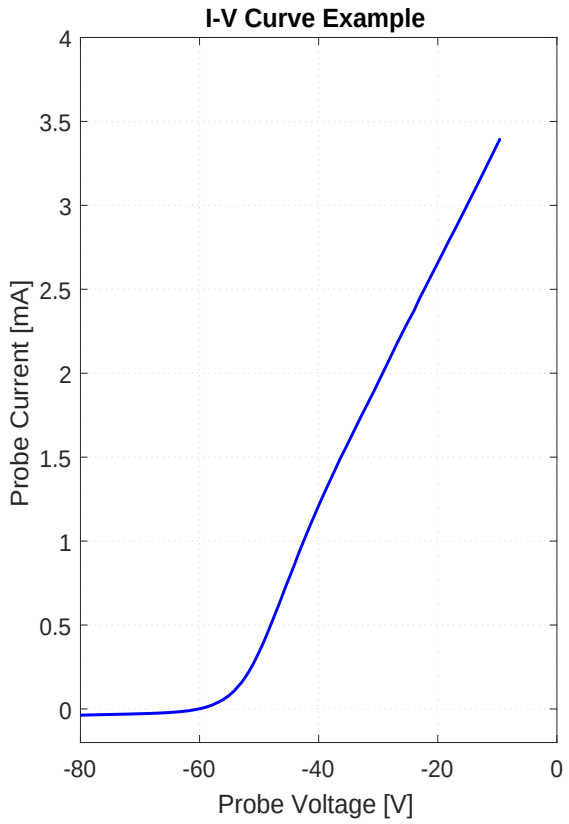

Figure 68: Example of an I-V curve.

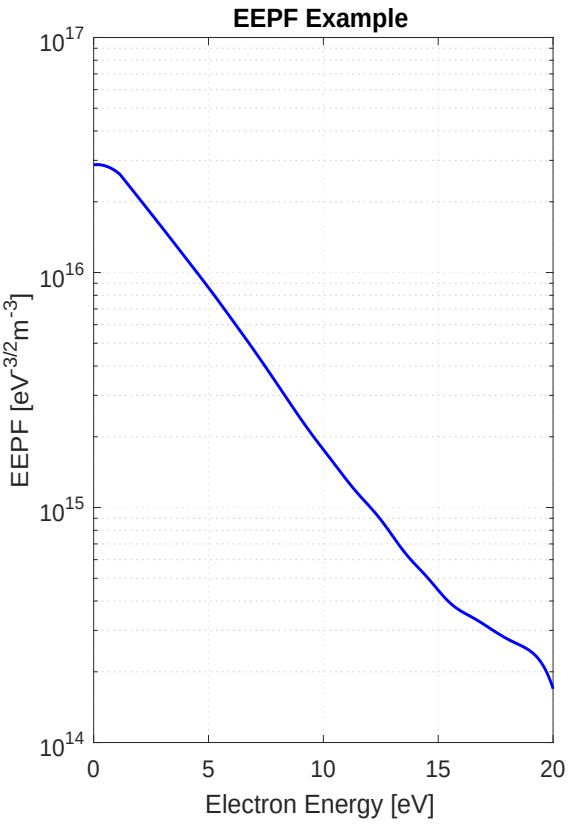

Figure 69: Example of an EEPF.

distribution functions (EEDF) are derived by the following relationship.

$$F(\epsilon) = \sqrt{\epsilon} f(\epsilon) \tag{30}$$

Then, the plasma density (n_e) and the effective electron temperature (T_{eff}), which accounts for the entire range of electron energy, can be obtained by integrating the EEDF as follows.

$$n_e = \int_0^\infty F(\epsilon) d\epsilon \tag{31}$$

$$T_{eff} = \frac{2}{3} < \epsilon >= \frac{2}{3n} \int_0^\infty \epsilon F(\epsilon) d\epsilon \tag{32}$$

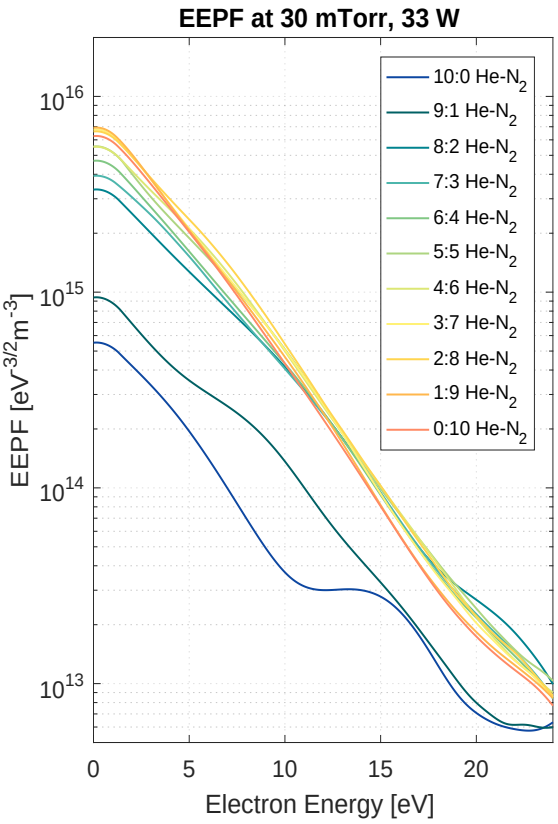

Figure 70: Measured EEPF of He-N_2 plasmas at 30 mTorr.

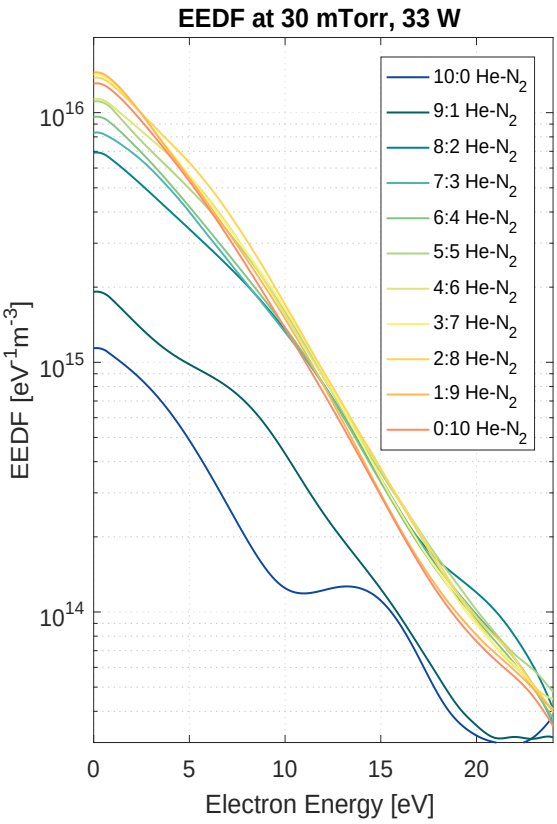

Figure 71: Measured EEDF of He-N_2 plasmas at 30 mTorr.

T_{eff} represents the overall electron temperature of a measured EEDF. T_{eff} can be calculated regardless of the shape of an EEDF. That is, an EEDF can have distinct electron temperatures in the different range of electron energy such as low T_l and high T_h electron temperatures, but T_{eff} can still be obtained. In essence, the Druyvesteyn method is powerful since it is applicable to arbitrary electron energy distribution functions as long as a collision-less probe sheath is guaranteed.

8.5 Measured He-N_2 Plasma Parameters

8.5.1 EEDF of He-N_2 Plasma

EEDF contains the most complete set of information of electrons in plasmas. As discussed in the previous section, EEDF is used for obtaining plasma parameters including electron temperature and electron density. Figure 70 shows the measured EEPF of He-N_2 plasma, which is proportional to d^2I_p/dV_p^2. Figure 71 shows the measured EEDF of He-N_2 plasmas, which is calculated from the measured EEPF. The concentration of N_2 is increased in steps of 10% and balanced with He. The overall magnitude and shape of EEDF change as N_2 concentration increases in the He-N_2 plasma.

8.5.2 Electron Temperature of He-N_2 Plasma

The electron temperatures of He-N_2 plasmas are calculated from the measured EEDF's. Figure 72 shows a decreasing trend in electron temperature as the mole fraction of N_2 increases in the He-N_2 plasma. The decreasing trend in T_e is mainly caused by the increasing number of excitation processes, which significantly dissipate electron energy. Molecular gases such as N_2 have a variety of excitation modes that can dissipate electron energy more effectively than monatomic gases that generally have fewer excitation modes. Since high energy electrons (*i.e.*, high temperature electrons) more effectively contribute in the ionization processes of gases, maintaining low electron temperature is important in achieving stronger dielectric strength. Therefore, increasing the mole fraction of N_2 in the He-N_2 gas mixture will result in higher dielectric strength.

8.5.3 Electron Density of He-N_2 Plasma

Increasing ionization processes results in increasing electron density in plasmas. Hence, electron density (*i.e.*, plasma density) may be used in assessing the dielectric strength

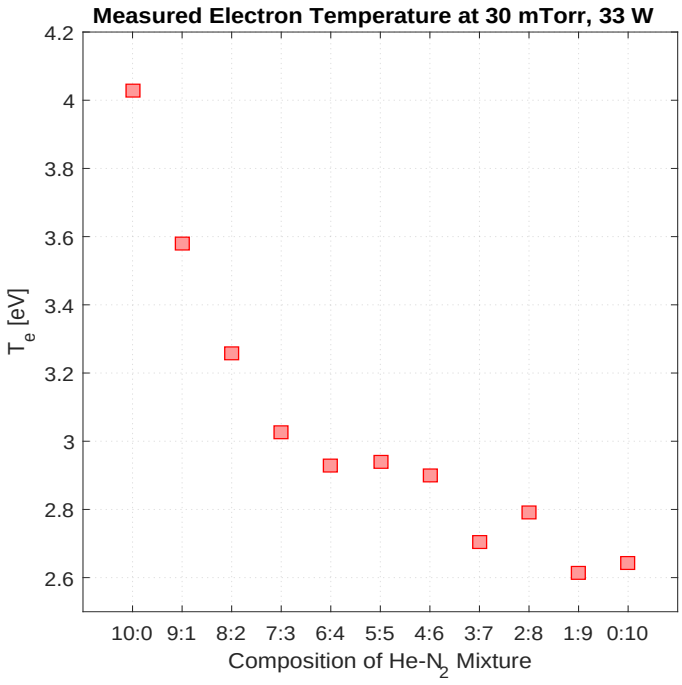

Figure 72: Measured effective electron temperature of He-N_2 plasmas.

of gases. However, correlating electron density and dielectric strength is not necessarily accurate. That is, electron density could be increasing even if the dielectric strength of a gas mixture is increasing. The electron density of a plasma chamber depends not only on the net ionization process, but also on the electron leakage at the chamber wall. Purely from electron kinetics perspective, gases with comparatively low dielectric strength will be ionized more easily and generate more free electrons, whereas gases with comparatively high dielectric strength will be less effectively ionized and generate fewer free electrons. However, in a plasma chamber, the number of free electrons (*i.e.*, electron density) is balanced by the rate of electrons leaking out through the chamber wall, which depends on the Bohm velocity (u_B) of the gas species and the effective surface area (A_{eff}) of the chamber wall.

Figure 73 shows an increasing trend in electron density as the concentration of N_2 increases in the He-N_2 plasma. The trend may seem like it is exhibiting a decreasing

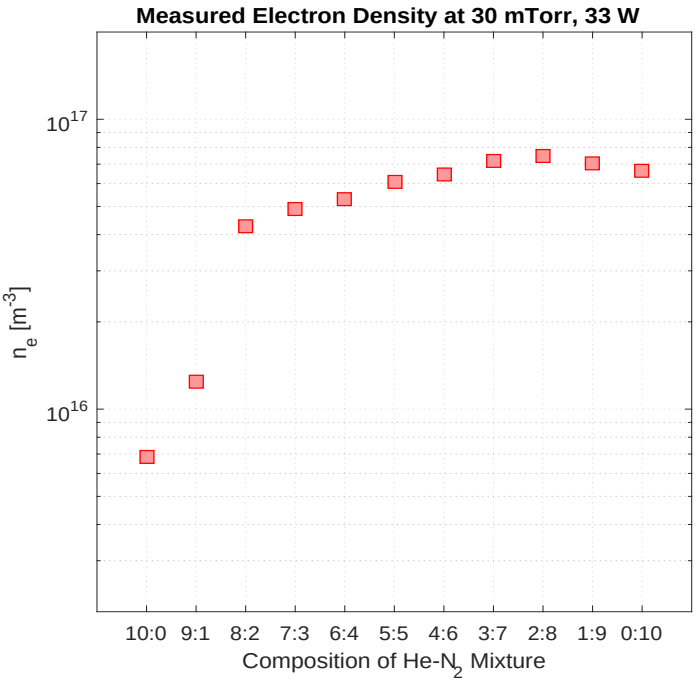

Figure 73: Measured electron density of He-N_2 plasmas.

dielectric strength as N_2 increases since higher electron density indicates higher ionization rate and lower dielectric strength. However, as discussed, it should be noted that ionization and attachment process is not the only factor that determines electron density in a plasma chamber. In confined plasmas, chamber wall is where the loss of electrons and ions occurs. Between a chamber wall and a bulk plasma, a plasma sheath exists. Depending on the sheath geometry, which depends on the mean free path of ions (λ_i), the effective chamber wall area (A_{eff}) is defined. If an effective chamber wall area is decreased due to gas mixture variation, the loss of electrons and ions would decrease and thus the plasma density would increase. Because of decreasing effective chamber wall area as N_2 is increased, the electron density of the measured bulk plasma increases as shown by Figure 73.

8.6 Estimated He-N_2 Plasma Parameters

8.6.1 Particle Balance Equation

The particle balance equation describes the temporal variation of particle density in plasmas. The equation describes the variation of electron density (*i.e.*, ion density) by balancing the ionization, attachment process, and the loss of electrons through plasma chamber wall. Assuming the quasi-neutrality of a plasma, the particle balance equation of electrons and ions is given as the following.

$$\frac{dn_e}{dt} = \sum_j \Big(K_{iz,j} n_{g,j} - K_{att,j} n_{g,j} - u_{B,j} \frac{A_{eff,j}}{V} \Big) n_e, \tag{33}$$

where $K_{iz,j}$ and $K_{att,j}$ are the rate constants of ionization and attachment of gas j, $n_{g,j}$ is the density of gas j, $u_{B,j}$ is the Bohm velocity of gas j, and $A_{eff,j}$ is the effective chamber wall area of gas j. According to this equation, electron density increases by the ionization process, but decreases by the attachment process and particle leakage at the chamber wall. The ionization and attachment process is described by rate coefficients, which are calculated by using the EEDF and the electron scattering cross sections of constituent gases as follows.

$$K_j = < \epsilon \sigma_j(\epsilon) > = \frac{1}{n} \int_0^\infty \epsilon \sigma_j(\epsilon) F(\epsilon) d\epsilon \tag{34}$$

The process of particle loss at the chamber wall depends on the Bohm velocity (u_B) and the effective area of chamber wall (A_{eff}). The Bohm velocity is given by the following equation.

$$u_B = \sqrt{\frac{eT_e}{M_i}}, \tag{35}$$

where $M_i = \sum x_k M_k$ for gas mixtures (x_k being the mole fraction of constituent gas k). Moreover, the effective chamber wall area is calculated as follows.

$$A_{eff,j} = 2\pi R^2 h_{l,j} + 2\pi R L h_{r,j}, \tag{36}$$

where R and L are the radius and length of a cylindrical chamber, h_l and h_r are the geometric correction factor, which are defined as the ratio of sheath edge plasma density to bulk plasma density.

$$h_{l,j} = \frac{n_{sl}}{n_e} \cong 0.86\Big(3 + \frac{l}{2\lambda_{i,j}}\Big)^{-1/2} \tag{37}$$

$$h_{r,j} = \frac{n_{sR}}{n_e} \cong 0.8\Big(4 + \frac{R}{\lambda_{i,j}}\Big)^{-1/2} \tag{38}$$

The correction factors h_l and h_r depend on the type of the gas of a plasma since ion mean free path is involved in the calculation, which is given as follows.

$$\lambda_{i,j} = \frac{1}{n_g \sigma_j} \tag{39}$$

By changing the He-N_2 mixture, σ_j changes. As a result, h_l, h_r, and A_{eff} change, and eventually n_e changes. Figure 74 illustrates the concept of h_l and h_r for a cylindrical plasma chamber. From the figure, one could notice why the top and bottom surface areas are multiplied by h_l, and why the side wall area is multiplied by h_r.

For negative ions, the particle balance equation involves the attachment and detachment processes as follows.

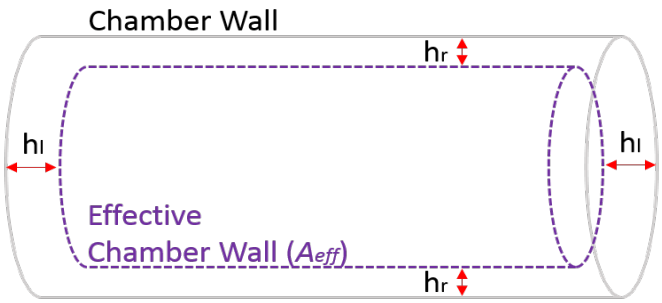

Figure 74: Effective wall area of a cylindrical chamber.

$$\frac{dn_-}{dt} = \sum_j \Big(K_{att,j} n_{g,j} - K_{det,j} n_{-,j} \Big) n_e, \tag{40}$$

where K_{det} is the rate constant of detachment, which can also be calculated by using the EEDF and the electron scattering cross sections of constituent gases. Since quasi-neutrality is maintained in plasmas, the following condition should be satisfied.

$$\sum_j n_{-j} + n_e + \sum_j n_{+j} = 0 \tag{41}$$

Electron temperature is obtained by solving the particle balance equation. Figure 75 shows the results of the calculated electron temperature using the particle balance equation. The figure shows that the electron temperature (*i.e.*, electron energy) decreases as the mole fraction of N_2 increases in the plasma. The decreasing trend is mainly due to the decreasing ionization process as the concentration of N_2 is increased in the plasma. It should be noted that the negatively charged particles are not taken into account in this chapter since He-N_2 mixtures are non-electron attaching gases.

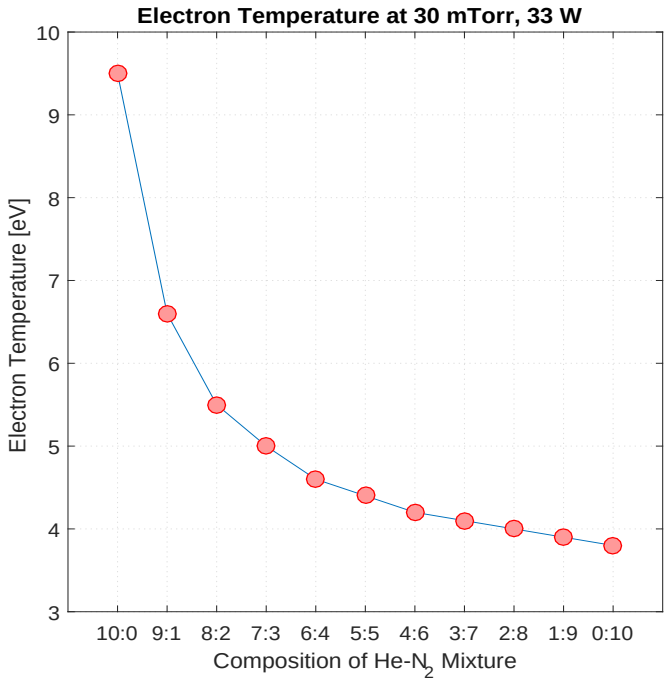

Figure 75: Estimated electron temperature of He-N_2 plasmas.

8.6.2 Power Balance Equation

The power balance equation describes the balance between input power (*i.e.*, absorbed power) and power loss.

$$P_{abs} = P_{loss} \tag{42}$$

P_{loss} consists of P_c and P_k, which are collisional loss and kinetic loss, respectively. P_c involves energy losses occurring from elastic and inelastic collisions and P_k involves energy losses occurring from electron and ion leakage at the chamber wall.

$$P_{loss} = P_c + P_k = e n_e u_B \varepsilon_{tot} \big(A_l h_r + A_r h_l \big), \tag{43}$$

where e is the elementary charge, u_B is the Bohm velocity, ε_{tot} is the total energy loss,

h_r and h_l are the area correction factors, and $A_l h_r + A_r h_l$ is the effective chamber wall area A_{eff}. The total energy loss ε_{tot} consists of kinetic energy loss and collisional energy loss.

$$\varepsilon_{tot} = \varepsilon_k + \varepsilon_c, \tag{44}$$

where ε_k is the kinetic energy loss and ε_c is the collisional energy loss. Kinetic energy loss ε_k occurs when ions or electrons escape from the plasma chamber. Ions and electrons mainly escape through plasma sheath near the chamber wall. Hence, kinetic energy loss consists of ionic energy loss ε_i and electronic energy loss ε_e.

$$\varepsilon_k = \varepsilon_i + \varepsilon_e \tag{45}$$

Ionic energy loss ε_i is given by the following equation, which is the sum of ion energy entering a sheath and energy gained by ion as it accelerates across the sheath.

$$\varepsilon_i = \left[\frac{1}{2}\ln\Big(\frac{M_i}{2\pi m}\Big) + \frac{1}{2}\right] T_e \tag{46}$$

Electronic energy loss ε_e is given by the following equation,

$$\varepsilon_e = 2T_e \tag{47}$$

Furthermore, the collisional energy loss ε_c is derived from the energy loss involved in an electron-ion pair generation, which is given by the following equation.

$$\varepsilon_c \sum_j K_{iz,j} n_{g,j} = T_e \sum_j \frac{3m}{M_j} K_{m,j} n_{g,j} + \sum_j \sum_k \varepsilon_{ex,k} K_{ex,j,k} n_{g,j} + \varepsilon_{iz} \sum_j K_{iz,j} n_{g,j} \tag{48}$$

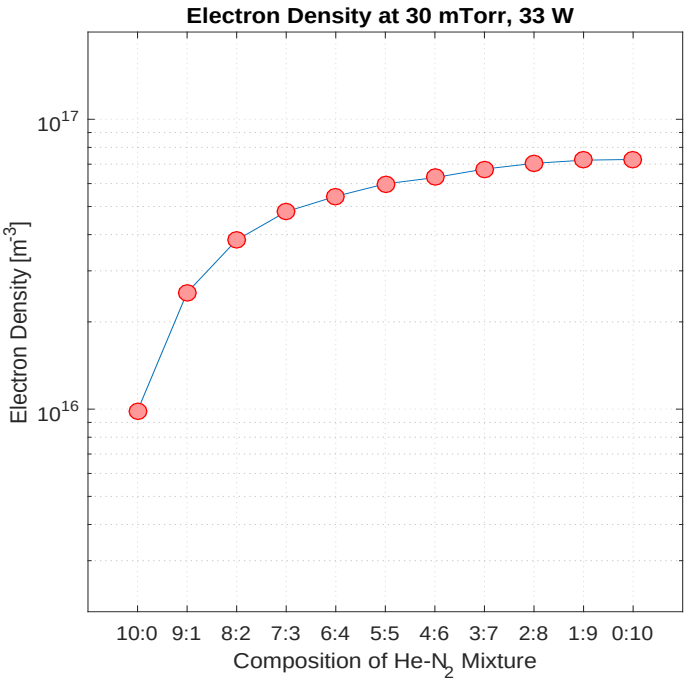

Figure 76: Estimated electron density of He-N_2 plasmas.

The right hand side of the equation describes the total energy loss of all collisions that occurred until a neutral particle is ionized. By rearranging the terms on the left, the collisional energy loss ε_c is obtained as follows.

$$\varepsilon_c = \left(T_e \sum_j \frac{3m}{M_j} K_{m,j} n_{g,j} + \sum_j \sum_k \varepsilon_{ex,k} K_{ex,j,k} n_{g,j} + \varepsilon_{iz} \sum_j K_{iz,j} n_{g,j} \right) / \sum_j K_{iz,j} n_{g,j} \tag{49}$$

With the knowledge of Bohm velocity u_B, total energy loss ϵ_{tot}, and effective chamber wall area A_{eff}, electron density (*i.e.*, plasma density) n_e is derived by solving the power balance equation.

$$n_e = \frac{P_{abs}}{e u_B \varepsilon_{tot} A_{eff}} \tag{50}$$

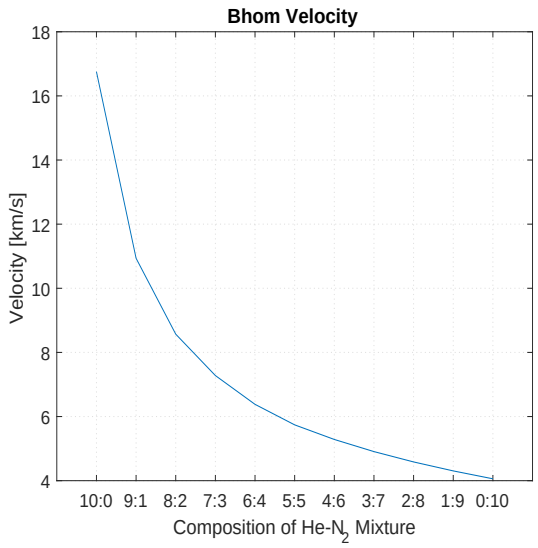

Figure 77: Bohm velocity of He-N_2 plasmas.

According to the equation, electron density n_e in a plasma is inversely proportional to the Bohm velocity u_B, total energy loss ε_{tot}, and effective chamber wall area A_{eff}, but proportional to input power P_{abs}. Figure 76 shows the values of n_e calculated from the power balance equation. As shown in the figure, n_e in creases as N_2 increases in the He-N_2 plasma. The increasing trend in n_e agrees well with the increasing trend of the measured n_e presented in Figure 73.

It is important to discuss why plasma density n_e increases as N_2 increases in the He-N_2 plasma. There are several contributing factors for the increasing trend. Figure 77 shows the decreasing trend in the Bohm velocity as N_2 increases in the He-N_2 plasma. The decreasing trend is mainly due to decreasing electron temperature and increasing ion mass M_i. Hence, as N_2 content accounts for a larger portion in the He-N_2 gas mixtures, the overall mass of ions increases, which decreases u_B. The reduction in u_B is one of the contributing factors that increases plasma density in the plasma chamber. Figure 78 shows the decreasing trend in the ionic loss as N_2 increases in the He-N_2 plasma, which is mainly due to decreasing electron temperature (Figure 75). Similarly, Figure 79 shows the decreasing trend in the electronic loss as N_2 increases

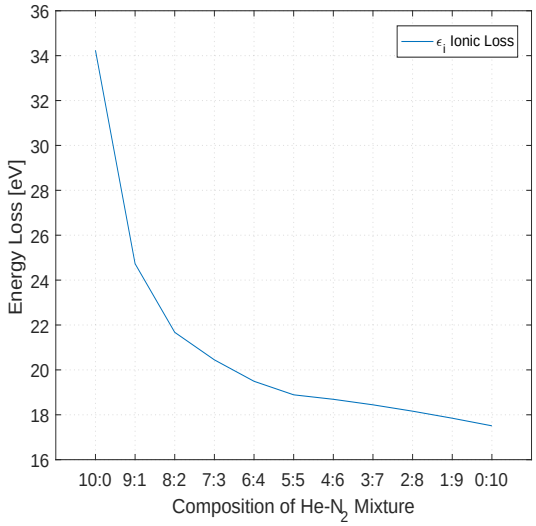

Figure 78: Ionic loss in He-N_2 plasmas.

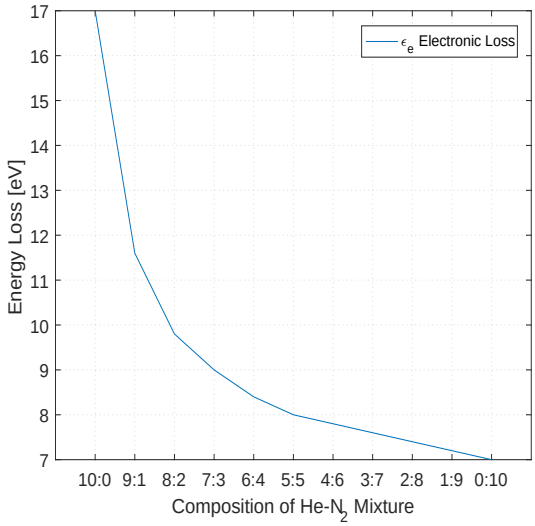

Figure 79: Electronic loss in He-N_2 plasmas.

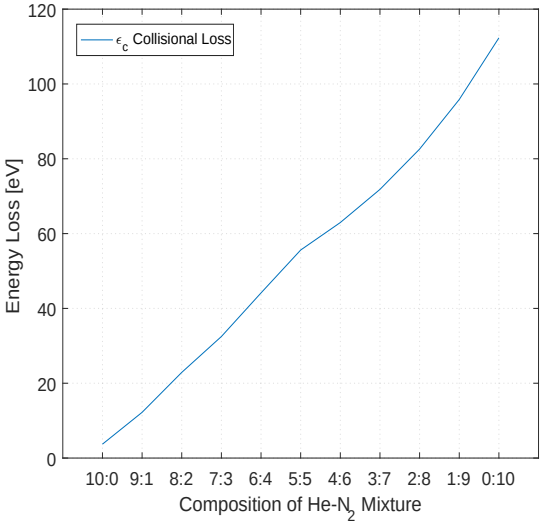

Figure 80: Collisional loss in He-N_2 plasmas.

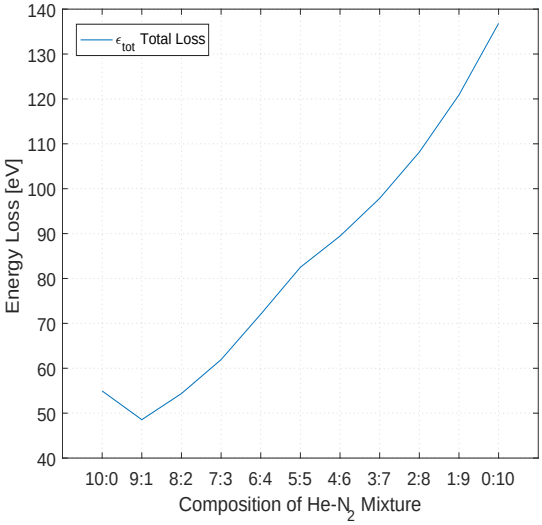

Figure 81: Total loss in He-N_2 plasmas.

in the He-N_2 plasma, which is also mainly due to decreasing electron temperature (Figure 75). Note that the decreasing electron temperature was calculated from the particle balance equation in Section 8.6.1. Figure 80 shows the increasing trend of collisional loss as N_2 increases in the He-N_2 plasma, which is mainly due to increasing excitation electron scattering process. The increasing energy loss caused by excitation collisions outweigh the decreasing kinetic energy loss, which leads to the increase of

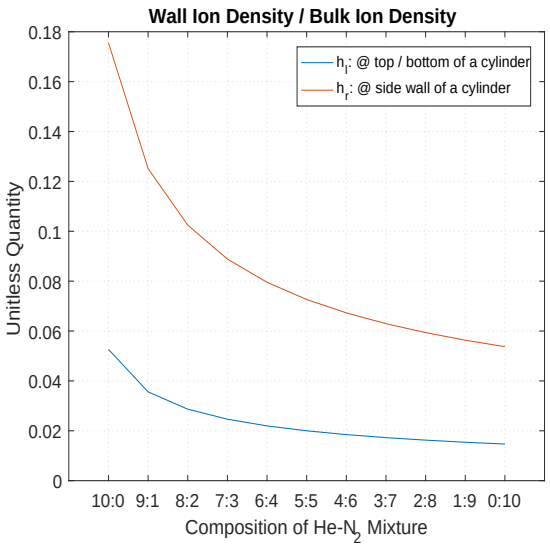

Figure 82: Variation in the area correction factors of He-N_2 plasmas.

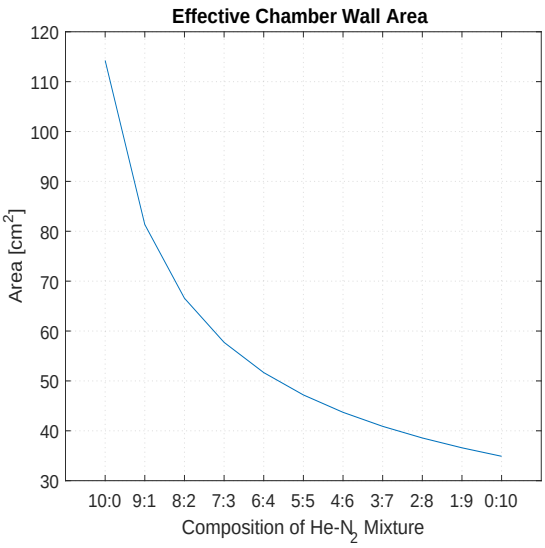

Figure 83: Variation in the effective area of He-N_2 plasmas.

the total energy loss as presented in Figure 81. As discussed in Section 8.6.1, h_r and h_l are defined as the ratio of ion density at the chamber wall to the bulk plasma. This ratio determines the effective surface area of a bulk plasma, through which ions and electrons escape. As Figure 82 clearly shows, both h_r and h_l decreases as N_2 increases in the He-N_2 plasma. The reduction in both h_r and h_l is mainly due to the reduction of the mean free path of ions as N_2 content increases. As a result, effective chamber wall area A_{eff} decreases as the concentration of N_2 increases as shown in Figure 83. Due to the decrease in both Bohm velocity u_B and effective chamber wall area A_{eff}, plasma density n_e increases as N_2 increases in the He-N_2 plasma.

8.7 Discussion

The decreasing trend of T_e as N_2 increases in the He-N_2 mixture can be interpreted as the increasing dielectric strength of the gas mixture. The interpretation is suitable because particle loss through the chamber wall does not play a significant role in determining T_e. However, the varying trend of n_e may not be suitable for dielectric strength evaluation since the chamber wall significantly influences the values of n_e.

If processes at plasma chamber wall does not alter n_e, and if n_e depends only on the electron kinetics of gas mixtures, the increasing or decreasing trend of n_e may be suitable as the means of evaluating the dielectric performance of a gas mixture. However, all confined plasmas interact with its chamber wall and thus n_e is not just dependent on electron kinetic processes. Therefore, the study recommends the use of T_e for comparing the dielectric strength of gas mixtures.

8.8 Summary

This chapter utilized a plasma diagnostics method for investigating the dielectric strength variation of He-N_2 gas mixtures. The results showed a decreasing trend in electron temperature and an increasing trend in electron density as N_2 increased in the He-N_2 plasma. The increasing electron density was mainly caused by the reduction of the effective chamber wall area when the concentration of N_2 increased. The reduction in the wall area impeded the leakage of electrons from the plasma, which increased the plasma density. The study discussed that plasma density is not solely dependent on the electron kinetics of gas mixtures and thus not a suitable parameter for assessing the dielectric strength of gases. On the other hand, the study discussed that electron temperature is suitable for the dielectric strength evaluation of gases due to its negligible dependence on the chamber wall area. The decreasing trend of electron temperature is the indication of dielectric improvement, which was also discussed in Chapters 4-7.

CHAPTER IX

CONCLUSION

This dissertation is focused on understanding the dielectric properties of gas mixtures for cryogenic power applications through modeling and experimental investigations with the goal of identifying specific mixtures that would be suitable for increasing the voltage ratings of HTS power devices cooled with gaseous cryogens.

To understand and improve the dielectric breakdown properties of gases, the dissertation presented the analysis on the electron kinetics of various potential cryogenic gas mixtures. The results showed that molecular gases generally show stronger dielectric strength than noble gases, which are monatomic. The superior dielectric strength of molecular gases is mainly due to the existence of numerous excitation modes in them. The study also included the mapping of the useful compositions of the gas mixtures for a given temperature and pressure range that prevents possible condensation. The maximum allowed concentration of molecular gases determined the maximum-achievable dielectric strength of gas mixtures, which changed as a function of the cryogenic operating temperature and pressure.

To quantitatively predict the dielectric strength of gases and gas mixtures, a new modeling procedure that uses a versatile formula for the ionization coefficient in its regression process was developed. The new modeling procedure enhanced the accuracy of the dielectric strength prediction of pure gases as well as gas mixtures. Unlike the conventional dielectric strength models, the versatility of the proposed formula enabled the new dielectric model to track the dielectric strength variation as the composition of the gas mixture is changed. The capability of the developed model has been validated by comparing its predictions with the experimental breakdown

measurements at room temperature and cryogenic temperature at a pressure range up to 2 MPa.

The dissertation also involved designing and utilizing plasma experiments for measuring plasma parameters used for evaluating the dielectric properties of the cryogenic gas mixtures. The measurements of the confined low-temperature plasmas did not behave as expected by showing increasing electron density as the nitrogen concentration increased in the helium-nitrogen plasma. The reason for the increase was explained by using the global model, which consists of particle balance equation and power balance equation, of the helium-hydrogen plasmas. The results of the global model showed a decrease in electron leakage at the chamber wall as nitrogen concentration increased in the plasma. The results of the plasma experiment suggested the use of electron temperature, but not electron density for evaluating the dielectric strength of gases.

CHAPTER X

FUTURE WORK

10.1 Versatile Model for Ternary Gas Mixtures

The proposed modeling procedure was discussed in Chapter 7. The performance of the versatile model was confirmed with the dielectric strength of He-H_2 gas mixtures. Although the present study validated the model's capability only with the He-H_2 gas mixtures, its accuracy is likely to be suitable for modeling other potential cryogenic gas mixtures. Therefore, it would be interesting to see the proposed modeling procedure being applied to He-N_2 and He-H_2-N_2 mixtures, both of which are promising gaseous cryogen candidates for HTS applications.

10.2 RF Plasma Parameter Measurement

In this dissertation, DC plasma parameters were measured to study the dielectric strength of gas mixtures. The main reason for using the DC plasma discharge was that the DC plasmas are sustained by the secondary electron emission process, which plays a significant role in most gas dielectric breakdown. Although this method served well for this study, room for improvements exists.

Electrostatic probe measurements are based on the assumption that probe sheath is collision-less. Collisionless condition requires low gas pressure and the use of simple gases during measurements. The issue is that DC plasmas are created based on Paschen's law, so decreasing the gas pressure may require exceedingly high voltages to maintain the discharge. Moreover, since different gases follows distinct Paschen's law, significantly high voltage range could be required to sustain a DC plasma depending on the subject gas. As discussed, using DC plasmas for studying small and simple

gases such as He and N_2 suffices the collision-less probe sheath condition at gas pressures on the range of tens of mTorr. However, studying heavier and more complex gases such as NOVEC 4710 or SF_6 would require lower gas pressure. Under such low pressure conditions, radio frequency (RF) plasmas are suitable since their discharge can be generally sustained at lower pressures than DC plasmas. However, the benefits come with a price. RF plasmas fluctuates in potential according to the RF power source. Hence, RF filters are required in the electrostatic probes. Also, to control the input discharge power, a matching network must be connected to the output of the RF power source. Moreover, since RF plasmas are not driven by an electric field formed between an anode and cathode, its plasma potential is positive with respect to the chamber wall. This indicates that a fully operating four-quadrant power supply is necessary for sweeping the probe voltage from negative to positive.

CHAPTER XI

LIST OF PUBLICATIONS

Journal Papers

J1. **C. Park**, S. Pamidi, and L. Graber, "Evaluating the Dielectric Strength of Helium-Nitrogen Gas Mixtures by Plasma Parameter Measurements", Physics of Plasmas, 2017 **(Submitted)**

J2. **C. Park**, S. Pamidi, and L. Graber, "The Critical Electric Field of Gas Mixtures Over the Extended Range of Cryogenic Operating Conditions", Journal of Applied Physics, vol. 122, no. 15, pp. 153301, 2017 **(Published)**

J3. **C. Park**, L. Graber, P. Cheetham, J. Viquez, C. H. Kim, and S. Pamidi, "A Versatile Modeling Technique for Predicting Dielectric Strength Improvements in Gas Mixtures for Superconducting Applications", IEEE Transactions on Dielectrics and Electrical Insulation, vol. 24, no. 5, pp. 2755-2764, Oct. 2017 **(Published)**

J4. **C. Park**, S. Pamidi, and L. Graber, "The Dielectric Properties of Gaseous Cryogen Mixtures of He, H2, Ne, and N2 in a Temperature Range of 50-80 K at Pressures up to 2.0 MPa", Journal of Applied Physics, vol. 121, no. 8, pp. 083304, 2017 **(Published)**

J5. **C. Park**, S. Pamidi, and L. Graber, "Boltzmann Analysis of Cryogenic He-H2 Gas Mixtures as Dielectric Media for High-Temperature Superconducting Power Devices", IEEE Transactions on Applied Superconductivity, vol. 27, no. 4, pp. 1-6, June 2017 **(Published)**

Conference Papers

C1. P. Cheetham, **C. Park**, C. Kim, L. Graber, and S. Pamidi, "Experimental Studies on the Cryogenic Dielectric Properties of Gas Mixtures for Superconducting Power Applications", IOP Conference Series: Materials Science and Engineering, vol. 278, no. 1, pp. 012040, 2017 **(Published)**

C2. **C. Park**, S. Pamidi, and L. Graber, "Application of the Langmuir Probe Plasma Diagnostics into the Investigation of the Dielectric Properties of Cryogenic Gas Mixtures", IOP Conference Series: Materials Science and Engineering, vol. 278, no. 1, pp. 012039, 2017 **(Published)**

C3. Lukas Graber, Maryam Saeedifard, Mickael J. Mauger, Qichen Yang, **Chanyeop Park**, Tobias Niebur, Sastry V. Pamidi, Stefan Steinhoff, "Cryogenic Power Electronics for Superconducting Power Systems", IOP Conference Series: Materials Science and Engineering, vol. 279, no. 1, pp. 012011, 2017 **(Published)**

C4. **C. Park**, L. Graber, W. Kim, P. Cheetham, C. Kim, S. Pamidi, and H. Rodrigo, "A versatile model for estimating breakdown voltage and its application for cryogenic gas mixtures", 2016 IEEE Conference on Electrical Insulation and Dielectric Phenomena (CEIDP), Toronto, ON, 2016, pp. 542-545 **(Published)**

APPENDIX A

THEORETICAL FRAMEWORK

A.1 Boltzmann Analysis

A.1.1 Two-term Approximation

The work presented in this dissertation uses the two-term approximation of the Boltzmann equation to obtain the electron distribution function, which is required for calculating the coefficient of electron kinetics. This section explains how the two-term approximation simplifies the Boltzmann equation.

Electron distribution function f is a probability density function of six-spatial dimensions in position, velocity, and one temporal dimension: $f(x, y, z, \upsilon_x, \upsilon_y, \upsilon_z, t)$, which describes the electron ensemble. By taking the total time derivative df/dt, the Boltzmann equation is expanded as shown below.

$$\frac{\partial f}{\partial t} + \upsilon \cdot \nabla f - \frac{e}{m} E \cdot \nabla_{\mathrm{v}} f = C[f], \tag{51}$$

υ is the velocity vector, ∇ is the gradient in the position space, e is the elementary charge, m is the electron mass, E is the electric field, ∇_{v} is the gradient in the velocity space, and $C[f]$ is the collision term that represents the rate of change in f. Note that eE/m is the acceleration term.

Solving the Boltzmann equation is exceedingly difficult for gas discharges since the fields and inter-particle collisions that appear in the equation must be determined self-consistently for each species. Hence, we drastically simplify the Boltzmann equation as follows. Initially, a spatially uniform electric field and collision probability is assumed, which indicates that f is symmetric around the electric field in velocity

space and that f may vary along the electric field in position space (*i.e.*, cylindrically symmetric along the direction of anisotropy). Then, we apply spherical coordinates in velocity space, in which the z direction is the electric field direction, θ is the angle between velocity and the field direction, and υ is the magnitude of the velocity.

$$\frac{\partial f}{\partial t} + \upsilon \cos\theta \frac{\partial f}{\partial z} - \frac{e}{m} E \Big(\cos\theta \frac{\partial f}{\partial \upsilon} + \frac{\sin^2\theta}{\upsilon} \frac{\partial f}{\partial \cos\theta} \Big), \tag{52}$$

Note that the first two process reduces the dimensions of f into $f(z, \upsilon, \theta, t)$ because the assumptions removed the dependence of f on x, y, and ϕ. We continue by assuming a steady state condition to get rid of the t dependence of f, and to further simplify the θ dependence, we use the two-term approximation method. The two-term approximation expands f to first order in the deviation from isotropy (*i.e.*, expand in terms of Legendre polynomials of $\cos\theta$, also known as spherical harmonic expansion) as follows.

$$f(\upsilon, \cos\theta, z, t) = f_0(\upsilon, z, t) + f_1(\upsilon, z, t) \cos\theta, \tag{53}$$

where f_0 is the isotropic part of the electron distribution and f_1 is the anisotropic part of it. By substituting (53) into (52), multiplying the respective Legendre polynomials (*i.e.*, 1 and $\cos\theta$), and integrating over 0 to π results in the following equations.

$$\frac{\partial f_0}{\partial t} + \frac{\gamma}{3} \epsilon^{1/2} \frac{\partial f_1}{\partial z} - \frac{\gamma}{3} \epsilon^{-1/2} \frac{\partial}{\partial \epsilon} (\epsilon E f_1) = C_0, \tag{54}$$

$$\frac{\partial f_1}{\partial t} + \gamma \epsilon^{1/2} \frac{\partial f_0}{\partial z} - E \gamma \epsilon^{1/2} \frac{\partial f_0}{\partial \epsilon} = -N \sigma_m \gamma \epsilon^{1/2} f_1, \tag{55}$$

where $\gamma = (2e/m)^{1/2}$ is a constant and $\epsilon = (\upsilon/\gamma)^2$ is electron energy in electron volts.

Note that (54) is obtained by multiplying 1 (time variation of the isotropic part of the electron distribution), (55) is obtained by multiplying $\cos\theta$ (time variation of the anisotropic part of the electron distribution), and that θ no longer exists. Further simplifications on $\partial f/\partial z$ and $\partial f/\partial t$ of (54) and (55) are handled by substituting the electron growth model

$$\alpha = -\frac{1}{n}\frac{n}{z} \tag{56}$$

into (54) and (55). After this simplification process, the Boltzmann equation becomes a convection-diffusion equation in one dimensional energy space.

$$\frac{\partial}{\partial\epsilon}\left(\tilde{W}F_0 - \tilde{D}\frac{\partial F_0}{\partial\epsilon}\right) = \tilde{S}, \tag{57}$$

where

$$\tilde{W} = -\gamma\epsilon^2\sigma_\epsilon - 3a\frac{n}{N}A_1, \tag{58}$$

$$\tilde{D} = \frac{\gamma}{3}\left(\frac{E}{N}\right)^2\frac{\epsilon}{\tilde{\sigma}_m} + \frac{\gamma k_B T}{e}\epsilon^2\sigma_\epsilon + 2a\frac{n}{N}(A_2 + \epsilon^{3/2}A_3), \tag{59}$$

$$\sigma_\epsilon = \sum_{k=elastic}\frac{2m}{M_k}x_k\sigma_k, \tag{60}$$

$$\tilde{S} = \sum_{k=inelastic}\tilde{C}_{0,k} \tag{61}$$

Note that this section only contains the basic principles and respective derivation of the two-term approximation method. For full details readers are recommended to refer to the publications by Hagelaar *et al.* [37, 38].

A.1.2 Computation Method

The Boltzmann equation with the two-term approximation is numerically solved by the BOLSIG+ software, which is used in the 'Boltzmann Equation Two-Term Approximation Interface' in the Plasma Module of COMSOL Multiphysics 5.2, to obtain the coefficients of electron kinetics [3, 4]. We assume that dissociated gas species do not exist because the studied temperature is low (*i.e.*, cryogenic), all neutral particles are in their ground states, and the energy of an incident electron and a new electron generated from an ionization collision is equally shared. It should be noted that the assumptions of BOLSIG+ do not apply to non-local electron kinetics [38]. Hence, the results should not be taken directly for describing real plasmas that involve boundaries and field variations, which influence electron kinetics via non-local processes. Yet, BOLSIG+ provides electron kinetics data with practical generalization, better than those assuming Maxwellian EEDF.

For a nearly isotropic f, elastic collision process should be dominant compared to the gained energy from electric field and the lost energy from inelastic collisions. For this reason, it has been reported that the two-term approximation method is less reliable at high E/N, in which the inelastic collision process is dominant and the electron distribution is highly anisotropic [14, 38, 56]. The Boltzmann analysis of the present study involves gas species that have large elastic momentum-transfer electron scattering cross sections and E/N as high as 120 Td (1 Td = 10^{-21} Vm^2). Also, because of the weak electron attaching nature of the gas species of the study, $(E/N)_{cr}$ values are lower than 45 Td, which makes the two term approximation valid,

but in gas mixture containing strong electron attaching gases such as SF_6, $(E/N)_{cr}$ exist in the range of 350-450 Td [54, 55, 94].

A.2 Plasma Physics

A.2.1 Electron Temperature

In plasma physics, the energy of electrons is often represented in terms of temperature. Electrons with high energy is referred to as hot electrons and cold electrons for those with low energy. The correlation between the energy and temperature is derived by defining the pressure of a gas. Pressure is caused by changes in momentum of particles colliding into the wall of a given space, where change of momentum is given as

$$\Delta p = |mu_x - (-mu_x)| = 2mu_x \text{ [kgm/s]} \tag{62}$$

The time that it takes until a particle collides with the same wall again in the x-axis direction after bouncing off from the other side of the wall is

$$\Delta t = \frac{2l}{u_x} \text{ [s]} \tag{63}$$

Hence, the force applied to the wall is

$$F = \frac{\Delta p}{\Delta t} = \frac{mu_x^2}{l} \text{ [N]} \tag{64}$$

Pressure, which is the applied force on a surface area, is derived as

$$P = \frac{F}{l^2} = \frac{mu_x^2}{l^3} = \frac{mu_x^2}{V} \text{ [N/m}^2\text{]} \tag{65}$$

Note that the equation above represents the pressure generated by a single particle. If N is the total number of particles in a given space, the overall pressure is derived as

$$P = \frac{Nmu_x^2}{V} \text{ [N/m}^2\text{]} \tag{66}$$

Generalizing u_x into u in 3D space requires the following equation.

$$u^2 = u_x^2 + u_y^2 + u_z^2 \tag{67}$$

Assuming an isotropic velocity distribution, that is, $< u_x^2 >=< u_y^2 >=< u_z^2 >$, the average velocity in 3D space becomes

$$< u^2 >= 3 < u_x^2 > \tag{68}$$

Therefore, pressure in 3D space becomes

$$P = \frac{Nm < u^2 >}{3V} \text{ [N/m}^2\text{]} \tag{69}$$

According to the ideal gas law $PV = NkT$, where k is the Boltzmann constant, and N is the number of particles,

$$PV = \frac{Nm < u^2 >}{3} = NkT \text{ [Nm]} \tag{70}$$

Hence,

$$\frac{1}{2}m < u^2 >= \frac{3}{2}kT \text{ [Nm]} \tag{71}$$

According to the equation above, the velocity of an electron can be estimated by measuring the temperature of it.

A.2.2 Collision Frequency

Given that the radius of a neutral particle is R, a neutral-neutral collision would occur when the distance between the center of two neutrals is less than $2R$. This is equivalent to having a neutral with a radius of $2R$ colliding with a particle that has no size such as electrons. The volume covered by the neutral moving in velocity u for time t is

$$V = \pi(2R)^2 ut \tag{72}$$

Given that the number density is n [m^{-3}], the total number of collisions over time t would be

$$nV = n\pi(2R)^2 ut \tag{73}$$

Hence, collision frequency, which is the number of collisions per unit time, is

$$\nu = n\pi(2R)^2 u = \sigma nu \text{ [Hz]} \tag{74}$$

where σ is the collision cross section. The same approach applies for collisions between electrons and neutrals. The only difference in the case of electron-neutral collisions is that the radius is R instead of $2R$ because the radius of electrons is negligible.

A.2.3 Mean Free Path

Mean free path λ is defined as the average distance a particle can travel without a collision. Using the collision frequency, the mean free path is given as

$$\lambda = \frac{u}{\nu} = \frac{1}{\sigma n} \tag{75}$$

Note that cross sections are functions of u or ϵ, so λ is also a function of electron energy. If a plasma chamber is smaller than the mean free path of electrons λ_e, electron-neutral collisions are less likely to occur, so it would be difficult for a plasma to be sustained as collisions that are required to generate and sustain a plasma are fewer than the electrons leaking out through the chamber wall.

A.2.4 Boltzmann Relation

In a confined plasma chamber, drift velocity u_d is negligible. Hence the fluid equation is given as

$$\begin{gathered} -eE - \nabla n_e \frac{kT}{n_e} = 0, \\ \nabla n_e = -\frac{n_e e E}{kT} \end{gathered} \tag{76}$$

Since $E = -\nabla V$,

$$\nabla n_e = \frac{n_e e}{kT} \nabla V \tag{77}$$

Assuming R^1 space,

$$\frac{dn_e}{dx} = \frac{n_e e}{kT}\frac{dV}{dx},$$
$$\frac{1}{n_e}dn_e = \frac{e}{kT}dV \tag{78}$$

Integrating both sides gives

$$\int_{n_1}^{n_2} \frac{1}{n_e}dn_e = \int_{V1}^{V2} \frac{e}{kT}dV,$$
$$\ln\left(\frac{n_2}{n_1}\right) = \frac{e}{kT}(V_2 - V_1) \tag{79}$$

Exponentiating both sides gives

$$n_2 = n_1 e^{\frac{e}{kT}(V_2 - V_1)} \tag{80}$$

This equation can be simplified further by utilizing the fact that kT is interchangeable with eT. The only difference between the two is that T has a unit of [K] for kT, whereas, [V] for eT.

$$n_2 = n_1 e^{\frac{V_2 - V_1}{T}} \tag{81}$$

The Boltzmann relation shows that the electron density depends on the plasma potential and vice versa. Potential increases as electron density increases. This is useful in determining the plasma potential relative to the plasma chamber wall potential.

A.2.5 Plasma Sheath

In a quasi-neutral plasma, light and mobile electrons reaches the wall more quickly than ions. Due to this phenomenon, ion density is higher than the electron density in

the vicinity of the chamber wall (*i.e.*, quasi-neutrality is broken). The region where quasi-neutral is not satisfied near the chamber wall is called plasma sheath. According to the Boltzmann relation, decreasing electron density leads to decreasing potential. Hence, the plasma potential is higher than the wall potential. In this section, the following conditions are assumed. It is assumed that electron distribution is Maxwellian, ions are cold ($T_i = 0$) in the plasma, quasi-neutrality is maintained in the plasma and up to the sheath edge, and potential is zero at the sheath edge (between pre-sheath and sheath). Based on these assumptions, electron density will vary according to the Boltzmann relation, and ions will obey the conservation of energy. At the sheath edge, if the ion velocity is u_{is}, the energy conservation gives

$$\frac{1}{2}M_i u_{is}^2 = \frac{1}{2}M_i u(x)^2 + e\Phi(x), \tag{82}$$

where $u(x)$ is the ion velocity and $\Phi(x)$ is the potential in the sheath. LHS of the equation in fact assumes that ions are cold, however, they are arrived at the sheath edge with a velocity of u_{is}. The continuity of ion flux assuming no collision in the sheath gives

$$n_{is}u_{is} = n_i(x)u(x), \tag{83}$$

where n_{is} is the ion density at the sheath edge. Solving the equation in terms of $n_i(x)$ gives

$$n_i(x) = n_{is}\left(1 - \frac{2e\Phi(x)}{M_i u_{is}^2}\right)^{-1/2} \tag{84}$$

Electron density is given by the Boltzmann relation

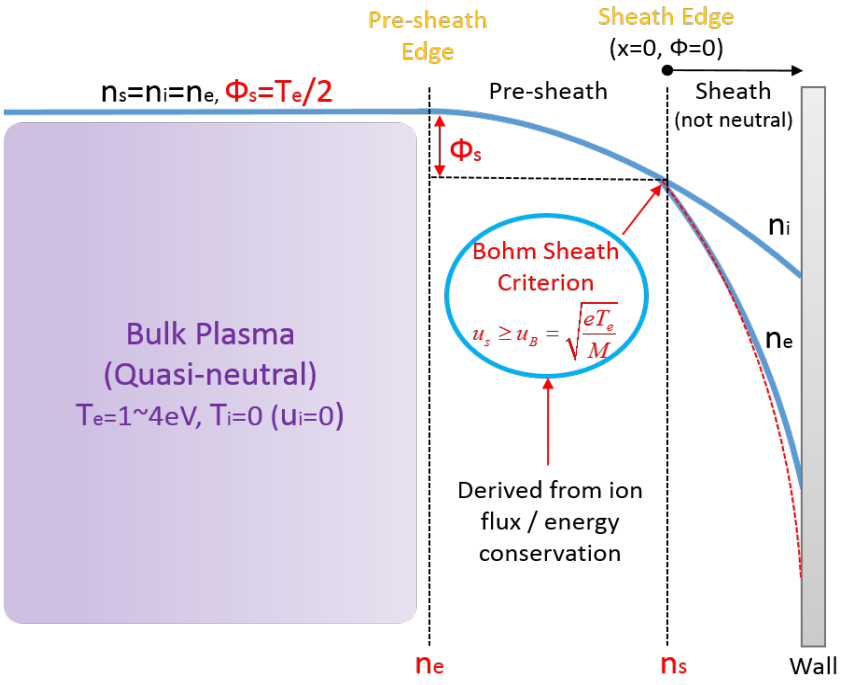

Figure 84: Depiction of a collisionless plasma sheath and pre-sheath.

$$n_e(x) = n_{es} e^{\frac{\Phi(x)}{T_e}}, \tag{85}$$

where n_{es} is the density of electrons at the sheath edge, $\Phi(x)$ is the potential with respect to the zero potential at the sheath edge. Transforming $n_i(x)$ into

$$n_i(x) = n_{is}\left(1 - \frac{e\Phi(x)}{\frac{1}{2}M_i u_{is}^2}\right)^{-1/2} \tag{86}$$

shows that $\frac{e\Phi(x)}{\frac{1}{2}M_i u_{is}^2} < 1$ because the potential near the sheath edge is close to zero. Applying Taylor series gives

$$n_i(x) = n_{is}\left(1 + \frac{e\Phi(x)}{M_i u_{is}^2} + ...\right) \tag{87}$$

Also applying Taylor series for $n_e(x)$ gives

$$n_e(x) = n_{es}\left(1 + \frac{\Phi(x)}{T_e} + ...\right) \tag{88}$$

Since electron density is lower than that of the ion density and $n_{is} = n_{es} = n_s$, the following condition should be satisfied.

$$\frac{\Phi(x)}{T_e} \leq \frac{e\Phi}{M_i u_s^2} \tag{89}$$

Solving this for u_{is} gives

$$u_{is} \geq \left(\frac{eT_e}{M_i}\right)^{1/2} = u_B, \tag{90}$$

where u_B is called the Bohm velocity. This indicates that the velocity at the sheath edge is not zero, although cold ion was assumed in the bulk plasma. To explain how ions would accelerate to Bohm velocity, pre-sheath is introduced. In the quasi-neutral pre-sheath, cold ion is accelerated due to the potential difference between the plasma (Φ_s) and the sheath edge ($\Phi = 0$). Therefore,

$$\frac{1}{2} M_i u_B^2 = e\Phi_s \tag{91}$$

Substituting (90) and solving for Φ_s gives

$$\Phi_s = \frac{T_e}{2} \tag{92}$$

Electron flux is given as

$$\Gamma_e = \frac{1}{4} n_e < v > \tag{93}$$

Then the electron flux at the chamber wall would be

$$\Gamma_{ew} = \frac{1}{4} n_e < v > e^{\frac{\Phi_w}{T_e}}, \tag{94}$$

where Φ_w is the potential of the wall with respect to the sheath edge potential ($\Phi = 0$). Assuming a constant ion flux through the sheath gives the following relationship.

$$\Gamma_{is} = n_{is} u_B \tag{95}$$

Since, $\Gamma_{is} = \Gamma_{ew}$ should be satisfied at the chamber wall,

$$n_{is} \Big(\frac{eT_e}{M_i} \Big)^{1/2} = \frac{1}{4} n_e \sqrt{\frac{8kT}{\pi m_e}} e^{\frac{\Phi_w}{T_e}} \tag{96}$$

Solving the above for Φ_w gives

$$\Phi_w = -T_e \ln \Big(\frac{M_i}{2\pi m_e} \Big)^{1/2} \tag{97}$$

As discussed, the wall potential is negative with respect to the sheath edge.

A.2.6 Matrix Sheath

Sheath voltages are often driven to be significantly larger than T_e. These sheaths are significantly negative than the sheath edge potential ($\Phi = 0$). According to the Boltzmann relation, n_e tends to zero quickly, thereby leaving only ions in the sheath.

Hence, the current to the electrode is almost all ion current. This is similar to the sheath near cathodes, as well as, sheath of a Langmuir probe when it is negatively biased significantly. With the assumption of uniform ion density throughout the sheath ($n_i = n_{is}$), this is known as the Matrix sheath. According to the Poisson's equation, electric potential and ion density is related as

$$\frac{d^2\Phi(x)}{dx^2} = -\frac{en_{is}}{\epsilon_0} \tag{98}$$

Solving this equation gives

$$\Phi(x) = -\frac{1}{2}\frac{en_{is}}{\epsilon_0}x^2 \tag{99}$$

Setting $\Phi(x) = -\Phi_w$ at $x = s$ (recall sheath edge is defined as $x = 0, \Phi = 0$, hence, Φ_w is the wall potential with respect to the sheath edge), Matrix sheath thickness is obtained as

$$s = \left(\frac{2\epsilon_0\Phi_w}{en_{is}}\right)^{1/2} \tag{100}$$

In terms of Debye length, the thickness of a Matrix sheath becomes

$$s = \lambda\left(\frac{2\Phi_w}{T_e}\right)^{1/2} \tag{101}$$

Hence, a sheath thickness can be as long as tens of Debye lengths.

A.2.7 Child Langmuir Sheath

Matrix sheath is not self-consistent since it does not account for the decrease in ion density as ions move toward the chamber wall (it assumes that it's constant). Hence,

it is not considered as a best way of estimating high voltage sheaths. If the initial energy $\frac{1}{2e}mu_{is}^2$ is very small compared to the potential, the energy balance equation reduces to

$$0 = \frac{1}{2}M_i u(x)^2 + e\Phi(x) \tag{102}$$

The conservation of flux can be written as

$$J_0 = en_i(x)u(x), \tag{103}$$

where J_0 is the constant ion current in Matrix sheath. Solving for $n_i(x)$ gives

$$n_i(x) = \frac{J_0}{e}\left(- \frac{2e\Phi(x)}{M_i}\right)^{-1/2} \tag{104}$$

According to the Poisson's equation

$$\frac{d^2\Phi(x)}{dx^2} = -\frac{J_0}{\epsilon_0}\left(- \frac{2e\Phi(x)}{M_i}\right)^{-1/2} \tag{105}$$

By introducing k_D for simplification

$$\frac{d}{dx}\frac{d\Phi(x)}{dx} = k_D(-\Phi(x))^{-1/2}, \tag{106}$$

where

$$k_D = -\frac{J_0}{\epsilon_0}\left(\frac{2e}{M_i}\right)^{-1/2} \tag{107}$$

Multiplying both sides with $d\Phi(x)/dx$ gives

$$d\left(\frac{d\Phi(x)}{dx}\right)^2 = k_D(-\Phi(x))^{-1/2}d\Phi(x) \tag{108}$$

Integrating both sides results in (initial conditions: $d\Phi/dx = 0,\ \Phi = 0$)

$$\left(\frac{d\Phi(x)}{dx}\right)^2 = 2k_D(-\Phi(x))^{1/2} \tag{109}$$

Taking a square root and integrating both sides gives

$$-\Phi^{3/4}(x) = \frac{3}{2}\left(\frac{J_0}{\epsilon_0}\right)^{1/2}\left(\frac{2e}{M_i}\right)^{-1/4}x \tag{110}$$

Solving for J_0 and letting $\Phi(s) = -V_0$

$$J_0 = \frac{4}{9}\epsilon_0\left(\frac{2e}{M_i}\right)^{1/2}\frac{V_0^{3/2}}{s^2} \tag{111}$$

This is known as the space charge limited current of Child-Langmuir law. Since

$$J_0 = en_s u_B, \tag{112}$$

substituting (112) into (111) and solving for s gives

$$s = \frac{\sqrt{2}}{3}\lambda\left(\frac{2V_0}{T_e}\right)^{3/4} \tag{113}$$

The Child-Langmuir sheath therefore can be on the order of 100 Debye lengths. Due

to this region being so long with the absence of electrons to excite neutrals, Child-Langmuir sheath appears to be dark. Electric potential within the Child-Langmuir sheath can be derived by using (111) in (110)

$$\Phi(x) = -V_0\left(\frac{x}{s}\right)^{4/3} \tag{114}$$

Since $E = -\nabla\Phi$, the equation above can be re-written as

$$E = \frac{4}{3}\frac{V_0}{s}\left(\frac{x}{s}\right)^{1/3} \tag{115}$$

Then the charge density n is derived as

$$n = \frac{4}{9}\frac{\epsilon_0}{e}\frac{V_0}{s^2}\left(\frac{x}{s}\right)^{-2/3} \tag{116}$$

A.2.8 Electron Distribution Functions

A.2.8.1 Velocity Distribution Function

Electron velocity distribution function $g(x, u)$ is defined as the number of electrons in six dimensional space at time t. The six dimensions include (x, y, z) for R^3 position space, and (u_x, u_y, u_z) for V^3 velocity space. Therefore, to calculate the total number of electrons N, $g(x, u)$ has to be integrated over the entire R^3 position space and V^3 velocity space. Taking the example of an R^1 position space and V^1 velocity space, in which the size of R^1 is L, the number of electrons would be

$$N_e = \int_0^L \int_{-\infty}^{\infty} g(x, u_x) du_x dx = \int_0^L \int_{-\infty}^{\infty} g(x, u_x) dx du_x \tag{117}$$

If the velocity distribution is independent of position, that is g is no longer a function

of x, the number of electrons would be

$$N_e = \int_0^L dx \int_{-\infty}^{\infty} g(u_x) du_x = L \int_{-\infty}^{\infty} g(u_x) du_x \tag{118}$$

Accordingly, the number density n_e is defined as

$$n_e = \frac{N_e}{L} = \int_{-\infty}^{\infty} g(u_x) du_x \tag{119}$$

The velocity distribution can be independent of position when thermal equilibrium is achieved: electron-electron collisions are high, and electron and neutral temperature is equivalent ($T_e = T_n$). Under such conditions, $g(u_x)$ follows the Boltzmann distribution. In V^1 space, the Boltzmann velocity distribution is given as

$$g_B(u_x) = n_e \Big(\frac{m_e}{2\pi k T} \Big)^{1/2} e^{-\frac{m_e u_x^2}{2kT}} \text{ [s/m]} \tag{120}$$

Note that the unit is [s/m] because it is in V^1 space. From now on, it is assumed that all distribution functions are independent of position, that is the integration is conducted within a unit volume. Thus, when it is integrated over the entire velocity, the resulting value would be n_e; the number of electrons N_e per unit space. Since an isotropic velocity distribution is assumed, averaging the velocity would return a zero value. Therefore, it is meaningful to average the squared velocity. The average of the squared velocity in V^1 space $< u_x^2 >$ is given as

$$< u_x^2 > = \frac{\int_{-\infty}^{\infty} u_x^2 g_B(u_x) du_x}{\int_{-\infty}^{\infty} g_B(u_x) du_x}$$

$$= \frac{1}{n_e} \int_{-\infty}^{\infty} u_x^2 g_B(u_x) du_x \tag{121}$$

$$= \left(\frac{m_e}{2\pi kT}\right)^{1/2} \int_{-\infty}^{\infty} u_x^2 e^{-\frac{m_e u_x^2}{2kT}} du_x$$

By utilizing the following integration property

$$\int_{-\infty}^{\infty} x^2 e^{-ax^2} dx = \frac{1}{2}\sqrt{\frac{\pi}{a^3}}, \tag{122}$$

$< u_x^2 >$ is reduced to

$$< u_x^2 > = \left(\frac{m_e}{2\pi kT}\right)^{1/2} \frac{1}{2} \sqrt{\frac{\frac{\pi}{1}}{\frac{m_e^3}{8k^3T^3}}}$$

$$= \frac{kT}{m_e} \left[(\mathrm{m/s})^2\right] \tag{123}$$

This again leads to the correlation between energy and temperature of electrons

$$\frac{1}{2} m_e < u_x^2 > = \frac{1}{2} kT, \tag{124}$$

which is only true when thermal equilibrium is satisfied ($T = T_n = T_e$). In the case of low temperature and low density plasma, gas temperature T_n is significantly lower than that of electrons. In this case, the gas temperature cannot represent the electron energy. Generalizing (124) into V^3 space also assumes isotropic velocity distribution.

$$\frac{1}{2}m_e < u^2 >= \frac{3}{2}kT \tag{125}$$

It is important to remember the following.

$$u^2 = u_x^2 + u_y^2 + u_z^2 \tag{126}$$

$$u^2 \neq 3u_x^2 \tag{127}$$

$$< u^2 >= 3 < u_x^2 > \tag{128}$$

$$< u_x >= 0 \tag{129}$$

$$< u >= 0 \tag{130}$$

The Boltzmann velocity distribution in V^3 space is

$$g_B(u) = n_e\Big(\frac{m_e}{2\pi kT}\Big)^{3/2} e^{-\frac{m_e u^2}{2kT}} \ [(\mathrm{s/m})^3], \tag{131}$$

where $u^2 = u_x^2 + u_y^2 + u_z^2$. By definition, $g_B(u)$ indicates the number of electrons in 3D velocity space.

A.2.8.2 Speed Distribution Function

The speed distribution function is different from the velocity distribution function in the following aspects. In V^3 space, only one velocity of certain magnitude and direction exists. However, when only magnitude is considered as in the case of speed distribution, there are $4\pi v^2$ number of velocities of magnitude v. Therefore, the Boltzmann speed distribution is given as

$$f_B(v) = 4\pi v^2 n_e \Big(\frac{m_e}{2\pi kT}\Big)^{3/2} e^{-\frac{m_e v^2}{2kT}} \text{ [s/m]} \tag{132}$$

Note that the unit is [s/m] since speed v is a scalar (1-dimension). The Boltzmann speed distribution has the following characteristic values.

$$v_{mp} = \sqrt{\frac{2kT}{m_e}}, \quad v_{av} =< v >= \sqrt{\frac{8kT}{\pi m_e}}, \quad v_{rms} = \sqrt{\frac{3kT}{m_e}} \tag{133}$$

v_{mp} is the most probable speed; defined as v at which $df(v)/dv = 0$ is satisfied. v_{av} is the average speed. v_{rms} is the root mean square speed. The average kinetic energy of electrons can be derived by initially obtaining $< u^2 >$ using the integration property

$$\int_0^\infty x^{2n} e^{-ax^2} dx = \frac{(2n)!}{n! 2^{2n+1}} \sqrt{\frac{\pi}{a^{2n+1}}} \tag{134}$$

The average of the squared speed is derived as

$$< v^2 > = \frac{\int_0^\infty v^2 f_B(v) dv}{\int_0^\infty f_B(v) dv}$$

$$= \frac{\int_0^\infty v^2 f_B(v) dv}{n_e}$$

$$= 4\pi \Big(\frac{m_e}{2\pi kT} \Big)^{3/2} \int_0^\infty v^4 e^{-\frac{m_e v^2}{2kT}} dv \tag{135}$$

$$= 4\pi \Big(\frac{m_e}{2\pi kT} \Big)^{3/2} \frac{4!}{2!2^5} \sqrt{\frac{\pi}{(m_e/2kT)^5}}$$

$$= \frac{3}{2} \frac{2kT}{m_e}$$

Therefore,

$$\frac{1}{2} m < v^2 >= \frac{3}{2} kT \tag{136}$$

A.2.8.3 Energy Distribution Function

Electron energy distribution function (EEDF) is defined as the number of electrons in the energy space. The energy and temperature of electrons are related to the speed v.

$$\epsilon = \frac{1}{2} m v^2 \tag{137}$$

Hence, the number of electrons in a unit volume is obtained by integrating an EEDF over the entire energy.

$$n_e = \int_0^\infty f(\epsilon) d\epsilon = \int_0^\infty f(v) dv \tag{138}$$

Since,

$$f(\epsilon)d\epsilon = f(v)dv$$

$$f(\epsilon) = f(v)\frac{dv}{d\epsilon} \tag{139}$$

$$= \frac{2n}{\sqrt{\pi}}\frac{\sqrt{\epsilon}}{(kT)^{3/2}}e^{-\frac{\epsilon}{kT}}$$

The average energy $< \epsilon >$ is derived as

$$< \epsilon >= \frac{\int_0^\infty \epsilon f(\epsilon)d\epsilon}{\int_0^\infty f(\epsilon)d\epsilon} = \frac{3}{2}kT, \tag{140}$$

which leads to the following

$$< \epsilon >= \frac{1}{2}m < v^2 >= \frac{3}{2}kT \tag{141}$$

A.2.9 Electron Flux

Flux is defined as the number of particles passing through a unit area per unit time. Electron flux in z-axis direction is given as

$$\Gamma_{ez} = n_e < u_z > \tag{142}$$

For $u_z > 0$,

$$
\begin{aligned}
< u_z > &= \frac{\int_{-\infty}^{\infty} u_z g_B(u)\ du}{\int_{-\infty}^{\infty} g_B(u)\ du} \\
&= \frac{1}{n_e}\int_{-\infty}^{\infty} u_z g_B(u)\ du
\end{aligned}
\tag{143}
$$

In spherical coordinate, $u_z = ucos\theta$, $du = du_x du_y du_z = u^2 sin\theta\ dud\phi d\theta$

$$
\begin{aligned}
< u_z > &= \frac{1}{n_e}\int_0^{\infty}\int_0^{2\pi}\int_0^{\pi/2} ucos\theta g_B(u)\ u^2 sin\theta\ dud\phi d\theta \\
&= \frac{1}{n_e}\int_0^{\infty}\int_0^{2\pi}\int_0^{\pi/2} ucos\theta n_e\Big(\frac{m_e}{2\pi kT}\Big)^{3/2} e^{-\frac{m_e u^2}{2kT}} u^2 sin\theta\ dud\phi d\theta \\
&= \Big(\frac{m_e}{2\pi kT}\Big)^{3/2}\int_0^{\infty} ue^{-\frac{m_e u^2}{2kT}} u^2\ du \int_0^{2\pi}\ d\phi \int_0^{\pi/2} sin\theta cos\theta\ d\theta \\
&= 2\pi\frac{1}{2}\Big(\frac{m_e}{2\pi kT}\Big)^{3/2}\int_0^{\infty} u^3 e^{-\frac{m_e u^2}{2kT}}\ du
\end{aligned}
\tag{144}
$$

By using the integration property

$$
\int_0^{\infty} x^{2n+1} e^{-ax^2} dx = \frac{n!}{2a^{n+1}}, \tag{145}
$$

the average velocity in z-axis direction becomes

$$
\begin{aligned}
< u_z > &= 2\pi\frac{1}{2}\Big(\frac{m_e}{2\pi kT}\Big)^{3/2}\frac{1}{2(\frac{m_e}{2kT})^2} \\
&= \pi\Big(\frac{m_e}{2\pi kT}\Big)^{3/2}\frac{4k^2T^2}{2m_e^2} \\
&= \pi\Big(\frac{m_e}{2\pi kT}\Big)^{3/2}\frac{4k^2T^2}{2m_e^2} \\
&= \sqrt{\frac{kT}{2\pi m_e}} \\
&= \frac{1}{4} < v > \quad \left(< v >= \sqrt{\frac{8kT}{\pi m_e}} \right)
\end{aligned}
\tag{146}
$$

Hence,

$$\Gamma_{ez} = \frac{1}{4} n_e < v > \tag{147}$$

A.2.10 Electron Energy Flux

The average energy flux in the z-axis direction is

$$\begin{aligned} S_{ez} &= n_e \frac{m_e}{2} < u^2 u_z > \\ &= n_e \frac{m_e}{2} \frac{1}{n_e} \int_{-\infty}^{\infty} u^2 u_z g_B(u)\ du \\ &= n_e \frac{m_e}{2} \frac{1}{n_e} \int_{-\infty}^{\infty} u^2 u_z n_e \Big(\frac{m_e}{2\pi kT}\Big)^{3/2} e^{-\frac{m_e u^2}{2kT}}\ du \\ &= n_e \frac{m_e}{2} \frac{1}{n_e} n_e \Big(\frac{m_e}{2\pi kT}\Big)^{3/2} \int_{-\infty}^{\infty} u^2 u_z e^{-\frac{m_e u^2}{2kT}}\ du \end{aligned} \tag{148}$$

Transforming the equation above into spherical coordinates gives

$$\begin{aligned} S_{ez} &= n_e \frac{m_e}{2} \Big(\frac{m_e}{2\pi kT}\Big)^{3/2} \int_0^{\infty} \int_0^{2\pi} \int_0^{\pi/2} u cos\theta u^2 e^{-\frac{m_e u^2}{2kT}} u^2 sin\theta\ du d\phi d\theta \\ &= n_e \frac{m_e}{2} \Big(\frac{m_e}{2\pi kT}\Big)^{3/2} \pi \int_0^{\infty} u^5 e^{-\frac{m_e u^2}{2kT}}\ du \\ &= n_e \frac{m_e}{2} \Big(\frac{m_e}{2\pi kT}\Big)^{3/2} \pi \frac{2!}{2(\frac{m_e}{2kT})^3} \\ &= n_e \sqrt{\frac{2k^3 T^3}{\pi m_e}} \end{aligned} \tag{149}$$

Since the electron flux in the z-axis direction is given as

$$\Gamma_{ez} = n_e \sqrt{\frac{kT}{2\pi m}}, \tag{150}$$

the electron energy flux in the z-axis direction is

$$S_{ez} = 2kT\Gamma_e \tag{151}$$

A.2.11 Planar Probe with Collisionless Sheath

Biasing the probe to a high positive potential collects only electrons and could significantly perturb the plasma. Hence, it is assumed that the probe voltage is from sufficiently negative potential to the plasma potential. Consider the probe voltage being sufficiently negative to collect only ions. According to the Child-Langmuir law, the current through the probe is

$$I = -I_i = -en_{is}u_B A, \ (n_{is} = n_s), \tag{152}$$

where the Bohm velocity u_B is

$$u_B = \left(\frac{eT_e}{M_i}\right)^{1/2} \tag{153}$$

This indicates that if T_e is known, n_s can be derived from measuring I_i. Since the plasma potential is

$$\Phi_s = \frac{T_e}{2}, \tag{154}$$

according to the Boltzmann relation, the electron density at the sheath edge will be

$$n_{es} = n_b e^{\frac{-\Phi_s}{T_e}} = 0.61 n_b \tag{155}$$

where n_b is the electron density at the boundary of the bulk plasma and the presheath (previously it was assumed that $n_s = n_{es} = n_{is}$ in the bulk plasma and presheath). In the range where the probe potential is decreasing from the plasma potential, electron current would be given as

$$I + I_i = I_e = eA\frac{1}{4} < v > n_b e^{\frac{V_p - \Phi_s}{T_e}} \tag{156}$$

By increasing the probe voltage V_p to reach Φ_s, the saturated electron current is obtained by

$$I_{esat} = eA\frac{1}{4} < v > n_b \tag{157}$$

Hence,

$$I_e = I_{esat} e^{\frac{V_p - \Phi_s}{T_e}} \tag{158}$$

Taking a natural logarithm on both sides gives

$$\ln\left(\frac{I_e}{I_{esat}}\right) = \frac{V_p - \Phi_s}{T_e} \tag{159}$$

which can be transformed into

$$\ln(I_e) = \frac{1}{T_e} V_p + \ln(I_{esat}) - \frac{\Phi_s}{T_e} \tag{160}$$

Note that the inverse slope of $\ln(I_e)$ with respect to V_p is T_e.

A.2.12 Non-Maxwellian Electrons

In low temperature and low density plasmas such as plasmas seen in DC glow discharges, thermal equilibrium is not satisfied. In this condition, the electron distribution is not Maxwellian. For an arbitrary distribution function $f(u)$, the electron

current to a planar probe assuming that the probe voltage is lower than that of the plasma potential is

$$\begin{aligned} I_e = eAn_e < u_z > &= eA \int_{-\infty}^{\infty} u_z f(u)\ du \\ &= eA \int_{-\infty}^{\infty} \int_{-\infty}^{\infty} \int_{u_{min}}^{\infty} u_z f(u)\ du_x du_y du_z, \end{aligned} \tag{161}$$

where the minimum velocity required for an electron to reach the probe tip is (Note that this was not necessary for calculating the electron flux)

$$u_{min} = \left[\frac{2e(\Phi_s - V_p)}{m_i} \right]^{1/2} \tag{162}$$

Performing a coordinate transformation into spherical coordinates gives

$$I_e = eAn_e < u_z >= eA \int_{u_{min}}^{\infty} \int_0^{2\pi} \int_0^{\theta_{min}} ucos\theta f(u) u^2 sin\theta\ dud\phi d\theta, \tag{163}$$

where $\theta_{min} = cos^{-1}(u_{min}/u)$. By integrating the equation above, the electron current is derived as the following.

$$I_e = \left(\frac{1}{2} - \frac{1}{2} \Big(\frac{u_{min}}{u} \Big)^2 \right) 2\pi eA \int_{u_{min}}^{\infty} u^3 f(u)\ du \tag{164}$$

To obtain the second derivative of I_e with respect to $V = \Phi_s - V_p$, the change of variable $\varepsilon = \frac{1}{2e} m_i u^2$ is performed as

$$I_e = \frac{2\pi e^3}{m_i^2} A \int_V^{\infty} \varepsilon \Big(1 - \frac{V}{\varepsilon} \Big) f(u(\varepsilon)) d\varepsilon \tag{165}$$

Differentiating I_e with the use of the Leibniz rule yields the following.

$$\frac{dI_e}{dV} = -\frac{2\pi e^3}{m_i^2} A \int_V^\infty f(u(\varepsilon)) d\varepsilon \tag{166}$$

Differentiating I_e again (Leibniz rule) results in the following.

$$\frac{d^2 I_e}{dV^2} = \frac{2\pi e^3}{m_i^2} A f(u(V)) \tag{167}$$

By using

$$f(\epsilon) d\epsilon = 4\pi u^2 f(u) du, \tag{168}$$

$$\varepsilon = \frac{1}{2e} m_i u^2, \tag{169}$$

the EEDF becomes the following.

$$f(\epsilon) = 2\pi \Big(\frac{2e}{m_i}\Big)^{3/2} \sqrt{\varepsilon} f(u(\varepsilon)) \tag{170}$$

Substituting (167) in (170) (note $\varepsilon = V$) results in

$$f(V) = \frac{2m_i}{e^2 A} \Big(\frac{2eV}{m_i}\Big)^{1/2} \frac{d^2 I_e}{dV^2}, \tag{171}$$

which directly gives information of $f(V)$ with the measured values of $d^2 I_e / dV^2$.

APPENDIX B

DC PLASMA EXPERIMENT

B.1 System Configuration

The automation of the plasma experiment was realized with the use of a computer installed with LabView and a micro controller (Arduino Uno). A LabView program was designed to command the micro controller to generate the pulse width modulation (PWM) signals. The PWM signals were averaged into a 0–10 V DC, which was used to control the DC power supply that was connected to the Langmuir probe. The LabView program was also used for controlling the voltage and current measurements of the probe. The measured probe voltage and current data were stored in an Excel file, which was later used in the derivation of EEPF and EEDF. Two mass flow controllers (MFC's) were individually controlled by the firmware of the MFC's, which were accessible by an ethernet connection. The two MFC's were not only used

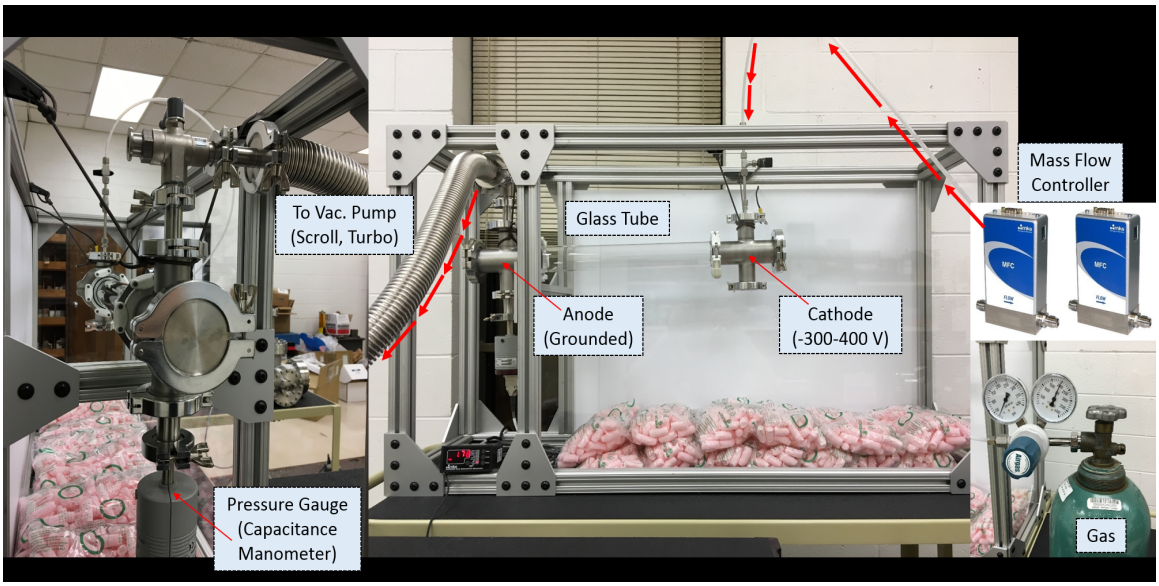

Figure 85: The experimental setup for the DC plasma measurements at Georgia Tech, NEETRAC (National Electric Energy Testing, Research, and Applications Center).

Figure 86: Materials used for constructing the Langmuir probe.

for controlling the gas mixture ratio, but also for controlling the chamber pressure. Initially, a ball valve at the downstream was adjusted to control the chamber pressure, which turned out to be extremely difficult. Later, the MFC's were used instead of the valves to control the chamber pressure, which worked perfectly. The input of the MFC's was connected to the outlet of pressure regulators attached to the gas cylinders. One thing to note is that the inlet pressure of the MFC's should be kept as low as 1–5 psi to assure stable and constant gas flow in the plasma chamber.

B.2 Probe Design

The construction of an electrostatic probe for DC plasma measurements was carried out in the lab. For the probe body, a 1/4 inch stainless steel pipe was used for maintaining a good vacuum seal at the location where the probe was inserted. The stem of the probe was made of a ceramic tube to minimize the electric field distortion. The trick is to make sure that the stainless steel probe body is not too long such that it would not interfere the uniform electric field in the plasma. The tip of the probe

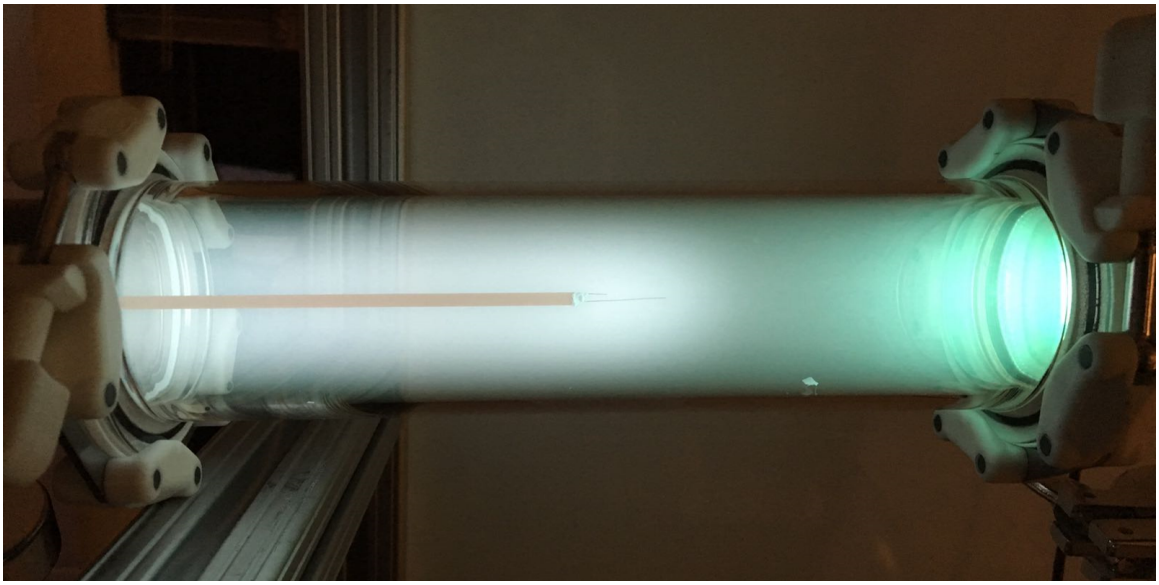

Figure 87: The lab-made Langmuir probe immersed in helium plasma.

was made of a thin tungsten wire, which went all the way through the probe stem and body. Ceramic paste, which was used to stabilize the probe tip, was fully cured before it was inserted into the plasma to avoid bubbling of the paste. The other end of the probe was tightly sealed with vacuum rated epoxy resin, which was also completely cured before use. Care was taken such that the tungsten wire does not touch the stainless steel body of the probe, which is electrically grounded.

APPENDIX C

BREAKDOWN MEASUREMENTS

Breakdown measurements on cryogenic gases were conducted in a pressure vessel installed with Bruce profiled electrodes. The gap distance between the two electrodes was fixed at 1 or 2 mm and the vessel was filled with the gas mixture at required pressure. The vessel was placed in a cryostat, which was filled with liquid nitrogen. A high voltage source was connected to the cryogenic rated bushing on the top of the vessel. The entire setup was contained in a Faraday cage during the breakdown experiment.

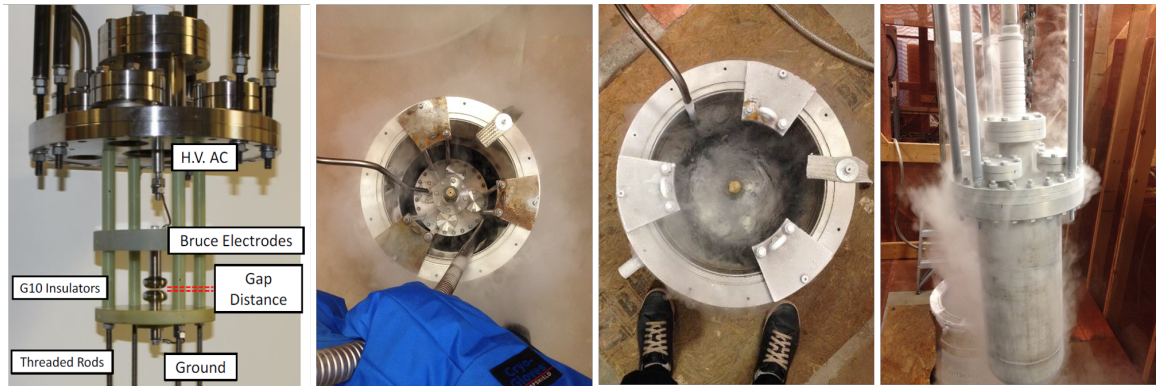

Figure 88: The experimental setup and procedure of the breakdown measurements for cryogenic gas mixtures at the Center for Advanced Power Systems, Florida State University.

REFERENCES

[1] "Plasma data exchange project," *http://fr.lxcat.net/*, 2010.

[2] *SIGLO database, http://www.lxcat.net, retrieved on November 4,*, 2015.

[3] "The boltzmann equation, two-term approximation interface," *https://www.comsol.com/blogs/the-boltzmann-equation-two-term-approximation-interface/*, 2015.

[4] "The electron boltzmann equation solver," *http://www.bolsig.laplace.univ-tlse.fr*, 2015.

[5] *Phelps database, http://www.lxcat.net, retrieved on March 11,*, 2017.

[6] *Morgan database, http://www.lxcat.net, retrieved on March 11,*, 2017.

[7] "Annual energy outlook 2017 with projections to 2050," *U.S. Energy Information Administration*, pp. 69–88, Jan 2017.

[8] Alves, L. L., Bartschat, K., Biagi, S. F., Bordage, M. C., Pitchford, L. C., Ferreira, C. M., Hagelaar, G. J. M., Morgan, W. L., Pancheshnyi, S., Phelps, A. V., Puech, V., and Zatsarinny, O., "Comparisons of sets of electronneutral scattering cross sections and swarm parameters in noble gases: II. helium and neon," *Journal of Physics D: Applied Physics*, vol. 46, no. 33, p. 334002, 2013.

[9] Auday, G., Guillot, P., Galy, J., and Brunet, H., "Experimental study of the effective secondary emission coefficient for rare gases and copper electrodes," *Journal of applied physics*, vol. 83, pp. 5917–5921, 1998.

[10] Bagnall FT, H. S., "Pre-breakdown ionization in molecular nitrogen in e x b fields," *Australian Journal of Physics*, vol. 18, no. 3, pp. 227–236, 1965.

[11] Bednorz, J. G. and Müller, K. A., "Possible hightc superconductivity in the balacuo system," *Zeitschrift für Physik B Condensed Matter*, vol. 64, pp. 189–193, Jun 1986.

[12] Berg, F., Palmer, J., Miller, P., Husband, M., and Dodds, G., "HTS electrical system for a distributed propulsion aircraft," *IEEE Transactions on Applied Superconductivity*, vol. 25, pp. 1–5, June 2015.

[13] Bray, J., "High-temperature superconducting motors and generators for power grid applications," *Cambridge, UK: Woodhead Publishing Ltd*, vol. 21, pp. 325–341, June 2015.

[14] Chachereau, A. and Pancheshnyi, S., "Calculation of the effective ionization rate in air by considering electron detachment from negative ions," *IEEE Transactions on Plasma Science*, vol. 42, pp. 3328–3338, Oct 2014.

[15] Chanin, L. M., Phelps, A. V., and Biondi, M. A., "Measurements of the attachment of low-energy electrons to oxygen molecules," *Phys. Rev.*, vol. 128, pp. 219–230, Oct 1962.

[16] Chanin, L. M. and Rork, G. D., "Measurements of the first townsend ionization coefficient in neon and hydrogen," *Phys. Rev.*, vol. 132, pp. 2547–2553, Dec 1963.

[17] Chanin, L. M. and Rork, G. D., "Experimental determinations of the first townsend ionization coefficient in helium," *Phys. Rev.*, vol. 133, pp. 1005–A1009, Feb 1964.

[18] Cheetham, P., Kim, W., Kim, C. H., Graber, L., Rodrigo, H., and Pamidi, S., "Enhancement of dielectric strength of cryogenic gaseous helium by addition of small mol% hydrogen," *IEEE Transactions on Applied Superconductivity*, vol. 27, pp. 1–5, June 2017.

[19] Cheetham, P., Park, C., Kim, C. H., Graber, L., and Pamidi, S. V., "Dielectric properties of cryogenic gas mixtures for superconducting power applications," *IOP Conference Series: Materials Science and Engineering*, vol. 278, no. 1, p. 012040, 2017.

[20] Cheung, N., "Plasma immersion ion implantation for semiconductor processing," *Materials Chemistry and Physics*, vol. 46, no. 2, pp. 132 – 139, 1996.

[21] Chu, P. K., Qin, S., Chan, C., Cheung, N. W., and Larson, L. A., "Plasma immersion ion implantationa fledgling technique for semiconductor processing," *Materials Science and Engineering: R: Reports*, vol. 17, no. 6, pp. 207 – 280, 1996.

[22] Davies, D. K., Jones, F. L., and Morgan, C. G., "Primary ionization coefficient of helium," *Proceedings of the Physical Society*, vol. 80, no. 4, p. 898, 1962.

[23] Deng, Y., Li, B., and Xiao, D., "Analysis of the insulation characteristics of C_3F_8 gas mixtures with N_2 and CO_2 using boltzmann equation method," *IEEE Transactions on Dielectrics and Electrical Insulation*, vol. 22, pp. 3253–3259, December 2015.

[24] Deng, Y., Lu, C., and Xiao, D., "Electron swarm parameters in c-C_4F_8 and CO_2 gas mixtures from boltzmann equation analysis," *IEEE Transactions on Plasma Science*, vol. 40, pp. 2671–2677, Oct 2012.

[25] Eckels, P. and Snitchler, G., "5 MW high temperature superconductor ship propulsion motor design and test results," *Naval Engineers Journal*, vol. 117, no. 4, pp. 31–36, 2005.

[26] Fitzpatrick, B. K., Kephart, J. T., and Golda, E. M., "Characterization of gaseous helium flow cryogen in a flexible cryostat for naval applications of high temperature superconductors," *IEEE Transactions on Applied Superconductivity*, vol. 17, pp. 1752–1755, June 2007.

[27] Gamble, B., Snitchler, G., and MacDonald, T., "Full power test of a 36.5 MW HTS propulsion motor," *IEEE Transactions on Applied Superconductivity*, vol. 21, pp. 1083–1088, June 2011.

[28] Go, D. B. and Pohlman, D. A., "A mathematical model of the modified paschens curve for breakdown in microscale gaps," *Journal of Applied physics*, vol. 107, no. 10, p. 103303, 2010.

[29] Godyak, V. A., Piejak, R. B., and Alexandrovich, B. M., "Probe diagnostics of nonmaxwellian plasmas," *Journal of Applied Physics*, vol. 73, no. 8, 1993.

[30] Godyak, V. A., "Measuring EEDF in gas discharge plasmas," *Plasma-Surface Interactions and Processing of Materials*, pp. 95–134, 1990.

[31] Graber, L., "Improving the accuracy of SF_6 leakage detection for high voltage switchgear," *IEEE Transactions on Dielectrics and Electrical Insulation*, vol. 18, pp. 1835–1846, December 2011.

[32] Graber, L., Bonfigli, G., and Muller, S., "Improving SF_6 leakage detection in switchgear by reducing the influence of solar radiation on density measurement," pp. 441–444, June 2008.

[33] Graber, L., Kim, W. J., Cheetham, P., Kim, C. H., Rodrigo, H., and Pamidi, S., "Dielectric properties of cryogenic gas mixtures containing helium, neon, and hydrogen," *IOP Conference Series: Materials Science and Engineering*, vol. 102, no. 1, p. 012018, 2015.

[34] Graber, L. and Pradhan, M. K., "Monitoring the SF_6 pressure level in metal-enclosed switchgear to detect gas leakages," pp. 357–362, April 2008.

[35] Graber, L., Saeedifard, M., Mauger, M. J., Yang, Q., Park, C., Niebur, T., Pamidi, S. V., and Steinhoff, S., "Cryogenic power electronics at megawatt-scale using a new type of press-pack igbt," *IOP Conference Series: Materials Science and Engineering*, vol. 279, no. 1, p. 012011, 2017.

[36] Guillot, P., Belenguer, P., Therese, L., Lavoine, V., and Chollet, H., "Secondary electron emission coefficients of standard samples for gdoes," *Surface and interface analysis*, vol. 35, no. 7, pp. 590–592, 2003.

[37] Hagelaar, G. J. M., "Coulomb collisions in the boltzmann equation for electrons in low-temperature gas discharge plasmas," *Plasma Sources Science and Technology*, vol. 25, no. 1, p. 015015, 2016.

[38] Hagelaar, G. J. M. and Pitchford, L. C., "Solving the boltzmann equation to obtain electron transport coefficients and rate coefficients for fluid models," *Plasma Sources Science and Technology*, vol. 14, no. 4, p. 722, 2005.

[39] Hayashi, M. and Nimura, T., "Calculation of electron swarm parameters in fluorine," *Journal of Applied Physics*, vol. 54, no. 9, pp. 4879–4882, 1983.

[40] Haydon, S. C. and Williams, O. M., "Combined spatial and temporal studies of ionization growth in nitrogen," *Journal of Physics D: Applied Physics*, vol. 9, no. 3, p. 523, 1976.

[41] HEYLEN, A. E. D., "Townsend's first ionization coefficient in pure nitrogen," *Nature*, vol. 183, pp. 1545–1546, 1959.

[42] Honjo, S., Mimura, T., Kitoh, Y., Noguchi, Y., Masuda, T., Yumura, H., Watanabe, M., Ikeuchi, M., Yaguchi, H., and Hara, T., "Status of superconducting cable demonstration project in japan," *IEEE Transactions on Applied Superconductivity*, vol. 21, pp. 967–971, June 2011.

[43] Husain, E. and Nema, R., "Analysis of paschen curves for air, N_2 and SF_6 using the townsend breakdown equation," *Electrical Insulation, IEEE Transactions on*, no. 4, pp. 350–353, 1982.

[44] Jaeger, E. F., Berry, L. A., Tolliver, J. S., and Batchelor, D. B., "Power deposition in highdensity inductively coupled plasma tools for semiconductor processing," *Physics of Plasmas*, vol. 2, no. 6, pp. 2597–2604, 1995.

[45] Jiang, X., Li, X., Zhao, H., Jia, S., Yan, J. D., and Zhu, K., "Analysis of the dielectric breakdown characteristics for a 252 kV gas circuit breaker," *IEEE Transactions on Power Delivery*, vol. 28, pp. 1592–1599, July 2013.

[46] Jones, J., "Ionization coefficients in nitrogen," *Journal of Physics D: Applied Physics*, vol. 1, no. 6, p. 769, 1968.

[47] Kephart, J. T., Fitzpatrick, B. K., Ferrara, P., Pyryt, M., Pienkos, J., and Golda, E. M., "High temperature superconducting degaussing from feasibility study to fleet adoption," *IEEE Transactions on Applied Superconductivity*, vol. 21, pp. 2229–2232, June 2011.

[48] Kim, J. Y., Cho, W.-H., Dang, J.-J., Chung, K.-J., and Hwang, Y., "Characterization of electron kinetics regime with electron energy probability functions in inductively coupled hydrogen plasmas," *Physics of Plasmas*, vol. 23, no. 2, p. 023511, 2016.

[49] Kim, J. Y., Kim, D.-H., Kim, J. H., Jeon, S.-B., Cho, S.-W., and Chung, C.-W., "Power dependence of electron density at various pressures in inductively coupled plasmas," *Physics of Plasmas*, vol. 21, no. 11, p. 113505, 2014.

[50] Kim, J. Y., Kim, Y.-C., Kim, Y.-S., and Chung, C.-W., "Effect of the electron energy distribution on total energy loss with argon in inductively coupled plasmas," *Physics of Plasmas*, vol. 22, no. 1, p. 013501, 2015.

[51] Lawton, S. A. and Phelps, A. V., "Excitation of the b1$\sum$+g state of O_2 by low energy electrons," *The Journal of Chemical Physics*, vol. 69, no. 3, pp. 1055–1068, 1978.

[52] Li, X., Zhao, H., and Jia, S., "Dielectric breakdown properties of SF_6-N_2 mixtures in the temperature range 300-3000 K," *Journal of Physics D: Applied Physics*, vol. 45, no. 44, p. 445202, 2012.

[53] Li, X., Zhao, H., Jia, S., and Murphy, A. B., "Study of the dielectric breakdown properties of hot SF_6-CF_4 mixtures at 0.01-1.6 MPa," *Journal of Applied Physics*, vol. 114, no. 5, 2013.

[54] Li, X., Zhao, H., Jia, S., and Murphy, A. B., "Prediction of the dielectric strength for c-C_4F_8 mixtures with CF_4, CO_2, N_2, O_2 and air by boltzmann equation analysis," *Journal of Physics D: Applied Physics*, vol. 47, no. 42, p. 425204, 2014.

[55] Li, X., Zhao, H., Wu, J., and Jia, S., "Analysis of the insulation characteristics of CF_3I mixtures with CF_4, CO_2, N_2, O_2 and air," *Journal of Physics D: Applied Physics*, vol. 46, no. 34, p. 345203, 2013.

[56] Lieberman, M. A. and Lichtenberg, A. J., "Chapter14," *Principles of plasma discharges and materials processing 2nd ed.*, Wiley, 2005.

[57] Lisovskiy, V., Yakovin, S., and Yegorenkov, V., "Low-pressure gas breakdown in uniform DC electric field," *Journal of Physics D: Applied Physics*, vol. 33, no. 21, p. 2722, 2000.

[58] Lozansky, E. D. and Firsov, O. B., "Theory of sparks," *Moscow: Atomizdat*, 1975.

[59] Miller, J., Santosusso, D., Uva, M., Woods, K., and Fitzpatrick, B., "Naval superconducting integrated power system (sips)," *10th Intelligent Ship Symposium*, May 2013.

[60] Nagorny, V. and Drallos, P., "Effective secondary emission coefficient in a high-pressure noble gas," *Plasma Sources Science and Technology*, vol. 6, no. 2, p. 212, 1997.

[61] Nowlin, R. N. and Carlile, R. N., "The electrostatic nature of contaminative particles in a semiconductor processing plasma," *Journal of Vacuum Science & Technology A: Vacuum, Surfaces, and Films*, vol. 9, no. 5, pp. 2825–2833, 1991.

[62] Oh, S.-J., Lee, H.-C., and Chung, C.-W., "A study on plasma parameters in Ar/SF_6 inductively coupled plasma," *Physics of Plasmas*, vol. 24, no. 1, p. 013512, 2017.

[63] ONNES, H. K., "The superconductivity of mercury," *Comm. Phys. Lab. Univ. Leiden*, vol. 122, p. 124, 1911.

[64] Palmer, A. J., "A physical model on the initiation of atmospheric-pressure glow discharges," *Applied Physics Letters*, vol. 25, no. 3, pp. 138–140, 1974.

[65] Pamidi, S., Kim, C. H., and Graber, L., "High-temperature superconducting (HTS) power cables cooled by helium gas in superconductors in the power grid: Materials and applications," *Cambridge, UK: Woodhead Publishing Ltd*, vol. 21, pp. 225–260, June 2015.

[66] Pamidi, S. V., "Research and development efforts at center for advanced power systems in the area of superconducting power devices," *CAPS*, 2015.

[67] Pamidi, S., Kim, C. H., Kim, J.-H., Crook, D., and Dale, S., "Cryogenic helium gas circulation system for advanced characterization of superconducting cables and other devices," *Cryogenics*, vol. 52, no. 46, pp. 315 – 320, 2012. 2011 Space Cryogenics Workshop.

[68] Park, C., Graber, L., Cheetham, P., Viquez, J. G., Kim, C. H., and Pamidi, S., "A versatile modeling technique for predicting dielectric strength improvements in gas mixtures for superconducting applications," *IEEE Transactions on Dielectrics and Electrical Insulation*, vol. 24, pp. 2755–2764, Oct 2017.

[69] Park, C., Graber, L., Kim, W., Cheetham, P., Kim, C., Pamidi, S., and Rodrigo, H., "A versatile model for estimating breakdown voltage and its application for cryogenic gas mixtures," *2016 IEEE Conference on Electrical Insulation and Dielectric Phenomena (CEIDP)*, pp. 542–545, Oct 2016.

[70] Park, C., Pamidi, S., and Graber, L., "Boltzmann analysis of cryogenic He-H_2 gas mixtures as dielectric media for high-temperature superconducting power devices," *IEEE Transactions on Applied Superconductivity*, vol. 27, pp. 1–6, June 2017.

[71] Park, C., Graber, L., and Pamidi, S., "The dielectric properties of gaseous cryogen mixtures of He, H_2, Ne, and N_2 in a temperature range of 50-80 K at pressures up to 2.0MPa," *Journal of Applied Physics*, vol. 121, no. 8, p. 083304, 2017.

[72] Park, C., Pamidi, S., and Graber, L., "The critical electric field of gas mixtures over the extended range of cryogenic operating conditions," *Journal of Applied Physics*, vol. 122, no. 15, p. 153301, 2017.

[73] Park, C., Pamidi, S. V., and Graber, L., "Langmuir probe plasma diagnostics to investigate the dielectric properties of cryogenic gas mixtures," *IOP Conference Series: Materials Science and Engineering*, vol. 278, no. 1, p. 012039, 2017.

[74] Pejovic, M. M., Ristic, G. S., and Karamarkovic, J. P., "Electrical breakdown in low pressure gases," *Journal of Physics D: Applied Physics*, vol. 35, no. 10, p. R91, 2002.

[75] Petrović, Z. L., Dujko, S., Marić, D., Malović, G., Nikitović, Ž., Šašić, O., Jovanović, J., Stojanović, V., and Radmilović-Rajenović, M., "Measurement and interpretation of swarm parameters and their application in plasma modelling," *Journal of Physics D: Applied Physics*, vol. 42, no. 19, p. 194002, 2009.

[76] Phelps, A. and Petrovic, Z. L., "Cold-cathode discharges and breakdown in argon: surface and gas phase production of secondary electrons," *Plasma Sources Science and Technology*, vol. 8, no. 3, p. R21, 1999.

[77] Pinheiro, M. J. and Loureiro, J., "Effective ionization coefficients and electron drift velocities in gas mixtures of SF_6 with He, Xe, CO_2 and N_2 from boltzmann analysis," *Journal of Physics D: Applied Physics*, vol. 35, no. 23, p. 3077, 2002.

[78] Raizer, Y. P., "Chapter4," *Gas Discharge Physics*, Springer, 2011.

[79] Rey, C. and Malozemoff, A., "Fundamentals of superconductivity," *Cambridge, UK: Woodhead Publishing Ltd*, vol. 21, pp. 29–74, June 2015.

[80] Rodrigo, H., Kwag, D., Graber, L., Trociewitz, B., and Pamidi, S., "AC flashover voltages along epoxy surfaces in gaseous helium compared to liquid nitrogen and transformer oil," *IEEE Transactions on Applied Superconductivity*, vol. 24, pp. 1–6, June 2014.

[81] Rong, M., Sun, H., Yang, F., Wu, Y., Chen, Z., Wang, X., and Wu, M., "Influence of O_2 on the dielectric properties of CO_2 at the elevated temperatures," *Physics of Plasmas*, vol. 21, no. 11, 2014.

[82] Sili, E., Cambronne, J.-P., and Koliatene, F., "Temperature dependence of electrical breakdown mechanism on the left of the paschen minimum," *Plasma Science, IEEE Transactions on*, vol. 39, no. 11, pp. 3173–3179, 2011.

[83] Snitchler, G., Gamble, B., King, C., and Winn, P., "10 MW class superconductor wind turbine generators," *IEEE Transactions on Applied Superconductivity*, vol. 21, pp. 1089–1092, June 2011.

[84] Spence, D. and Schulz, G. J., "Temperature dependence of dissociative attachment in O_2 and CO_2," *Phys. Rev.*, vol. 188, pp. 280–287, Dec 1969.

[85] Tanaka, Y., "Prediction of dielectric properties of N_2/O_2 mixtures in the temperature range of 300-3500K," *Journal of Physics D: Applied Physics*, vol. 37, no. 6, p. 851, 2004.

[86] Terpstra, M. A., "Flammability limits of hydrogen-diluent mixtures in air," *Department of mechanical and manufacturing engineering, Calgary, Alberta*, 2012.

[87] Tezcan, S. S., Dincer, M. S., Bektas, S., and Hiziroglu, H. R., "Boltzmann analysis of electron swarm parameters in binary CF_4+Ar mixtures," *IEEE Transactions on Dielectrics and Electrical Insulation*, vol. 20, pp. 98–103, February 2013.

[88] Towler, G. and Sinnott, R., "Chemical engineering design, 2nd edition: Principles, practice and economics of plant and process design," *Butterworth-Heinemann*, pp. Physical Property Data Bank: C1–C3, January 2012.

[89] Uhm, H. S., Whang, K. W., Choi, E. H., and Kim, S. S., "Influence of penning effects on high-pressure discharge in the plasma display panel," *Physics of Plasmas (1994-present)*, vol. 9, no. 2, pp. 706–712, 2002.

[90] von Engel, A., "Handbuch der physik," Springer Berlin, 1956.

[91] Wang, W., Murphy, A. B., Rong, M., Looe, H. M., and Spencer, J. W., "Investigation on critical breakdown electric field of hot sulfur hexafluoride/carbon tetrafluoride mixtures for high voltage circuit breaker applications," *Journal of Applied Physics*, vol. 114, no. 10, 2013.

[92] Wang, W., Tu, X., Mei, D., and Rong, M., "Dielectric breakdown properties of hot SF_6/He mixtures predicted from basic data," *Physics of Plasmas*, vol. 20, no. 11, 2013.

[93] White, R. D., Robson, R. E., Schmidt, B., and Morrison, M. A., "Is the classical two-term approximation of electron kinetic theory satisfactory for swarms and plasmas?," *Journal of Physics D: Applied Physics*, vol. 36, no. 24, p. 3125, 2003.

[94] Yao, S., Huang, R., Zhang, X., Zhong, L., Wang, X., Wu, Y., and Rong, M., "Influence of copper contamination on dielectric breakdown properties of high-temperature SF_6 gas based on boltzmann equation analysis," *Electric Power Equipment-Switching Technology (ICEPE-ST), 2015 3rd International Conference on*, pp. 317–320, Oct 2015.

[95] Yoon, J.-S., Song, M.-Y., Han, J.-M., Hwang, S. H., Chang, W.-S., Lee, B., and Itikawa, Y., "Cross sections for electron collisions with hydrogen

molecules," *Journal of Physical and Chemical Reference Data*, vol. 37, no. 2, 2008.

[96] Yousfi, M., de Urquijo, J., Juarez, A., Basurto, E., and Hernandez-Avila, J. L., "Electron swarm coefficients in CO_2-N_2 and CO_2-O_2 mixtures," *IEEE Transactions on Plasma Science*, vol. 37, pp. 764–772, June 2009.

[97] Zhao, H., Li, X., Jia, S., and Murphy, A. B., "Dielectric breakdown properties of SF_6-N_2 mixtures at 0.01-1.6 MPa and 300-3000 K," *Journal of Applied Physics*, vol. 113, no. 14, 2013.

[98] Zhao, H., Li, X., Jia, S., and Murphy, A. B., "Prediction of the critical reduced electric field strength for carbon dioxide and its mixtures with 50% O_2 and 50% H_2 from boltzmann analysis for gas temperatures up to 3500 K at atmospheric pressure," *Journal of Physics D: Applied Physics*, vol. 47, no. 32, p. 325203, 2014.

[99] Zhao, H. and Lin, H., "Dielectric breakdown properties of N_2-O_2 mixtures by considering electron detachments from negative ions," *Physics of Plasmas*, vol. 23, no. 7, p. 073505, 2016.